

BIO-INSPIRED TENDON-DRIVEN SYSTEMS: COMPUTATIONAL
ANALYSIS, OPTIMIZATION, AND HARDWARE IMPLEMENTATION

by

Joshua M. Inouye

A Dissertation Presented to the
FACULTY OF THE USC GRADUATE SCHOOL
UNIVERSITY OF SOUTHERN CALIFORNIA
In Partial Fulfillment of the
Requirements for the Degree
DOCTOR OF PHILOSOPHY
(BIOMEDICAL ENGINEERING)

May 2012

Epigraph

But grow in the grace and knowledge of our Lord and Savior Jesus Christ. To him be the glory both now and to the day of eternity. Amen.

2 Peter 3:18

Dedication

To my father, my mother, and my Heavenly Father.

Acknowledgements

There have been many people that have provided invaluable contributions to my research and personal encouragement in difficult times. My father and mother originally instilled in me a very strong work ethic from a very young age, and this set the foundation for all of the perseverance that was necessary to get to this point. They always were very encouraging throughout my life and I owe them much love and thanks. My brother and sister have likewise been very encouraging in my journey the past several years.

I would like to thank Laila Guessous and Brian Sangeorzan for accepting me into the summer NSF Research Experience for Undergraduates at Oakland University during my undergraduate studies. I first became interested in academic research after my great experience there, and I am indebted to them for their generosity in their time and effort mentoring me.

I would like to thank Francisco Valero-Cuevas so much for his incredible guidance in the past few years and for believing in me and funding me even when I had a very slow start in finding a lab during my first few years at USC. If I had not connected with him, I would have dropped out of the PhD program. I have learned so much from him about doing solid research, obtaining funding, networking, managing a versatile and interdisciplinary lab, and appreciating many different cultures.

I would also like to thank Jason Kutch for all of his guidance and help. He provided some very crucial advice at many important turning points in my research, and his encouragement and experience were huge factors that led to quick progress once I settled on a research project.

Manish Kurse was also extremely helpful to me nearly every day. We worked on some similar research areas, being that we are both mechanical engineers, and he was able to teach me many things about linear algebra, efficient programming, and experimental testing.

Thanks also to Alex Reyes, who has become one of my best friends in the past few years, for always listening to my ideas and giving helpful feedback and encouragement. In addition, he has taught me a lot about circuit design and electrical engineering, which hopefully will come in handy someday.

To the other lab members to which I am extremely indebted for their advice, opinions, and encouragement: Sudarshan Dayanidhi, Evangelos Theodorou, Cornelius Raths, Brendan Holt, Emily Lawrence, and Srideep Musuvathy.

I would also like to thank Edward Ebramzadeh for his advice, encouragement, and friendship as well. I worked in his lab for about a year and learned a great deal about orthopaedic research as well as perseverance in my doctoral studies.

Thanks to Jill McNitt-Gray, Chris Powers, and Phil Requejo for allowing me to do laboratory rotations in their labs, and the students Joe Munaretto and Sean Farrokhi, for helping me work on their projects, and Noom Somboon also for helping me with research projects.

I would like to thank the members of my guidance committee for their time and efforts in providing suggestions to ensure a respectable thesis submission: Terry Sanger, Tansu Celikel, Stefan Schaal, and Gaurav Sukhatme. Additional thanks to Tansu and Stefan for taking positions on my dissertation committee.

Thanks to Mischal Diasanta for all of her help and guidance in class selection as well as encouragement and advice in the lab selection process. She has been an absolutely fantastic graduate advisor.

Lastly and most importantly, all of my work would not have been possible without the hand of the Lord in my life.

Table of Contents

Epigraph	ii
Dedication	iii
Acknowledgements	iv
List Of Tables	xi
List Of Figures	xii
Abstract	xviii
Chapter 1: Introduction	1
1.1 Background	1
1.2 Previous Work	2
1.3 Significance of Research	4
1.4 Dissertation outline	5
Chapter 2: Fundamentals of Tendon Actuation	7
2.1 General serial linkage mechanisms	7
2.1.1 Kinematics	9
2.1.2 Kinetics	15
2.2 Tendon routing and moment arms	22
2.3 Definition of necessary actuation: versatility	24
2.3.1 Moment arm matrices	25
2.3.2 Necessary conditions for admissible moment arm matrices	27
2.4 Discussion	31
Chapter 3: Fundamentals of Feasible Sets	33
3.1 Forward analysis I: from feasible activation sets to feasible force sets using vertex enumeration.	33
3.2 Forward analysis II: from basis vectors to feasible sets using Minkowski sums.	39
3.3 Why SVD is not the correct approach for analysis of tendon-driven systems	39
3.4 Other cases	43
3.4.1 Feasible wrench sets	44

3.4.2	Feasible velocity and twist sets	47
3.4.3	Feasible acceleration sets	49
Chapter 4: A Novel Synthesis of Computational Approaches Enables Optimization of Task-Independent Grasp Quality of Tendon-Driven Hands	51	
4.1	Abstract	51
4.2	Introduction	51
4.3	Procedure	56
4.3.1	Finding the set of feasible grasp wrenches and computing grasp quality	56
4.3.1.1	Select initial grasp parameters	56
4.3.1.2	Build fingertip feasible force set	56
4.3.1.3	Find feasible object force set	57
4.3.1.4	Simplify feasible object force set	58
4.3.1.5	Translate contact forces to object wrenches	60
4.3.1.6	Find feasible grasp wrench set	61
4.3.1.7	Compute grasp quality	62
4.3.2	Computing grasp quality metrics for specific manipulator designs .	63
4.3.2.1	Finger topology	63
4.3.2.2	Grasp configuration	65
4.3.2.3	Calculating grasp quality	66
4.3.2.4	Monte Carlo simulations	67
4.3.2.5	Regression analysis	67
4.4	Results	68
4.4.1	Baseline results	68
4.4.2	Monte Carlo simulations	69
4.4.3	Regression analysis	70
4.5	Discussion	73
4.6	Appendix: Calculation of the feasible force sets of tendon-driven manipulators	77
Chapter 5: Quantitative Prediction of Grasp Impairment in Peripheral Neuropathies of the Hand	81	
5.1	Abstract	81
5.2	Introduction	81
5.3	Methods	81
5.4	Results and Discussion	84
Chapter 6: Bettering the Human Hand: Anthropomorphic Tendon-Driven Robotic Hands can Exceed Human Grasping Capabilities	86	
6.1	Abstract	86
6.2	Introduction	87
6.3	Procedure	89
6.3.1	Calculating human hand grasp quality	89
6.3.2	Calculating anthropomorphic hand grasp quality	90
6.3.3	Optimizing anthropomorphic hand grasp quality	94

6.3.3.1	Monte Carlo on structure matrices	94
6.3.3.2	Optimization of joint centers of rotation	95
6.3.3.3	Optimization of maximal tendon tensions	97
6.4	Results	99
6.4.1	Random Monte Carlo designs	99
6.4.2	Optimization of joint centers of rotation and distribution of maximal tendon tensions	102
6.5	Discussion	105

Chapter 7: Asymmetric Routings With Fewer Tendons Can Offer Both Flexible Endpoint Stiffness Control and High Force-Production Capabilities in Robotic Fingers 109

7.1	Abstract	109
7.2	Introduction	110
7.3	Methods	113
7.3.1	Analysis and Synthesis of Stiffness	116
7.3.1.1	Joint Stiffness Adjustability	116
7.3.1.2	Endpoint Stiffness Eccentricity	119
7.3.2	Analysis and Optimization of Force Polytopes	121
7.4	Results	124
7.4.1	Joint Stiffness Adjustability	124
7.4.2	Optimized Endpoint Stiffness Eccentricity vs. Maximal Isotropic Value	125
7.4.3	Optimizing MIV for 3 Specific Routings	126
7.5	Discussion	128

Chapter 8: A Novel Computational Approach Helps Explain and Reconcile Conflicting Experimental Findings on the Neural Control of Arm Endpoint Stiffness 132

8.1	Abstract	132
8.2	Introduction	133
8.3	Methods	136
8.3.1	Arm Model	136
8.3.2	Theoretical Formulation	136
8.3.3	Checking for Realizable Endpoint Stiffness Matrices	141
8.3.4	Varying Moment Arms and Synergies	144
8.3.5	Exploring Energy Expenditure Within the Stiffness Redundancy Solution Space	145
8.4	Results	146
8.4.1	Realizable Fraction of Endpoint Stiffness Ellipses	146
8.4.2	Realizable Orientations in the Presence of Synergies	148
8.4.3	Energy Expenditure Ranges	149
8.5	Discussion	151

Chapter 9: Optimization of Tendon Topology for Robotic Fingers: Prediction and Implementation	154
9.1 Abstract	154
9.2 Introduction	155
9.3 Finger Construction	158
9.4 Methods	159
9.4.1 Force polytope analysis	159
9.4.2 Evaluating tendon routings	164
9.4.3 Experimental testing of tendon routings	167
9.5 Results	170
9.5.1 Calculating maximum isotropic values	170
9.5.2 Theoretical predictions vs. experimental results	171
9.6 Discussion	175
9.7 Conclusions	181
Chapter 10: Computational Optimization and Experimental Evaluation of Grasp Quality for Tendon-Driven Hands Under Constraints	183
10.1 Abstract	183
10.2 Introduction	184
10.3 Methods	186
10.3.1 Hand Construction	186
10.3.2 Grasp Quality Analysis	188
10.3.3 Optimization of Grasp Quality	191
10.3.3.1 Optimizing Pulley Sizes	192
10.3.3.2 Optimizing Tendon Tension Distribution	192
10.3.4 Experimental testing of tendon routings	195
10.4 Results	197
10.4.1 Computational grasp quality predictions	197
10.4.2 Theoretical predictions vs. experimental results	199
10.5 Discussion	200
Chapter 11: Conclusions and Future Work	206
Bibliography	208

List Of Tables

4.1	Baseline grasp quality results. Coefficient of static friction $\mu_s = 0.5$. Units of grasp quality are in Newtons.	69
4.2	Average evaluation times (standard deviations) during Monte Carlo simulations, in seconds.	70
4.3	Significant normalized regression coefficients for grasp quality with 95% confidence intervals on N+1 topology, 2-finger grasp. ‘-’ denotes not significant at the cutoff p-value of 0.05. Moment arms expressed as (Joint number,tendon number). $R^2 = 0.930$	72
4.4	Expected (from linear regression on Monte Carlo iterations) and actual (from computational method implementation) effects of moment arm adjustments by 10% on grasp quality of N+1 design, 2-finger grasp. Moment arms expressed as (Joint number,tendon number).	73
5.1	Muscles in each nerve pathology group. M: median, R: radial, U: ulnar, CTS: Carpal Tunnel Syndrome.	83
6.1	Maximal joint diameters (i.e., differences between largest moment arms for each joint) according to data obtained from the literature.	93

List Of Figures

2.1	(a) Human arm modeled as planar 2-joint serial manipulator. (b) Human thumb modeled as 3-D 5-joint serial manipulator.	9
2.2	Coordinate frames assigned to planar 2-link arm with the D-H convention and corresponding D-H parameters.	11
2.3	Homogeneous transformation matrix in terms of i^{th} set of D-H parameters.	13
2.4	Coordinates of hand obtained from homogeneous transformation matrix.	13
2.5	Illustration of Jacobian for arm system.	16
2.6	Calculation of joint torques using perpendicular distances of line of action from joint axes. Force units are in N.	19
2.7	A one-DOF manipulator configurations and associated endpoint force production capabilities. (a) Torque motor. (b) Tendons with equal max tensions, equal moment arms. (c) Tendons with unequal max tensions, equal moment arms. (d) Tendons with equal max tensions, unequal moment arms.	24
2.8	Fundamental relationship between tendon routing and moment arm matrices. Tendon layout of 2 4-DOF robotic fingers and their associated moment arm matrices. (a) All equal moment arms. (b) Varying moment arms. Not to scale. Note that this figure underscores how a given tendon routing drawing has a corresponding moment arm matrix, and vice versa.	26
2.9	(a) A one-DOF manipulator. (b) Determination of null space of R with singular value decomposition. (c) Calculation of solution for tendon tensions, given desired joint torque.	31
3.1	Forward mapping of feasible activation set to feasible force set. Note: the feasible activation set and the feasible tendon tension set for this example are both in \mathbb{R}^6 , but only 3 dimensions are shown.	34

3.2	3-D Feasible force set of 5-DOF finger using parameters shown.	38
3.3	Demonstration of the duality between basis vectors and feasible sets.	40
3.4	Illustration of why manipulating force ellipsoids do not accurately capture the force-production capabilities of tendon-driven manipulators.	43
3.5	Differing endpoint conditions affect feasible wrench set analysis for 3-DOF planar manipulator. (a) Fixed boundary condition, 3 DOFs constrained. (b) Pin joint boundary condition, 2 DOFs constrained.	45
3.6	One-DOF manipulator.	49
4.1	Illustration of integration of techniques that were previously isolated.	54
4.2	Flowchart of steps for finding feasible grasp wrench set and computing grasp quality.	55
4.3	An example of a fingertip feasible force set and its intersection with a friction cone to produce a feasible object force set.	57
4.4	(a) An example of an edge collapse operation. The vertices \mathbf{v}_1 and \mathbf{v}_2 are collapsed into a new vertex \mathbf{v}_{new} . (b) Example of using edge collapse operations to simplify the feasible object force set from 19 vertices down to 10 vertices. Note: this view is of the underside of the feasible object force set shown in Figure 4.3.	59
4.5	Grasp configurations analyzed. (a) 4-DOF robotic finger, 2N tendon arrangement, with endpoint wrench description. (b) 4-DOF robotic finger, N+1 tendon arrangement.	64
4.6	Grasp configurations analyzed. (a) Isometric view of 2-finger grasp. (b) Front view of 2-finger grasp. (c) Side view of 3-finger grasp.	66
4.7	Uniform sampling distribution used for each independent parameter value perturbation in Monte Carlo simulations.	68
4.8	Histogram of grasp quality values from Monte Carlo simulations for two-finger grasp, 2N and N+1 designs, with Gaussian curves overlaid. The N+1 topologies exceeding the baseline 2N topology are shaded gray.	70
5.1	Grasp quality calculation steps. (a) Basis vectors. (b) Feasible force sets. (c) Feasible object force sets. (d) Feasible object wrench illustrated in 3-D. (e) Grasp quality metric of radius of largest ball (illustrated in 3-D; actual calculation is in 6-D).	82

5.2	Grasp quality deterioration as a function of % advancement of neuropathy.	85
6.1	Computation of human hand grasp quality. Index finger and thumb basis vectors and feasible force sets not equal scales. (a) Fingertip basis vectors. (b) Feasible force sets built from basis vectors. (c) Feasible object force sets: intersection of feasible force sets with friction cones. (d) Feasible object wrench (only 3-D feasible forces shown). (e) Examples of maintained and failed grasps.	91
6.2	Anthropomorphic hand grasp.	92
6.3	Procedure for finding randomized designs via Monte Carlo sampling.	96
6.4	Crossover of the 10 structure matrices with the highest MIVs for each finger.	96
6.5	Illustration of perturbations of the joint center of rotation.	97
6.6	Illustration of Markov-Chain Monte Carlo algorithm for distribution of maximal tendon tensions.	98
6.7	Comparison of human grasp quality with boxplots of anthropomorphic hand designs. Optimization step #1 is for the joint centers of rotation. Optimization step #2 is for the distribution of maximal tendon tensions..	100
6.8	Various index finger tendon routings. Not to scale. (a) Best crossover index finger design selected for optimization. (b) Example of an index finger tendon routing that produced a very low grasp quality. (c) Typical 2N design.	101
6.9	Markov-Chain Monte Carlo optimization. (a) Visualization of optimization paths of 10 random seeds and one center seed. (b) Optimization progress over 150 iterations.	102
6.10	Index finger tendon layout, maximal tendon tension distribution, and feasible force sets for top 2 optimized designs and the human hand. Tendon layouts shown roughly to scale. Feasible force sets shown to scale.	103
6.11	Power grasp of a heavy bar. The hand must resist a force that is opposite the distal direction of the index finger.	106
7.1	Procedure for finding admissible structure matrices. N+1 structure matrix shown.	115
7.2	Postures analyzed for each tendon routing. Link lengths and joint diameters shown to scale (i.e., with kinematic parameters of the DLR hand). . .	115

7.3 Reformulation of variables in Equation 7.4 for use in Equation 7.6. (\bullet) denotes element-by-element multiplication. R_i is the i^{th} row of R . Joint stiffness adjustability (JSA) is equal to $\text{rank}(\tilde{R})$.	119
7.4 Joint stiffness adjustability versus number of tendons, plotted for all admissible routings. Mathematically, JSA is the rank of \tilde{R} , which is the number of free parameters of the joint stiffness matrix that can be independently chosen.	124
7.5 Optimized endpoint stiffness eccentricity (ESE*) vs. unoptimized maximal isotropic value (MIV), averaged over the 3 postures. Note: only 524 out of 1,200 data points shown (all other designs had higher ESE* than 8 and lower MIV than 16). Large circles mark the averages of posture 1 (small squares), posture 2 (small triangles), and posture 3 (small diamonds) for the routings shown in Figure 7.6.	125
7.6 Illustration of 3 routings along with stiffness ellipsoids and feasible force sets. JSA: Joint stiffness adjustability. MIV: Maximal isotropic value before optimization, in N. MIV*: Maximal isotropic value after optimization, in N. ESE: Endpoint stiffness eccentricity before optimization. ESE*: Endpoint stiffness eccentricity after optimization. \vec{K}_t^* : tendon stiffnesses producing ESE*, normalized so that maximal stiffness is 1. \vec{T}_{max}^* : maximal tendon tensions producing MIV*, in N. Note: all results shown are for posture 2 only, and values correspond with the small triangles in Figure 7.5.127	127
8.1 (a) Arm model. (b) Workspace of arm model. SVD used to transform endpoint stiffness matrix to a stiffness ellipse.	137
8.2 Endpoint stiffness variables reformulated. (\bullet) denotes element-by-element multiplication, and R_i is the i^{th} row of R .	140
8.3 The endpoint stiffness ellipse as defined by the desired endpoint stiffness vector, corresponding to an orientation angle and a set condition number.	142
8.4 Example of realizable orientations in various postures for a condition number of 2. Red lines indicate that the orientation of the major axis in that position is realizable, and black lines indicate that the orientation is not realizable.	143
8.5 Fraction of realizable orientations given various modeled conditions.	147
8.6 Range of orientations in the presence of synergies.	148
8.7 Maximal possible energy reduction for any orientation given the condition number and posture.	150

9.1	2-D and 3-D views of finger model in SolidWorks, and the actual finger.	160
9.2	Pulleys used in finger design. (a) Turcite rotating small pulley. (b) Aluminum terminating small pulley. (c) Turcite rotating large pulley. (d) Aluminum terminating large pulley.	161
9.3	Illustration of calculation of MIV (maximum isotropic value) from feasible force set.	162
9.4	Base moment arm matrices used when finding admissible and unique tendon routings.	166
9.5	Finger posture used in computations and experimental testing.	166
9.6	Experimental system for feasible force set testing.	169
9.7	Maximum isotropic values for various routings. (a) Boxplot of MIV for all designs before and after pulley-size optimization. (b) Boxplot of MIV vs. design (includes optimized and unoptimized pulley sizes).	172
9.8	Results from experimental testing of various routings. (a) The 6 different routings tested. Shown to scale. R matrix values are in mm. (b) Experimental vs. theoretical MIV. Parity line is where experimental MIV would be exactly equal to theoretical MIV (intercept of 0, slope of 1). Regression has an R^2 value of 0.987. (c) Table of averages from 3 tests for each design in main posture. (d) 3-D visualization of experimental and theoretical feasible force sets for designs 1 and 6.	173
9.9	Illustration of a simple (but intelligent) tendon re-routing that drastically increases MIV.	176
10.1	Top and side views of finger design and kinematics.	187
10.2	Finger placements for each grasp.	190
10.3	Base moment arm matrices used when finding realizable, unique tendon routings.	191
10.4	Illustration of Markov-Chain Monte Carlo algorithm for distribution of maximal tendon tensions.	194
10.5	Experimental system for grasp testing.	196
10.6	(a) Computational results of grasp quality for hand designs. Optimization paths shown. (b) Pulley-size and max tension optimized designs.	198

10.7 Computational predictions of fitness for unoptimized and optimized naive 2N design.	199
10.8 Results from experimental testing of various routings. Experimental vs. theoretical grasp quality for both grasps. Parity line is where experimental grasp quality would be exactly equal to theoretical grasp quality (intercept of 0, slope of 1). Regression line constant term forced to zero. 3-D force portions of grasp wrench set for two different tests shown on right (torque constrained to zero).	201
10.9 Experimental vs. predicted volumes of grasp wrench sets.	204

Abstract

This thesis work focuses on the design and optimization of tendon-driven systems. One of the chief reasons these systems can be termed “bio-inspired” is due to the fact that they produce forces and movements via tendons which are connected to actuators and have uni-directional action (they can only pull, not push). In particular, the human hand sets itself apart from the rest of the body’s neuromuscular systems in that there are no muscles in the fingers themselves: all the muscles are proximal to the fingers. The study and analysis of tendon-driven hands and fingers suggest that i) the human hand is mechanically optimized for grasping capabilities and ii) use of bio-inspired principles in robotic systems can drastically improve force-production capabilities, grasp strength, and stiffness control performance. Some of the bio-inspired principles which are proven throughout this work to be very beneficial in robotic systems are asymmetry and skewed combinations of design parameters. This work not only has strong implications for the design of commercial robotic and prosthetic hands, but also broadly seeks to inspire creativity in design and optimization routines for complex problems in many different engineering disciplines.

Chapter 1

Introduction

1.1 Background

Biomimetic tendon-driven systems have been designed over the past few decades for the purposes of grasping and manipulation (Ambrose, Aldridge, Askew, Burridge, Bluethmann, Diftler, Lovchik, Magruder & Rehnmark 2000, Jacobsen, Iversen, Knutti, Johnson & Biggers 1986, Jau 1995, Massa, Roccella, Carrozza & Dario 2002, Salisbury 1982).

These systems (including dexterous prosthetic and robotic hands) take their inspiration from the tendons present in the entirety of the human body. The most fantastic example of a tendon-driven system either in nature or in robotics is the human hand. The complexity, intricacy, and functionality of its elaborate architecture and 46 muscles have never been duplicated, even without consideration of its spectacular sensory and regeneration capabilities. It is unrivaled in its ability to grasp and manipulate objects, particularly in unstructured environments, while having very compact size and excellent durability when compared with robotic and prosthetic hands available today.

While bio-inspired artificial hands have been criticized for issues such as friction and tendon compliance (Chang, Lee & Yen 2005), they have distinct advantages over torque-driven hands including light weight, low backlash, small size, high speed, and remote actuation (Tsai 1995). Another important advantage is that they offer significant design flexibility in setting moment arms and maximal tendon tensions (Pons, Ceres & Pfeiffer 1999), which allows optimization of capabilities for particular families of tasks (such as grasping).

1.2 Previous Work

Several studies have addressed the problem of designing the topology, tendon routing, or link design of tendon-driven manipulators (or fingers). According to Flavio Firmani, for example, “The knowledge of maximum twist (velocity-producing) and wrench (force-producing) capabilities is an important tool for achieving the optimum design of manipulators” (Firmani, Zibil, Nokleby & Podhorodeski 2008). Special attention has been given to the design of manipulators with isotropic transmission characteristics (i.e., ability to transmit forces equally in all directions at the end effector) (Lee 1991, Chen, Su & Yao 1999, Ou & Tsai 1996, Sheu, Huang & Lee 2009). A few advantages of this isotropic property include more uniform tendon force distribution and minimization of the dispersion of noise through the system (Salisbury & Craig 1982, Ou & Tsai 1996). However, it has been noted that it may be advantageous to design a manipulator with non-isotropic characteristics (Tsai 1995), as is the case in the human hand (Valero-Cuevas 2005). In

addition, prior work on isotropic transmission does not consider tension limits of the tendons, which is of particular importance when designing small, dexterous hands.

There is a vast body of literature on defining and computing grasp quality metrics. Some studies emphasize the full set of grasp wrenches, but do not take into account the force capabilities of each finger (Miller & Allen 1999). Many other grasp quality metrics can be computed based on other criteria, but do not take into account any tendon-driven architectures, which limits their applications to the design of tendon-driven mechanisms (Surez Feijo, Cornell & Roa Garzn 2006). Previous research on grasp quality for tendon-driven hands has enabled computation of a grasp quality metric based on a very specific, pre-defined task wrench space (Fu & Pollard 2006). However, they note that their methodology, which utilizes a linear programming approach, does not generalize to the full set of feasible grasp wrenches.

Several studies have analyzed the kinetostatic performance of tendon-driven and torque-driven manipulators (Bouchard, Gosselin & Moore n.d., Chiacchio, Bouffard-Vercelli & Pierrot 1997, Firmani et al. 2008, Finotello, Grasso, Rossi & Terribile 1998, Gouttefarde & Krut 2010, Zibil, Firmani, Nokleby & Podhorodeski 2007, Tsai 1995, Lee & Tsai 1991, Lee 1991) (determining the kinetostatic capabilities given design parameters), and several others have addressed their optimization or synthesis (specifying the design parameters given desired capabilities) (Fu & Pollard 2006, Chen et al. 1999, Ou & Tsai 1993, Ou & Tsai 1996, Sheu et al. 2009, Angeles 2004, Aref, Taghirad & Barissi 2009, Chablat & Angeles 2002, Khan & Angeles 2006). These studies are based on mathematical *theory*. The *fabrication* of robotic fingers has been widely accomplished for robotic hands (Jacobsen et al. 1986, Salisbury & Craig 1982, Shadow

Robot Company n.d., Grebenstein, Albu-Schaffer, Bahls, Chalon, Eiberger, Friedl, Gruber, Hagn, Haslinger & Hppner n.d., Ambrose et al. 2000, Jau 1995, Massa et al. 2002, Lin & Huang 1996, Kawasaki, Komatsu & Uchiyama 2002, Namiki, Imai, Ishikawa & Kaneko 2003, Yamano & Maeno 2005, Gaiser, Schulz, Kargov, Klosek, Bierbaum, Pylatiuk, Oberle, Werner, Asfour & Brethauer 2008). Experimental *testing* of kinetostatic performance can be found in the biomechanics literature (Kuxhaus, Roach & Valero-Cuevas 2005, Valero-Cuevas, Zajac & Burgar 1998), but these do not implement a system whose parameters can be altered. We combine these three areas of *theory, fabrication, and testing* to optimize and validate hardware implementations of alternative robotic finger and hand designs.

1.3 Significance of Research

Borrowing principles from robotics and mathematics (Yoshikawa 2002) and utilizing computational geometry tools, this dissertation research is devoted to developing and implementing computational analyses of tendon-driven systems. This thesis presents novel analysis methods and the results from associated experimental studies.

The significance of using this methodology for analyzing human hands is that it allows the quantification of the deterioration of grasping abilities of hands that are subjected to nerve trauma (e.g., an injury to the innervation pathways of the hand due to a traffic accident) or disease (e.g., carpal tunnel syndrome, or low nerve palsies resulting from incomplete spinal cord injury). In addition, due to impairment or loss of grasping abilities resulting from disease or trauma, tendon-transfer surgeries (where a tendon from one

muscle is cut and then attached to another area to restore function) are commonly used to reinstate these abilities. Part of this work now enables comparison of various tendon-transfer surgeries to calculate their predicted success. Comparison of patient outcomes with these quantitative predictions of functional impairment and surgical success will allow more rapid development of new treatment modalities.

The significance of this research for designing robotic and prosthetic hands is that it will allow optimization of the strength and minimization of the size of these hands. More specifically, the design methodology developed in this reserach can be used to design dexterous, tendon-driven hands with higher grasp capabilities than are currently available, and simpler hands with specific capabilities.

In addition to robotic and prosthetic hand design, the application of this methodology is very broad and is applicable to the design of any industrial and commercial tendon-driven system. One example of such a commercial system is the da Vinci Surgical System, which is the most successful commercially-available surgical robotic system and whose instruments are driven by tendons. Moreover, the small size afforded by tendon-driven devices make them ideal for minimally invasive surgery, rescue robot and service robot applications.

1.4 Dissertation outline

There are 11 chapters in this thesis including the introductory chapter. Chapters 2 and 3 are dedicated to introductory material on tendon-driven systems which is the mathematical and computational foundation for the remaining chapters. These were my

parts of a book chapter submitted in 2011 with Francisco Valero-Cuevas, Jason Kutch, and Evangelos Theodorou. Chapter 4 is based on a journal paper which develops a novel method for grasp quality analysis of tendon-driven hands, and it is the core analysis methodology for chapters 5, 6, and 10. Chapter 5 is based on a conference paper on human hand grasp quality following nerve disorders. Chapter 6 is based on a journal paper which compares the human hand with optimized robotic hands that have the same kinematics and constraints. Chapter 7 is based on a full-length conference paper which compares hundreds of robotic finger designs in their force-production and passive stiffness control characteristics. Chapter 8 is based on a journal paper which analyzes the capabilities of humans to control the stiffness characteristics of their arms. Chapters 9 and 10 are based on journal papers which experimentally test bio-inspired, reconfigurable finger designs in hardware. Francisco Valero-Cuevas is the last author on the papers based on Chapters 2-10, and Jason Kutch is the second author on the papers based on Chapters 4, 5, and 9. Chapter 11 discusses conclusions and future research.

Chapter 2

Fundamentals of Tendon Actuation

A thorough understanding of the kinematics and kinetics of tendon-driven actuation is necessary to fully analyze the capabilities and limitations inherent in these biological and robotic systems. This section gives a brief overview of i) the theory behind the basic kinematic and kinetic analysis of serial robotic manipulators and ii) the aspects of tendon-driven systems that set them apart from traditional torque-driven systems. It should be noted that this section is intended to give the reader a sense of the mathematical principles of these topics and some associated issues, but is by no means comprehensive and further study is likely required to use this knowledge in practice. Our prior publications (Valero-Cuevas, Hoffmann, Kurse, Kutch & Theodorou 2009, Valero-Cuevas 2005) also contain a wealth of references to background material.

2.1 General serial linkage mechanisms

The term “serial linkage mechanism” refers to a mechanism (or manipulator as is called in robotics) that has two basic types of joints that connect different links in series to grant them DOFs: prismatic and revolute. Prismatic joints (i.e., translational) are those

that can extend or retract a link along a fixed axis with no rotation (e.g., a pneumatic or hydraulic cylinder), and revolute (i.e., rotational) joints are those that revolve a certain axis with no other motion (e.g., a hinge joint). In this section, we will be concentrating on revolute joints, as these are the types of joints that are used to represent the DOFs of vertebrate limbs. Most vertebrate limbs are approximated by revolute joints articulating rigid links¹. Universal joints such as those used to represent 2-DOF joints like in the metacarpophalangeal (MCP) joint of the index finger (which is the base knuckle of the finger) can be represented by two revolute joints with intersecting rotational axes. Other joints with 3 DOFs like the shoulder or hip can be represented by spherical joints with three revolute joints with rotational axes perpendicular to each other. Other joints like the knee are more complex and involve both rotation and sliding.

The primary goals of robotic (and biological) manipulators are to i) produce a certain desired kinematics at the end-effector (e.g., the hand is the end-effector if the arm is considered as the manipulator, or the fingertip is the end-effector if the finger is considered as the manipulator) or ii) to produce a desired force at the end-effector. Combinations of motion and force are also desired, but they are an important special case that is treated in detail elsewhere (Keenan, Santos, Venkadesan & Valero-Cuevas 2009).

¹In biological systems, joint kinematics arise from the interaction of the contact of bony articulating surfaces held by ligamentous structures. In such cases, the kinematics can be load dependent (Valero-Cuevas & Small 1997)

2.1.1 Kinematics

Kinematics refers to the motions and positions of a manipulator without regard to the forces that produce them. Very straightforward methods can be used to calculate velocities and positions of the end-effector. The basic kinematic problem can be stated as follows: given that we have a mechanical model and known the joint variables (i.e., joint angles and angular velocities) of a robotic or biological manipulator, what is the endpoint position and velocity? We will first describe the method for calculating endpoint position.

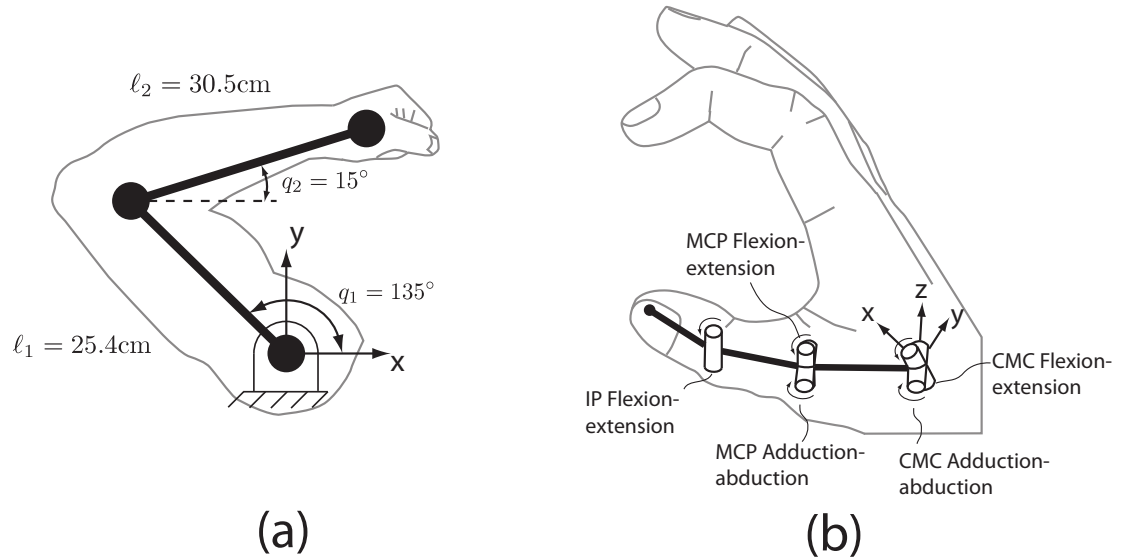


Figure 2.1: (a) Human arm modeled as planar 2-joint serial manipulator. (b) Human thumb modeled as 3-D 5-joint serial manipulator.

A human arm modeled as a planar 2-joint serial manipulator is shown in Figure 2.1a. The variables used to calculate the hand position are the lengths of the forearm and upper arm and the joint angles of the shoulder and elbow joint. It requires very little knowledge of geometry to be able to calculate that the endpoint (in cm) is at

$$(x, y) = (25.4 \cos(135^\circ) + 30.5 \cos(15^\circ), 25.4 \sin(135^\circ) + 30.5 \sin(15^\circ)) = (11.5, 25.9)$$

Simple enough. However, consider the 3-D model of the thumb shown in Figure 2.1b, in which there is one universal joint at the CMC (carpometacarpal) joint, one universal joint at the MCP (metacarpophalangeal), and one hinge joint at the IP (interphalangeal) joint. Say the metacarpal bone (closest to the wrist) has length 5.08cm, the proximal phalanx (next bone toward the thumbtip) has length 3.18cm, and the distal phalanx (the bone on the thumbtip) has length 2.54cm, and the joint angles are (as defined by the Denavit-Hartenberg convention, explained below):

Joint	Angle
CMC Adduction-abduction	-45°
CMC Flexion-extension	20°
MCP Adduction-abduction	-10°
MCP Flexion-extension	-30°
IP Flexion-extension	-20°

Where is the endpoint? The analytical expression for calculating the endpoint coordinates is quite complicated, and the position is very difficult to calculate by cursory geometric examination. However, we are able to calculate the endpoint position in relation to a global reference frame in a straightforward, step-by-step manner if we use *homogeneous transformations* of coordinate systems, and attach a unique coordinate system to each link of the serial manipulator. The placement of the coordinate system is most conveniently and concisely done for serial manipulators using the Denavit-Hartenberg (D-H) convention (Denavit 1955), and is shown for the arm example in Figure 2.2.

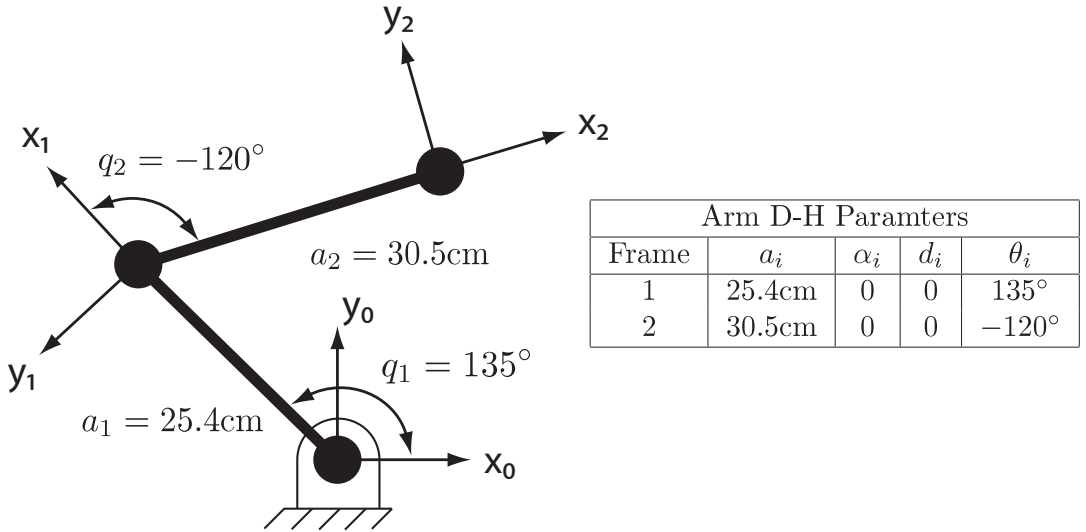


Figure 2.2: Coordinate frames assigned to planar 2-link arm with the D-H convention and corresponding D-H parameters.

Each coordinate system (after the global coordinate system x_0, y_0, z_0) is placed in a systematic manner to obey the convention and accurately define each of the 4 parameters. The i^{th} z-axis of each joint is always aligned with the i^{th} joint axis. In the arm example, the axes of rotation are all out of the page in the positive z-axis. The x-axis is defined as the directed line perpendicular to the z-axes from frame $i - 1$ to frame i . For the arm example, this means that the i^{th} x-axis is aligned with the i^{th} link. The y-axis is then determined from the already-defined x- and z-axes using the right-hand rule.

Briefly, the Denavit-Hartenberg convention involves 4 parameters for each coordinate system transformation defined by a joint-link combination: a , α , d , and θ . For serial manipulators with all revolute joints, these parameters are easily defined. The link length for the i^{th} link is a_i , the rotation of the z-axis from frame $i - 1$ to i around the i^{th} x-axis is α_i (typically in 90° increments for serial robotic manipulators), the perpendicular distance

between the x-axes of link $i - 1$ and i is d_i (typically 0 for serial robotic manipulators), and the joint angle for the i^{th} joint is θ_i . The parameters for the arm example are shown in Figure 2.2 and the parameters for the thumb example are (note that the 5th frame, not shown in Figure 2.1b, is at the thumbtip):

Thumb D-H Parameters				
Frame	a_i	α_i	d_i	θ_i
1	0	-90°	0	-45°
2	2"	0	0	20°
3	0	-90°	0	-10°
4	1.25"	0	0	-30°
5	1"	0	0	-20°

Once the D-H parameters are determined, the procedure for finding the endpoint is standardized (in fact, it was developed to be implemented computationally for arbitrary systems) by means of homogeneous transformations expressed in terms of D-H parameters. A homogeneous transformation matrix is a 4×4 matrix composed of a 3×3 rotation matrix, a 3×1 translation vector, and a 1×4 row vector whose elements are always $\begin{bmatrix} 0 & 0 & 0 & 1 \end{bmatrix}$, as shown in Figure 2.3. The i^{th} parameter set can be used to transform points from frame i back to frame $i - 1$. For our purposes, we can use one homogeneous transformation matrix for each set of D-H parameters, multiply them together, and then read off the 3×1 translation vector which has the x, y, and z coordinates of the endpoint.

Let us take the arm as a short example. The transformation matrix T_1^2 uses the D-H parameters from frame 2 and the transformation matrix T_0^1 uses the D-H parameters from

$$T_{i-1}^i = \begin{bmatrix} \cos(\theta_i) & -\sin(\theta_i) \cos(\alpha_i) & \sin(\theta_i) \sin(\alpha_i) & a_i \cos(\theta_i) \\ \sin(\theta_i) & \cos(\theta_i) \cos(\alpha_i) & -\cos(\theta_i) \sin(\alpha_i) & a_i \sin(\theta_i) \\ 0 & \sin(\alpha_i) & \cos(\alpha_i) & d_i \\ 0 & 0 & 0 & 1 \end{bmatrix}$$

3x3 Rotation Matrix 3x1 Translation Vector
 ↓ ↓
 ↓

1x4 Constant Vector

Figure 2.3: Homogeneous transformation matrix in terms of i^{th} set of D-H parameters.

frame 1 to produce the following transformation T_0^2 matrix, from which we can directly get the coordinates of the endpoint, shown in Figure 2.4.

$$T_0^2 = T_1^2 T_0^1 = \begin{bmatrix} 0.966 & -0.259 & 0 & 11.5 \\ 0.259 & 0.966 & 0 & 25.9 \\ 0 & 0 & 1 & 0 \\ 0 & 0 & 0 & 1 \end{bmatrix}$$

(x,y,z) position of hand
 ↓

Figure 2.4: Coordinates of hand obtained from homogeneous transformation matrix.

Using this simple method, we can determine that the coordinates (in cm) of the thumb endpoint are (8.92, -3.94, -2.49). While this is not an exhaustive treatment of the kinematics of serial manipulators, homogeneous transformations, or the D-H parameter convention, it suffices for the purposes of this chapter to know that the endpoint coordinates of any manipulator can be obtained in analytical form, into which the D-H parameters can be substituted to get the endpoint position. For a more detailed explanation of these topics, the reader is referred to (Valero-Cuevas 2005, Denavit 1955, Murray,

Li & Sastry 1994, Yoshikawa 1990). In addition, an interesting analysis of anatomical D-H parameters found in the human thumb can be reviewed in (Santos & Valero-Cuevas 2006).

Let us now turn to the issue of calculating endpoint velocity, given joint angular velocities of the joints. The endpoint velocity vector can be calculated using the following equation:

$$\dot{\vec{x}} = J(\vec{q})\dot{\vec{q}} \quad (2.1)$$

where $\dot{\vec{x}}$ is the endpoint velocity vector (generally $\begin{bmatrix} \dot{x} & \dot{y} & \dot{z} \end{bmatrix}^T$, but can be modified to $\begin{bmatrix} \dot{x} & \dot{y} \end{bmatrix}^T$ if manipulator is planar), $J(\vec{q})$ is the manipulator Jacobian, \vec{q} is the vector of joint angles, and $\dot{\vec{q}}$ is the vector of joint angular velocities.

The manipulator Jacobian is fundamental to the calculation of the feasible motions and forces that a manipulator can generate. It is a matrix of partial derivatives of the endpoint position coordinates with respect to each of the joint angles, as shown in the following equation ($x(\vec{q})$ denotes the analytical expression of x-position of the endpoint as a function of \vec{q} , as determined by the homogeneous transformations described above or other methods):

$$J(\vec{q}) = \begin{bmatrix} \frac{\partial x(\vec{q})}{\partial q_1} & \frac{\partial x(\vec{q})}{\partial q_2} & \dots & \frac{\partial x(\vec{q})}{\partial q_n} \\ \frac{\partial y(\vec{q})}{\partial q_1} & \frac{\partial y(\vec{q})}{\partial q_2} & \dots & \frac{\partial y(\vec{q})}{\partial q_n} \\ \frac{\partial z(\vec{q})}{\partial q_1} & \frac{\partial z(\vec{q})}{\partial q_2} & \dots & \frac{\partial z(\vec{q})}{\partial q_n} \end{bmatrix} \quad (2.2)$$

where n is the number of joints of the manipulator. The last row can be eliminated if analyzing a planar manipulator, since all the entries will be zero anyways. In addition,

it should be noted that this is a *translational* Jacobian (i.e., involving only the endpoint position). Jacobians with up to 6 rows which describe the endpoint translational and angular velocity can be similarly calculated (Yoshikawa 2002), but we will work primarily with translational velocities and forces in this chapter, in which case we only require the calculation of the translational Jacobian.

Each column of the Jacobian is the endpoint velocity vector produced by one unit of the corresponding joint angular velocity (i.e., the first column of the Jacobian is the endpoint velocity vector produced by an angular velocity of 1 radian per second at the first joint if other joint angular velocities are zero, the second column is the velocity vector produced by a 1 radian per second angular velocity at the second joint if other joint velocities are zero, etc.). Let us look at the planar arm example again. If we eliminate the last row since the arm is planar, then the Jacobian is illustrated in Figure 2.5.

It can be noted that the translational Jacobian for the thumb example has 3 rows (for x, y, and z coordinates) and 5 columns (one for each joint, or rotational DOF). Further treatment of the Jacobian can be found in (Yoshikawa 2002, Murray et al. 1994). For now, it suffices for the reader to know that the Jacobian relates joint velocities to endpoint velocities, and that it can be derived in a straightforward manner for any arbitrary serial manipulator by taking partial derivatives of the analytical expressions derived from the use of D-H parameterization (or other methods) and homogeneous transformations.

2.1.2 Kinetics

Kinetics refers to the forces and/or energy transmitted through a system without regard to its motion or positioning capabilities. We will mainly address the force-production

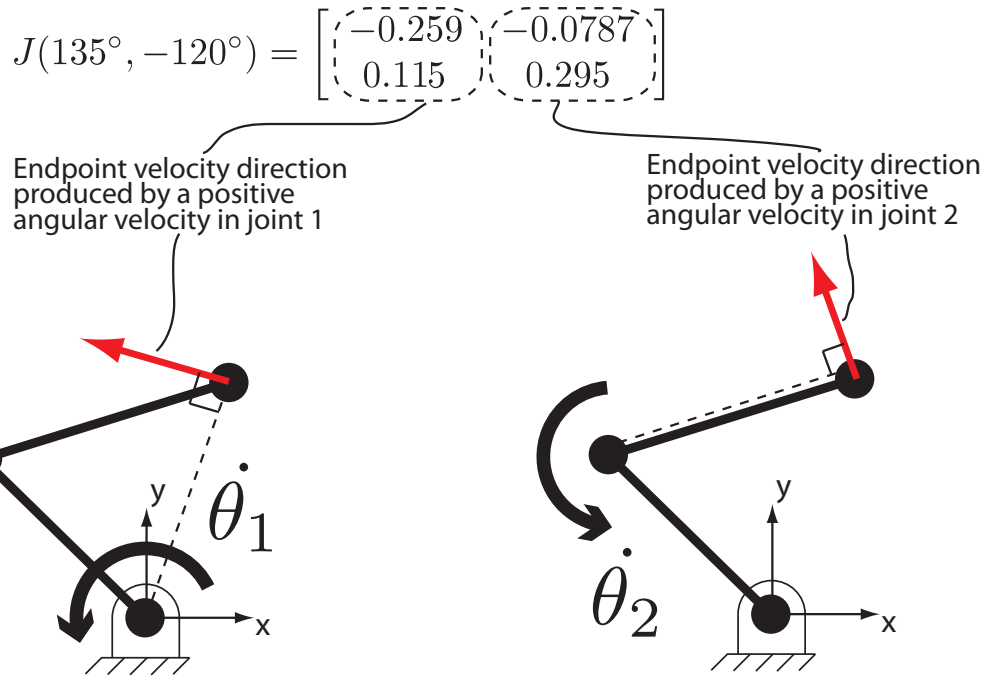


Figure 2.5: Illustration of Jacobian for arm system.

capabilities of manipulators. The main equation involved in determining the forces that can be produced by a serial manipulator is given in the following static equilibrium equation:

$$\vec{\tau} = J(\vec{q})^T \vec{F} \quad (2.3)$$

where $\vec{\tau}$ is the vector of joint torques, $J(\vec{q})^T$ is the transpose of the Jacobian at a specific posture (i.e., set of joint angles, \vec{q}), and \vec{F} is the 3-D vector of forces (or 2-D if analyzing a planar system) produced at the endpoint. This equation is derived using the principle of virtual work. For simplicity we will write J instead of $J(\vec{q})$. We begin with the following basic physics equations:

$$W = \vec{F} \cdot \vec{x} \quad (2.4)$$

$$W = \vec{\tau} \cdot \vec{q} \quad (2.5)$$

$$(2.6)$$

Which, for conservation of energy means that the internal (joint torques) and external (endpoint forces) must equal each other in the absence of deformation of the rigid links:

$$\vec{F} \cdot \vec{x} = \vec{\tau} \cdot \vec{q} \quad (2.7)$$

where W is the work done, \vec{F} is a vector of forces, \vec{x} is a vector of translational displacements, $\vec{\tau}$ is a vector of joint torques, and \vec{q} is a vector of angular displacements.

Taking differentials on both sides, we get

$$\partial W = \vec{F} \cdot \partial \vec{x} \quad (2.8)$$

$$\partial W = \vec{\tau} \cdot \partial \vec{q} \quad (2.9)$$

$$\vec{F} \cdot \partial \vec{x} = \vec{\tau} \cdot \partial \vec{q} \quad (2.10)$$

Substituting the dot product operator by its equivalent vector inner product, we get

$$\vec{F}^T \partial \vec{x} = \vec{\tau}^T \partial \vec{q} \quad (2.11)$$

If we then divide both sides by ∂t then we get

$$\vec{F}^T \dot{\vec{x}} = \vec{\tau}^T \dot{\vec{q}} \quad (2.12)$$

Now, since we have already seen in Equation 2.1 that $\dot{\vec{x}} = J \dot{\vec{q}}$, then we can produce

$$\vec{F}^T J \dot{\vec{q}} = \vec{\tau}^T \dot{\vec{q}} \quad (2.13)$$

$$\vec{F}^T J = \vec{\tau}^T \quad (2.14)$$

And following the rules of transposition for matrix multiplication we get

$$\vec{\tau} = J^T \vec{F} \quad (2.15)$$

Recall that although it is not explicitly shown for simplicity, J is really $J(\vec{q})$, a function of \vec{q} (i.e., joint configuration).

Let us look at the arm example. If we would like to exert a 1N force in the positive y-direction (or rather, that we want to resist a 1N force in the negative y-direction), we can uniquely specify the joint torques which will make this happen. It is simple to do this by using the basic equation $\tau = Fd$, where F is the force applied and d is the perpendicular distance of the line of action from the joint. Using this equation, we see that $\tau_1 = d_1 F = -0.115$ Nm and $\tau_2 = d_2 F = -0.295$ Nm, as shown in Figure 2.6.

However, using Equation 2.2, we can do this by simple matrix multiplication:

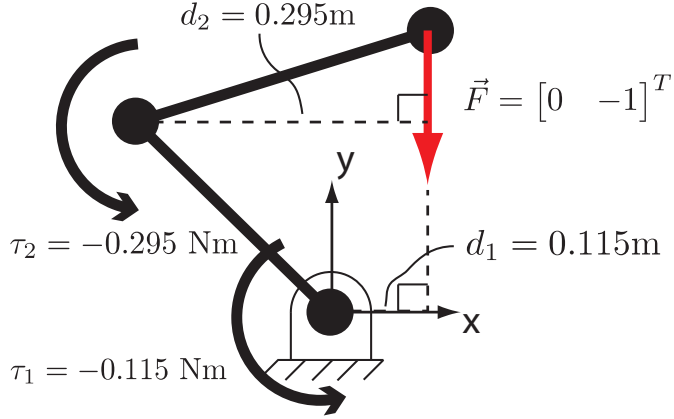


Figure 2.6: Calculation of joint torques using perpendicular distances of line of action from joint axes. Force units are in N.

$$\vec{\tau} = J^T \vec{F} = \begin{bmatrix} -0.259 & 0.115 \\ -0.0787 & 0.295 \end{bmatrix} \begin{bmatrix} 0 \\ -1 \end{bmatrix} = \begin{bmatrix} -0.115 \\ -0.295 \end{bmatrix} \quad (2.16)$$

What if we specify an arbitrary joint torque vector, $\vec{\tau}$? Can we find the force generated at the endpoint, \vec{F} ? The answer is yes, in certain situations, although we will briefly take a look at an example in which this does not work. The simplest case is when we have a square (i.e., invertible, full rank, or non-singular) Jacobian matrix, in which case we can invert the Jacobian transpose matrix in Equation 2.15 and obtain the following equation:

$$\vec{F} = J^{-T} \vec{\tau} \quad (2.17)$$

In this way, we can specify the joint torques found in the arm example and get the force output at the endpoint. An important thing to note, however, is that for this case, finding the force output is dependent on a *pin joint* connection at the endpoint, in which no torque can be applied. Consider the following situation: suppose that there is

a pure moment exerted on the endpoint of 1 Nm. Free-body static analysis will simply reveal that the required joint torques (in Nm) to resist this moment are $\vec{\tau} = \begin{bmatrix} 1 & -1 \end{bmatrix}^T$.

However, if we plug this joint torque vector into Equation 2.17, we get that the endpoint force (in N) is $\begin{bmatrix} 2.67 & -2.67 \end{bmatrix}^T$! Remember that a pure moment was applied with zero force, but using the equation indicates that there was force. However, if the joint is a pin joint, then no torque can be exerted at the endpoint, and Equation 2.17 holds because static equilibrium holds. Note that equations 2.15 and 2.17 are simply a compact way to write the static equilibrium equations for a serial kinematic chain in matrix form (try it!); which implies that to use them properly you must first make sure that you are considering the correct boundary conditions and number of equations to satisfy $\Sigma \vec{F} = 0$ and $\Sigma \vec{\tau} = 0$. Much confusion has arisen in the use of equations 2.15 and 2.17 because some people tend to assume that using those equation suffices to solve the problem (i.e., Jacobians are easy to calculate, rows are easy to delete to make the Jacobian invertible as if by magic), when in reality they represent a very specific version of the equilibrium equations and the user needs to make sure that they are correctly implemented.

The situation becomes even more complicated when the Jacobian is inherently non-square. Take the thumb as an example, with a ball joint connection at the endpoint (i.e., the endpoint is constrained from translation but not rotation). The Jacobian is a 3×5 matrix, and is not uniquely invertible. Only the pseudoinverse may be taken. Without getting into too much detail, the torque vector is 5-dimensional, but the 3-dimensional linear subspace (or hyperplane) spanned by the columns of J^T is the only portion of this 5-dimensional torque space in which pure static x, y, and z-forces will be produced without any self-motion of the thumb (recall that the thumb has 5 DOFs and the spherical

connection only constrains 3 DOFs). Any applied torque combination outside of this 3-D hyperplane will cause the thumb to move along the 2 remaining degrees of freedom that are not constrained. Therefore, if the specified torque vector is located on this 3-D hyperplane, then the pseudoinverse may be used to calculate the endpoint force that is generated by the torque vector ². A more detailed explanation may be found in (Fu & Pollard 2006), but it benefits the reader to at least be aware of this issue with redundant manipulators (or those whose Jacobian is non-square). It can be noted that redundant systems are found throughout the human body, but commercial robotic manipulators tend to be non-redundant to simplify these (and other) issues. In addition, certain cases arise in which the endpoint Jacobian can include one or more angular components (i.e., up to 3 rows, one for each rotational DOF at the endpoint), and then the endpoint boundary conditions become crucial in the analysis. For an example of a special case (the index finger), the reader is referred to (Valero-Cuevas et al. 1998).

²At this point it is useful to underscore properties of non-square matrices that are often not well explored in introductory linear algebra classes. One should build intuition about non-square matrices so that one can begin to relate the different names used for them: A non-square matrix is also non-invertible, which is also called a singular matrix, which is also rank deficient, which also has a determinant equal to zero, etc. If the matrix has more columns than rows, then it also has a nullspace, which means it has a large condition number, or singular values equal to zero, etc. All of these different properties point to the fact that such matrices map from spaces of different dimensions, such that there is no longer a one-to-one mapping between these spaces, or that some points in one space map into the zero point in the other, etc. One should not think of Jacobian matrices as simply an array of numbers, but rather as filters that transform energy from one kind to another (Valero-Cuevas 2005). In this case, we have the mechanical transformation of energy provided by the joint torques into work done by the endpoint forces and vice versa (as per the law of conservation of energy used to derive the Jacobian: Equation 2.7). Thus matrices have gains, preferred input and output directions, etc. Several of these issues will be explored in the present chapter, as when we discuss singular value decomposition, but it is highly recommended that the reader develop an intuition for the properties of rank deficient matrices.

2.2 Tendon routing and moment arms

The purpose of this section is to explore the nuances of tendon-driven systems. Many robotic manipulators are driven by torque motors at each of the joints either by linkages, cables, or gears. These motors are able to exert forces at the various joints in both clockwise and counterclockwise directions, with equal torques and velocities in either direction. While robotic tendon-driven systems can also be actuated via torque motors, they are only able to *pull* on the tendons and not push. This makes tendon-driven systems distinctly different from their idealized torque-driven counterparts. While this one-way actuation might seem like a disadvantage, a tendon-driven manipulator can be designed to have advantages such as light weight, low backlash, remote actuation, and perhaps most importantly, *design flexibility*. As the reader will discover, varying the tendon routing and moment arms of a tendon-driven manipulator enables optimization (which is much more limited with torque-driven systems) for various task requirements, especially when size and power constraints are critical.

As a simple example, Figure 2.7 shows a one DOF manipulator that can rotate a beam around a single joint. We will see how we can offset the bias caused by the mass of a link by using the flexibility of tendon-driven systems by varying moment arms and/or motor strengths. The beam has mass m and length ℓ . If a single torque motor is attached to the beam with maximal torque in either direction τ_{max} , then the motor has to exert $\frac{m\ell}{2}$ units of torque to simply support the weight of the beam, and the remaining torque capacity (in the counterclockwise direction) is $\tau_{max} - \frac{m\ell}{2}$ units of torque, generating up to $\frac{\tau_{max} - \frac{m\ell}{2}}{\ell}$ units of force in the upward direction at the endpoint. Conversely, the maximal

force that is able to be generated in the downward direction at the endpoint is $\frac{\tau_{max} + \frac{m\ell}{2}}{\ell}$, since the manipulator can use the weight of the beam to exert downward force. This is all well and good. However, if we want the manipulator to be able exert equal forces up and down given the maximal torque constraint, this cannot be accomplished with a single torque motor.

Now say that we use 2 tendons, driven by one motor each, and the torque capabilities are identical (i.e., the motors are able to deliver τ_{max} units of torque to the joint in either direction). The pulley size (also, moment arm) of radius r for each tendon is used to actuate the manipulator. This configuration will allow the manipulator to be able to exert the same range of forces as the torque-driven configuration. However, we are easily able to configure the system to be able to exert equal forces in both directions at the endpoint. One solution is divide up the torque capacity so that the motor on the top has $\frac{m\ell}{2}$ maximal units of torque more than the bottom one. This would allow the joint to be able to produce $\tau_{max} + \frac{m\ell}{4}$ units of torque counterclockwise and $\tau_{max} - \frac{m\ell}{4}$ units of torque clockwise at the joint, translating to the endpoint to be able to exert $\frac{\tau_{max}}{\ell}$ units of force in the upward and downward direction after the mass of the beam is taken into account. Alternatively, if size constraints are in place on the total pulley size, we could also let the motors have equal maximal tensions and shift the center of rotation downward so that the larger moment arm is on the top, allowing the torque produced in the counterclockwise direction to be greater than in the clockwise direction in the same manner that we could divide the motor strengths to be able to produce equal force in both upward and downward directions. These designs are illustrated in Figure 2.7.

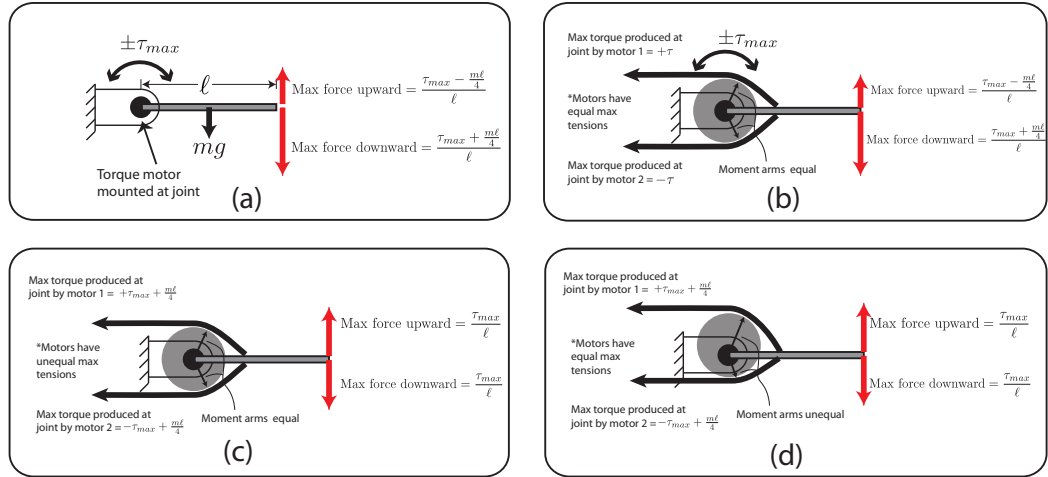


Figure 2.7: A one-DOF manipulator configurations and associated endpoint force production capabilities. (a) Torque motor. (b) Tendons with equal max tensions, equal moment arms. (c) Tendons with unequal max tensions, equal moment arms. (d) Tendons with equal max tensions, unequal moment arms.

While this is not an involved or necessarily realistic scenario, it partially demonstrates the design flexibility offered by a tendon-driven system. In this section, we will briefly discuss i) the definition of versatility, ii) moment arm matrices, which arise from the specific tendon routing and pulley size and type, and iii) necessary conditions for admissible moment arm matrices.

2.3 Definition of necessary actuation: versatility

We will define versatility as the ability to produce a joint torque vector in any direction in torque space (i.e., cover every quadrant of the space). Versatility is always desirable and in most cases necessary for adequate function of a manipulator. Versatility of the endpoint is easy to check once the feasible torque set of the manipulator is determined. If the feasible torque set (described in Section 3) encloses the origin, then the endpoint can produce at

least some force in any direction (if the Jacobian is full rank). In certain situations in which joints are coupled (e.g., coupling of the distal and proximal interphalangeal joints of the index finger), the manipulator can produce force in any direction without being necessarily versatile, as defined here.

For a tendon-driven manipulator to be versatile, it must have a tendon routing described by an *admissible* moment arm matrix (further details in a section below). Admissible moment arm matrices are those that enable independent control of all of the joints *in both directions*. If the Jacobian of the manipulator is full rank, then an admissible moment arm matrix implies versatility, and vice-versa.³

2.3.1 Moment arm matrices

A moment arm matrix, R , is an $m \times n$ matrix, where m is the number of joints and n is the number of tendons of the manipulator. The entries are $r_{i,j}$, which is a signed moment arm value (positive values indicate positive torque generated at a joint when tension is applied to the tendon, and v-v), i is the joint number and ranges from 1 to m , and j is the tendon number, which ranges from 1 to n . The moment arm matrix can be used to transform tendon tensions to joint torques using the following equation:

$$\vec{\tau} = R\vec{T} \quad (2.18)$$

³The nuance here is that one can have a non-convex feasible torque set that is made of thin lines that enter each quadrant, but cannot go everywhere (i.e., cover an area) in the neighborhood of the origin.

Therefore, if tendon tensions are specified, the joint torques are uniquely specified. This is not true in the reverse case, as we will soon see. Two example robotic fingers and their associated moment arm matrices are shown in Figure 2.8.

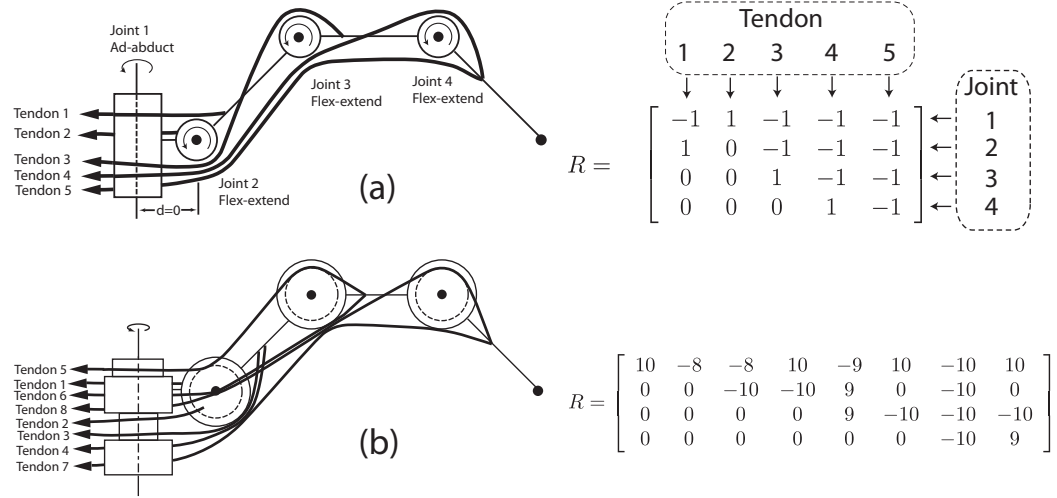


Figure 2.8: Fundamental relationship between tendon routing and moment arm matrices. Tendon layout of 2 4-DOF robotic fingers and their associated moment arm matrices. (a) All equal moment arms. (b) Varying moment arms. Not to scale. Note that this figure underscores how a given tendon routing drawing has a corresponding moment arm matrix, and vice versa.

We can observe the systematic way in which the moment arm matrix is constructed.

In the simple finger in Figure 2.8a, let us look at Tendon 1. It crosses joints 1 and 2, and its moment arm values are contained in the first column of the R matrix. It will produce a negative motion or force around the first joint (using the right-hand rule), so the entry in the first row is -1. It will produce a positive motion or force around the second joint, so the entry in the second row is +1. It does not cross the other joints, so the moment arm value at those joints is zero. The rest of the R matrix is similarly constructed.

We can see that the design space for the moment arm matrix of a multi-joint, tendon-driven system is very high-dimensional. The finger in Figure 2.8a has a 20-dimensional

design space (i.e., there are 20 entries that define the tendon routing and moment arms) and the finger in Figure 2.8b has a 32-dimensional design space. Even if we only use 3 possible values for the moment arm matrix entries—1, 0, and -1, the 20-dimensional design space will have $3^{20} \approx 3.5$ billion possibilities. If we use the 32-dimensional design space, there will be $3^{32} \approx 1.9 \times 10^{15}$ possibilities! And keep in mind that this is not considering that moment arm values are not discreet and can be varied to any desired size. How is a designer ever to choose a moment arm matrix for a system given such a large design space? Thankfully, the mathematical theory behind moment arm matrices limits the design space of moment arm matrices to a subset of matrices which are admissible (i.e., to make the system versatile). In addition, the computational analysis which we will discuss later in the chapter can be used to optimize manipulator performance based on certain task requirements. In this next section, we will briefly go over the necessary conditions for an admissible moment arm matrix.

2.3.2 Necessary conditions for admissible moment arm matrices

The three necessary conditions for an admissible moment arm matrix R (i.e., versatile in the sense that provides for independent controllability of all of the degrees of freedom of the manipulator) for a manipulator with n degrees of freedom are as follows (Sheu et al. 2009, Tsai 1999):

1. The rank of the moment arm matrix R must be n (i.e., full row rank, even if non-square ⁴).

⁴Recall that for a matrix to be full row rank it needs all its rows to be linearly independent (i.e., no one row can be found by linear combinations of the other rows). Thus even if the matrix is ‘wide and has many more columns than rows (i.e., more tendons than joints, and is therefore non-square), it can still have full row rank

2. The null space of R must contain at least one vector in which all the elements are of the same sign.
3. There are at least 2 nonzero elements in each row and there must be at least one sign change between elements in each row.

The first condition is necessary for manipulator versatility. In this context, we define manipulator versatility as the ability to control each joints angular position, velocity, and/or torque independently. Technically, if the tendons were able to both push and pull (i.e., if they were rods like for the swash plate of helicopter rotors, or Stewart platforms), this condition alone would be necessary and sufficient for manipulator versatility. The second and third conditions are necessary due to the tendon-driven nature of the system. The second condition ensures that there is at least one combination of tendon tensions that will produce no net torque on the joints (and hence no net force at the endpoint). We will soon see that this is necessary for the calculation of feasible solutions for tendon tensions given a desired output, since none of the tendons may exert negative tension. The third condition ensures that there is a minimum of one tendon routed on each side of the joint so that it can exert torque (and produce angular velocity) in both directions for each joint, due to the tension-only nature of tendons.

Let us now examine an equation that relates joint torques to tendon tensions. Assuming that the moment arm matrix satisfies the above 3 conditions, we can find a least-squares solution for tendon tensions given a desired set of joint torques using the pseudoinverse of R :

$$\vec{T} = R^+ \vec{\tau} \quad (2.19)$$

However, given that the pseudoinverse provides the least squares solution to the invertibility problem, there is bound to be at least one negative element in the predicted solution for the vector of tendon tensions. But again, because tendons can only pull, any implementable solution requires that all of the elements of the tension vector be non-negative. Therefore one should also use the basis vectors for the null space of R to find solutions that satisfy this non-negativity requirement ⁵. The following equation contains both the *particular* solution, also given in Equation 2.19, and the *homogeneous* solution (the second term on the right side of the following equation):

$$\vec{T} = R^+ \vec{\tau} + H \vec{\lambda} \quad (2.20)$$

where H is a matrix whose columns are the null vectors of R , and $\vec{\lambda}$ is an arbitrary vector of constants. Any $\vec{\lambda}$ vector may be chosen without affecting the joint torques. Therefore, it can be adjusted freely to make all tensions positive, given that the second necessary condition is satisfied.

As an extremely simple example, let us turn again to a one-DOF manipulator, shown in Figure 2.9a. We will assume the beam is massless for this example. The 2-D Jacobian for this manipulator is $\begin{bmatrix} 0 & \ell \end{bmatrix}^T$. If we want to exert 1 unit of force in the upward direction, then we can use Equation 2.15 to get the necessary torque $\tau = J^T \vec{F} = \begin{bmatrix} 0 & \ell \end{bmatrix} * \begin{bmatrix} 0 & 1 \end{bmatrix}^T = \ell$ at the joint. The moment arm matrix R for this system is a 1×2 matrix equal

⁵Recall that the null space is the set of all \vec{x} vectors that satisfy the equation $A\vec{x} = \vec{0}$

to $\begin{bmatrix} 1 & -1 \end{bmatrix}$, assuming a moment arm radius of 1 unit for each tendon. Although the necessary conditions may seem trivial for this example, they are all satisfied. The matrix is clearly full row rank (i.e., it only has one row. It is non-square because it has more tendons than joints). To determine a basis for the null space of R (which is only one-dimensional in this case. See (Strang 2003) for a review of this topic), we can use singular value decomposition (See Section 3.3 and (Strang 2003)) which yields a null vector of $\begin{bmatrix} -0.707 & -0.707 \end{bmatrix}^T$, shown in Figure 2.9b. This satisfies the second necessary condition. The third necessary condition is also satisfied since there is a sign change between elements in the only row of R . Since we want a torque of ℓ , we can use the particular solution of Equation 2.20 and the pseudoinverse $R^+ = \begin{bmatrix} 0.5 & -0.5 \end{bmatrix}^T$ to determine that the least-squares solution is $\vec{T} = R^+ \vec{\tau} = \begin{bmatrix} 0.5 & -0.5 \end{bmatrix}^T \ell = \begin{bmatrix} 0.5\ell & -0.5\ell \end{bmatrix}^T$. Now, since we must make all tensions non-negative, we can use the homogeneous solution with the arbitrary constant λ . We have the null space of R , which we substitute in for H , shown in Figure 2.9c.

Now if we choose $\lambda = -0.5/0.707$, then we get a tension vector $\vec{T} = \begin{bmatrix} \ell & 0 \end{bmatrix}$. Now the tendon tensions are non-negative and the desired force output is generated! We could also have chosen a lambda that was higher than the one chosen, which would have produced equally higher tensions in both tendons, which would cancel each other out and the output force would be the same. In biomechanical terms, this would be known as *co-contraction*, where muscles on either side of a joint are active with no net endpoint output force generated.

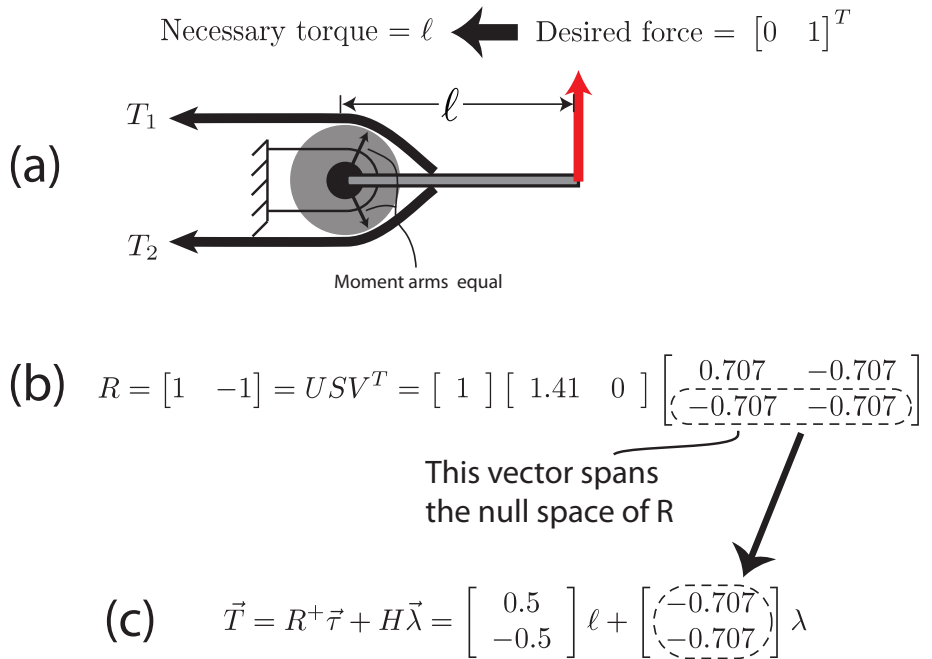


Figure 2.9: (a) A one-DOF manipulator. (b) Determination of null space of R with singular value decomposition. (c) Calculation of solution for tendon tensions, given desired joint torque.

2.4 Discussion

In summary, while we see that these 3 necessary conditions definitely eliminate some designs from the large, high-dimensional design space that was discussed earlier, the space is still very large and suffers from the curse of dimensionality when trying to optimize tendon driven systems that have more than a few tendons. This necessitates computational tools for quickly evaluating the fitness of a particular moment arm matrix given a specific or general set of tasks. In addition, it begins to suggest that analytical, closed form solutions are not available for tendon-driven systems because tools such as singular

value decomposition assume symmetry of actuation. Thus, in Section 3 we go on to introduce an alternative approach based on computational geometry that enables a more complete and accurate treatment of these systems.

Chapter 3

Fundamentals of Feasible Sets

3.1 Forward analysis I: from feasible activation sets to feasible force sets using vertex enumeration.

Having introduced the fundamentals of tendon driven systems, we now begin to describe in detail several analysis approaches and tools to understand the capabilities of a given manipulator design. Knowing the workspace of a manipulator (i.e., the set of postures it can achieve and the endpoint locations it can reach) is critical to the design and control of its kinematics, see (Yoshikawa 1990) for details. Similarly, knowing the set of all possible endpoint forces and torques a manipulator design can produce is critical to the design and control of its kinetics. We can analyze the kinetostatic (i.e., static force production) capabilities of manipulators using forward analysis. The term ‘forward’ is used because it recapitulates the order in which a robotic manipulator is usually controlled: you deliver select torques to the joints to produce desired endpoint forces and torques. This approach uses a computational geometry analysis in which we map the set of all feasible commands to its actuators (the feasible activation set, which we will describe shortly) through the

manipulator to find the set of endpoint forces that the mechanism can generate. To perform this forward analysis, we need the manipulator Jacobian J , the moment arm matrix R , and the diagonal matrix of maximal tendon tensions F_0 (See (Valero-Cuevas 2005)). This is the opposite of inverse analysis, which maps forces at the endpoint back to activation vectors, and which will be described in a later section. Figure 3.1 illustrates the forward mapping of feasible activation sets to feasible force sets, using the arm example shown in previous sections. We will give it 6 tendons (actuated by muscles).

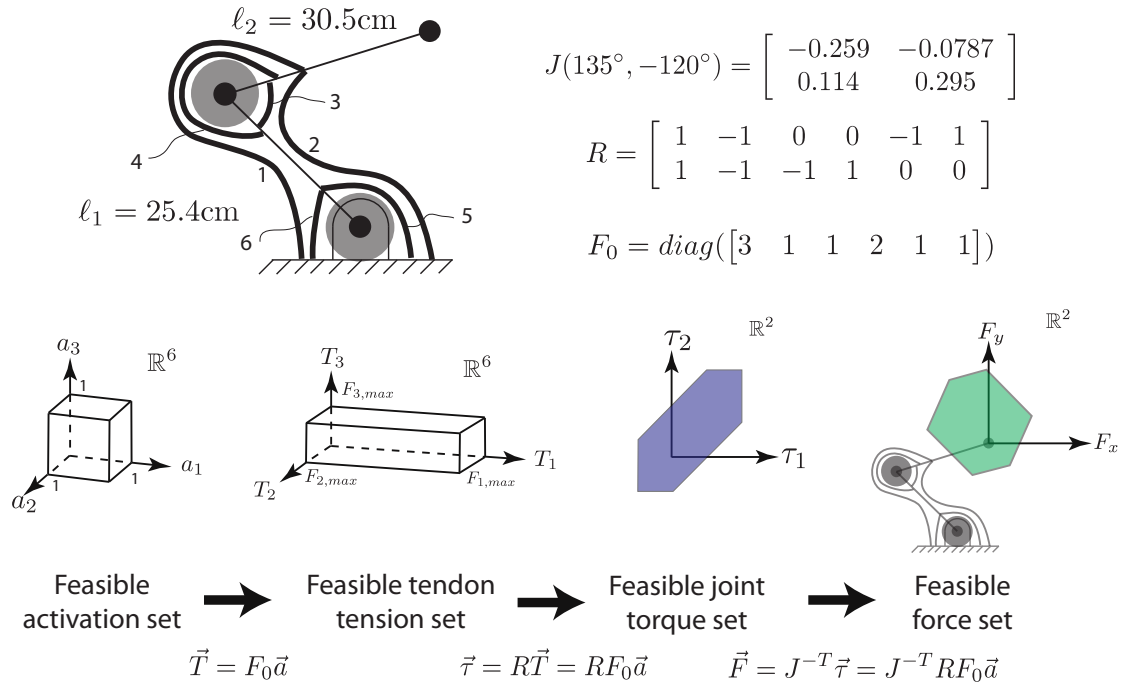


Figure 3.1: Forward mapping of feasible activation set to feasible force set. Note: the feasible activation set and the feasible tendon tension set for this example are both in \mathbb{R}^6 , but only 3 dimensions are shown.

Please note that we use the term ‘activation’ to mean (in the physiological sense) the intensity with which a muscle is driven by the neural system), or (in the robotic sense) to mean the tension level in a tendon.

Thus, a feasible activation set is the set of all feasible activations of muscles, or tensions in tendons where activation levels are normalized to range between 0 and 1, with 0 being no activation of a tendon (and therefore no tension) and 1 being full activation of a tendon (or maximal tension). The mapping from an activation vector \vec{a} to a tendon tension vector \vec{T} is given by the following equation (for an overview of this topic see(Valero-Cuevas 2005)):

$$\vec{T} = F_0 \vec{a} \quad (3.1)$$

As was noted earlier, F_0 is a diagonal matrix whose elements correspond to the maximal tensions (or muscle forces, in the physiological sense) of each tendon. This equation transforms a vector of normalized activations to a vector of tendon tension scaled to the capabilities of the muscles or motors driving the system. To find the entire feasible tendon tension set, all we need to do is map each vertex of the feasible activation set (i.e., each vertex of the unit hypercube in the positive orthant) into the feasible tendon tension set via the F_0 matrix (See Figure 3.1, (Valero-Cuevas et al. 1998, Valero-Cuevas 2005)). Essentially, we scale the n-cube ¹ that defines and contains the convex set of all possible combinations of activation vectors ² in to an n-dimensional parallelepiped of tendon tensions. This is because F_0 matrix is a diagonal matrix, so each activation level gets mapped into a tension value in units of force.

¹A unit cube in the n-dimensional space of number of tendons

²Where a given activation pattern is a point belonging to this n-dimensional cube

After we have the feasible tendon tension set, we can map it to the feasible joint torque set through the moment arm matrix R using the following equation (See Figure 3.1, (Valero-Cuevas et al. 1998, Valero-Cuevas 2005)):

$$\vec{\tau} = R\vec{T} \quad (3.2)$$

Once again, we can map each vertex of the feasible tendon tension set to a vertex of the feasible joint torque set. After mapping all the vertices in this way, the feasible joint torque set is the convex hull of these vertices. Note that at this point we are able to define the set of all possible net joint torques the tendons are able to produce. The size and shape of the feasible torque set will depend on the properties of the moment arm matrix R ³. A geometric analogy is that of casting the shadow of a parallelepiped (like a white- or black-board eraser) onto a plane. This would be a mapping from \mathbb{R}^3 to \mathbb{R}^2 (three muscles and two joints). Try then to change the orientation of the parallelepiped to see how the number of vertices, size and shape of the shadow can change. In all cases, however, the vertices of the 2D projection are a function of the vertices of the 3D object.

Next, we can map the feasible joint torques to endpoint forces (if the proper endpoint boundary conditions are in place and the Jacobian is square and invertible, as discussed in Section 2; in this example, we assume a pin joint which is the proper condition for this analysis, and the Jacobian is square— 2×2). To do this, and assuming the proper conditions, we can use the following equation to map feasible joint torque set vertices to feasible force set vertices:

³for the sake of simplicity we restrict ourselves to constant moment arms (i.e., which would arise from circular pulleys, but in reality these can change with posture so one would define $R(\vec{q})$).

$$\vec{F} = J^{-T} \vec{\tau} \quad (3.3)$$

Then the feasible force set will be the convex hull of these vertices in endpoint force space. Figure 3.1 shows all of these steps, given the parameters shown. It can be observed that the moment arm matrix satisfies all of the necessary conditions for full controllability, discussed in the previous section. First, it is full rank. Second, SVD gives 4 null vectors:

$$\begin{aligned}\vec{v}_1 &= \begin{bmatrix} 0.289 & -0.5 & 0.789 & 0.211 & 0 & 0 \end{bmatrix}^T \\ \vec{v}_2 &= \begin{bmatrix} -0.289 & 0.5 & 0.211 & 0.789 & 0 & 0 \end{bmatrix}^T \\ \vec{v}_3 &= \begin{bmatrix} 0.289 & 0.5 & 0.289 & -0.289 & 0.5 & 0.5 \end{bmatrix}^T \\ \vec{v}_4 &= \begin{bmatrix} -0.289 & -0.5 & -0.289 & 0.289 & 0.5 & 0.5 \end{bmatrix}^T.\end{aligned}$$

Adding \vec{v}_1 , \vec{v}_2 , and \vec{v}_3 gives a vector in the null space $\vec{v}_{null} = \begin{bmatrix} 0.289 & 0.5 & 1.289 & 0.711 & 0.5 & 0.5 \end{bmatrix}^T$ that satisfies the second necessary condition of all elements being of the same sign. Lastly, there is at least one sign change between elements in each row of R , which satisfies the third necessary condition.

The entire analysis, from feasible activation sets to feasible force sets (for square, invertible Jacobians—not the general case), can be summarized by the following equation (Valero-Cuevas et al. 1998):

$$\vec{F} = J^{-T} R F_0 \vec{d} \quad (3.4)$$

What happens in the general case when the Jacobian is non-square and therefore the last transformation using J^{-T} between feasible torque sets and feasible force sets is not possible? Well, we must modify this last transformation from feasible joint torques to feasible endpoint forces by first intersecting the feasible torque set with the linear subspace spanned by the columns of J^T (Fu & Pollard 2006). The vertices of this reduced-dimensionality set can then be transformed to endpoint force space using the pseudoinverse so that $\vec{F} = J^{+T}\vec{\tau}$. The 5-DOF thumb in Figure 3.2 is a case of a non-square Jacobian, and determination of the feasible force set using this method produces the feasible force set shown in Figure 3.2 using the parameters shown.

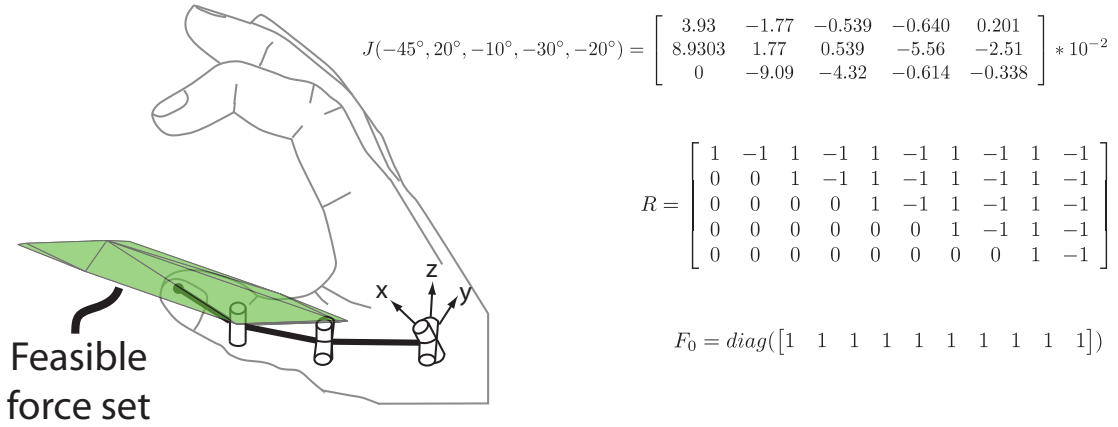


Figure 3.2: 3-D Feasible force set of 5-DOF finger using parameters shown.

3.2 Forward analysis II: from basis vectors to feasible sets using Minkowski sums.

As an alternative to the vertex enumeration approach described above, we can also think of the capability of each tendon as being represented by a “basis vector” in the following spaces:

1. Activation space
2. Tendon tension space
3. Torque space
4. Force space

Taking the convex hull of the Minkowski sum (all positive additions) of these basis vectors in their respective spaces can then be used to build the feasible set in that space

⁴. Basis vectors and their corresponding feasible sets are shown in Figure 3.3.

3.3 Why SVD is not the correct approach for analysis of tendon-driven systems

Singular value decomposition (SVD) has been used typically in the past for analysis of the force and velocity-production capabilities of manipulators at their endpoint (Yoshikawa 2002, Valero-Cuevas 2005). This approach produces what are called the manipulability

⁴It is important to note that the notion of basis vectors in force space is only valid if the Jacobian is square and invertible, since the basis vectors in torque space can only be transformed to basis vectors in force space through J^{-T} . If the Jacobian is non-square, then the vertex enumeration approach is necessary to build the feasible force set, as described in the previous section.

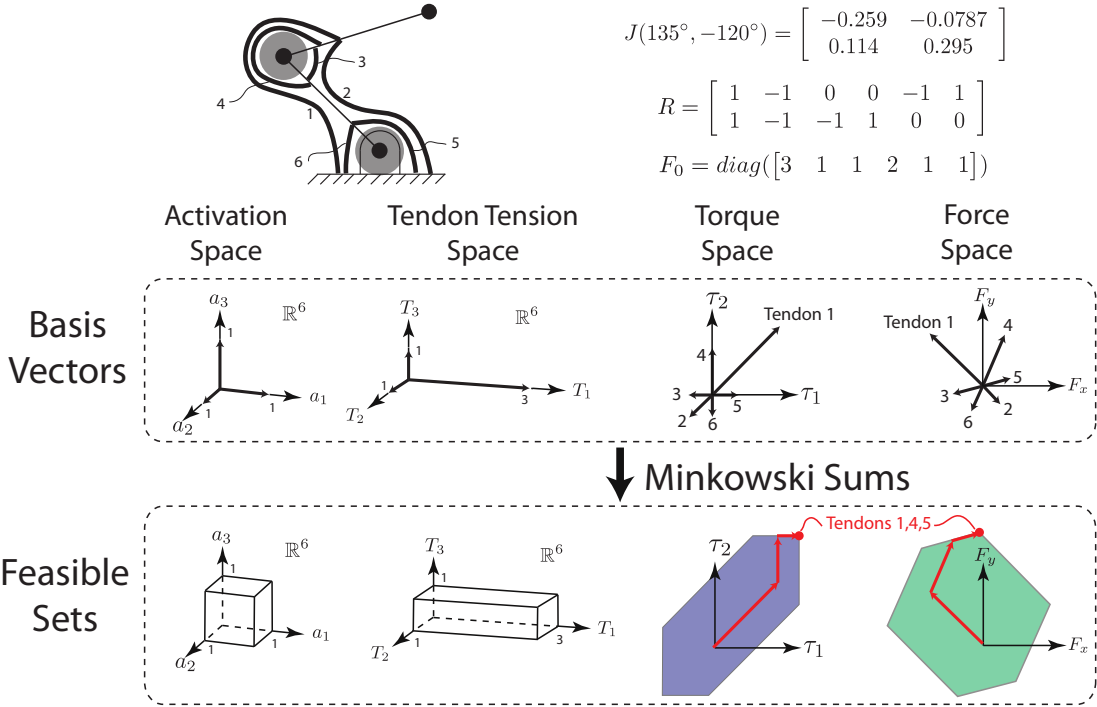


Figure 3.3: Demonstration of the duality between basis vectors and feasible sets.

and manipulating force ellipsoid that, respectively, describe the directions in which the endpoint velocities and forces can be produced with greatest and least ease. While very valuable, this analysis assumes that the feasible joint angular velocity set (i.e., the set of possible combinations of joint angular velocities) is a sphere in joint angular velocity space (i.e., $\|\dot{q}\| = (\dot{q}_1^2 + \dot{q}_2^2 + \dots + \dot{q}_n^2)^{1/2} \leq 1$, where n is the number of joints in the manipulator), and that the feasible joint torque set is a sphere in joint torque space (i.e., $\|\vec{\tau}\| = (\tau_1^2 + \tau_2^2 + \dots + \tau_n^2)^{1/2} \leq 1$). These assumptions are somewhat reasonable with torque motors at the joints, and enables a quick and easy method for determining the feasible endpoint velocity or force *ellipsoids* (manipulability and manipulating force ellipsoids, respectively). The manipulability ellipsoid comes from the SVD of the Jacobian J , and

the manipulating force ellipsoid from the SVD of the pseudoinverse (or inverse, if the Jacobian is square) of the Jacobian transpose J^T . The SVD of a matrix A is:

$$A = U\Sigma V^T \quad (3.5)$$

Where Σ is a diagonal matrix containing the singular values, in descending order, that indicate the highest and lowest gains the matrix can produce. The rows of V^T contain the right singular vectors. These row vectors are the directions in the input space, ordered from top to bottom, that are magnified by the corresponding singular values. The columns of U contain the left singular vectors. These row vectors are the directions in the output space, ordered from left to right, that are magnified by the corresponding singular values. Thus, if we assume the input space is a unit sphere, SVD describes the direction in output space where the output will be greatest (i.e., the leftmost column of U) and smallest (i.e., the rightmost column of U). Thus, the left singular vectors of J or J^{+T} (or J^{-T} , if the Jacobian is square) define the major axes of the feasible velocity or force ellipsoid, respectively, of the endpoint, and the corresponding singular values define the length of these axes. For an example of this analysis, the reader is referred to (Valero-Cuevas 2005). It has been noted that analysis based on ellipsoids is not as accurate a representation as using polytopes describing the feasible output set, in which the feasible joint torque or velocity set is a hypercube or parallelepiped rather than a sphere (i.e., $|\dot{q}_i| \leq \dot{q}_{i,max}$ or $|\tau_i| \leq \tau_{i,max}$) (Finotello et al. 1998). Furthermore, even if the vertex enumeration analysis is carried out to find such polytopes of feasible output, it is only correct for torque-driven manipulators in which the motors can produce equal amounts of force and/or velocity

in both directions at the joints. For the case of tendon-driven manipulators where the feasible inputs are hypercubes or parallelepipeds in the first, or all positive, octant the assumptions of input unit spheres is violated and thus SVD does not offer an accurate representation of their output capabilities.

We illustrate the ways in which analysis with manipulating force ellipsoids can lead to false impressions of the endpoint force capabilities of tendon-driven manipulator using the simple arm example, shown in Figure 3.4. We see that the manipulating force ellipsoid generated from singular value decomposition of the J^{-T} matrix for the arm generates a manipulating force ellipsoid with a certain alignment (given by the left singular vectors of J^{-T}) and length (given by the singular values of J^{-T}) of the major axes of the ellipsoid. This is the feasible force set if the Euclidean norm of the *joint torque vector* is bounded by a constant value (i.e., the feasible torque set lies inside the unit circle, or generally, sphere).

However, the feasible torque set for the tendon-driven arm is not a circle, but is a polygon (or generally polytope, if the dimensionality is higher than 2) in torque space, shown in Figure 3.4. We see that the manipulating force ellipsoid differs greatly in size, shape and orientation from its feasible force set, Figure 3.4. We see that changing the moment arm matrix, the maximal tendon tensions, or any combination of the two results in differing shapes and sizes of the feasible torque sets and feasible force sets. The arm in Figure 3.4a is better at producing force in the positive-y direction, while the arm in Figure 3.4b is better at producing force in the negative-y direction. This distinction is not possible with manipulating force ellipsoid analysis using SVD.

$$R = \begin{bmatrix} 1 & -1 & 0 & 0 & -1 & 1 \\ 1 & -1 & -1 & 1 & 0 & 0 \end{bmatrix} \quad R = \begin{bmatrix} 1 & -1 & 0 & 0 & -1 & 1 \\ 1 & -1 & -1 & 1 & 0 & 0 \end{bmatrix} \quad R = \begin{bmatrix} 2 & -0.7 & 0 & 0 & -1 & 1 \\ 2 & -0.4 & -1.3 & 1 & 0 & 0 \end{bmatrix}$$

$$F_0 = \text{diag}([3 \ 1 \ 1 \ 2 \ 1 \ 1]) \quad F_0 = \text{diag}([1 \ 3 \ 1 \ 1 \ 1 \ 3]) \quad F_0 = \text{diag}([3 \ 1 \ 1 \ 2 \ 1 \ 1])$$

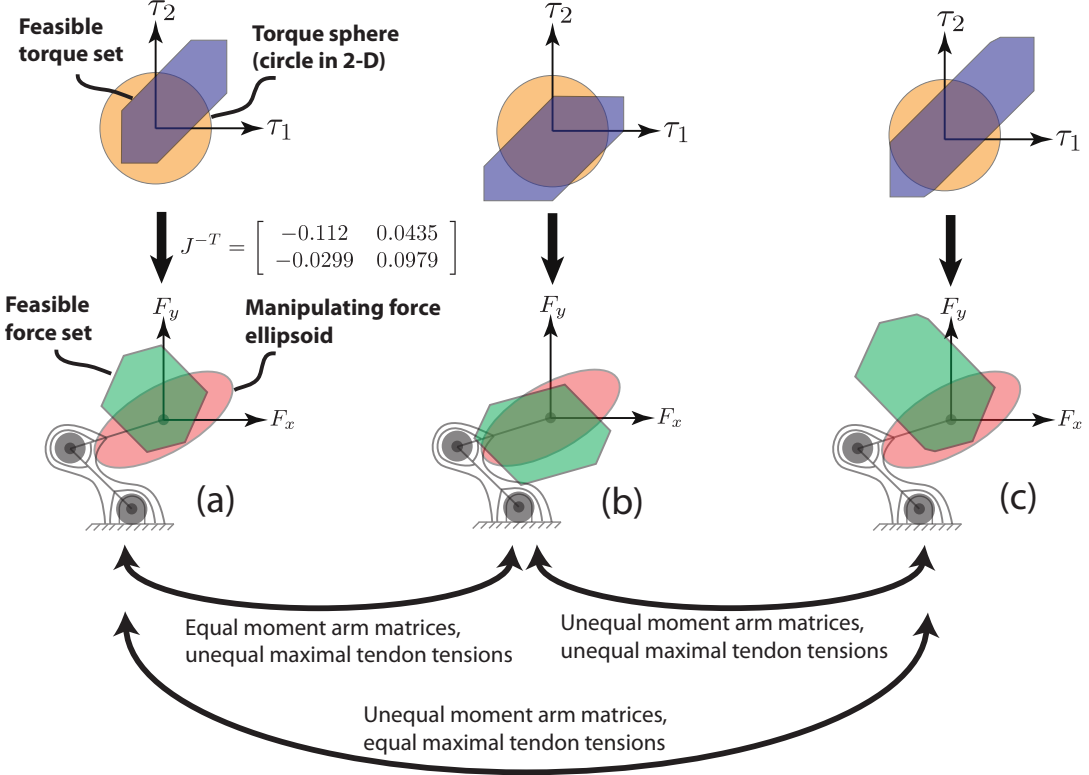


Figure 3.4: Illustration of why manipulating force ellipsoids do not accurately capture the force-production capabilities of tendon-driven manipulators.

3.4 Other cases

While we have focused on the feasible force sets of serial chain manipulators up until this point, there are other analyses that involve other feasible sets, including feasible wrench sets, feasible velocity sets, feasible twist sets, and feasible acceleration sets. We will briefly discuss each of these feasible sets.

3.4.1 Feasible wrench sets

A wrench refers to a force-torque combination, and it can be up to 6-dimensional at a manipulator endpoint (3-D forces and 3-D torques). The analysis we have presented thus far involves 2-D or 3-D forces only, with a pin joint or ball joint connection boundary condition at the endpoint. However, if we have a redundant manipulator (i.e., more than 2 DOFs for a planar manipulator or more than 3 DOFs for a 3-D manipulator), we can normally exert one or more torques about the endpoint if it is constrained from rotation.

As a simple example, let us examine a planar 3-DOF manipulator, shown in Figure 3.5. The endpoint is constrained from any rotation or translation by a fixed boundary condition in Figure 3.5a. Translations in the x- and y-directions are constrained and rotation at the endpoint around the z-axis is constrained. Therefore, all 3 DOFs have been constrained. This is distinctly different from a pin joint, in which rotation is allowed. If a pin joint is present, shown in Figure 3.5b, then only the x- and y-translations are constrained and therefore there is an extra degree of freedom in the rotation of the endpoint, so the manipulator may take on multiple configurations, each having a different endpoint orientation angle but the same translational coordinates, shown also in Figure 3.5b. The translational Jacobian J for this manipulator is a 2×3 matrix, which has a null space of one dimension. If a joint angular velocity vector $\dot{\vec{q}}$ is a scalar multiple of the null vector (or in the general case, if the joint angular velocity vector lies in the linear subspace spanned by the null vectors of J), then the endpoint velocity (translational) will be zero and there will be what is termed *self-motion* of the manipulator (i.e., motion of the

finger without translational movement of the endpoint (Valero-Cuevas et al. 1998, Valero-Cuevas 2005)).

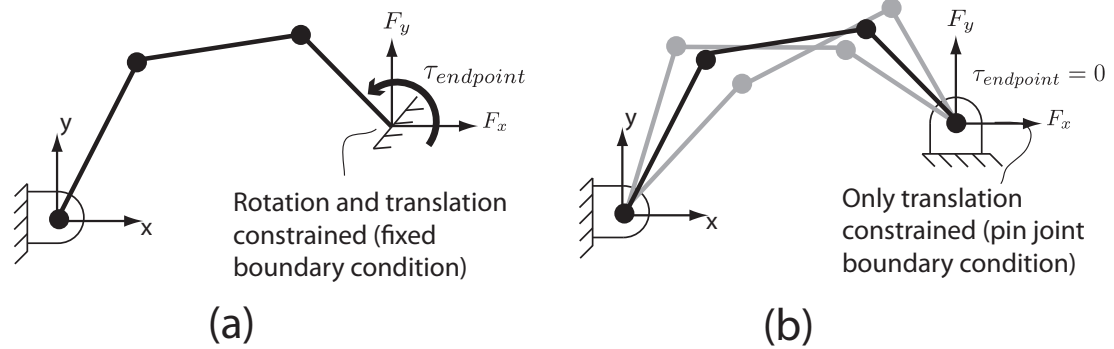


Figure 3.5: Differing endpoint conditions affect feasible wrench set analysis for 3-DOF planar manipulator. (a) Fixed boundary condition, 3 DOFs constrained. (b) Pin joint boundary condition, 2 DOFs constrained.

Due to this possibility of self-motion, there is also the possibility of controlling the endpoint torque by using specific combinations of joint torques if the rotation of the endpoint is constrained. A Jacobian that has 2 translational components and one rotational component can be defined if the endpoint position/rotation vector is defined as $\begin{bmatrix} x & y & \alpha \end{bmatrix}^T$ (where α is the angle of the endpoint in relation to the global reference frame) rather than only a position vector $\begin{bmatrix} x & y \end{bmatrix}^T$. Also, since the manipulator has 3 DOFs, it can independently control the x-force, y-force, and endpoint torque $\tau_{endpoint}$. If the Jacobian is constructed to have 2 translational components and one rotational component, it is then a 3×3 matrix and can be inverted (unless the manipulator is in a singular configuration in which case the matrix is also singular and not invertible). The static endpoint output is no longer just a force vector with x- and y-components, but also has the endpoint torque component. This force/torque combination is called a *wrench*.

vector \vec{w} , and for this manipulator it is the vector $\begin{bmatrix} F_x & F_y & \tau_{endpoint} \end{bmatrix}^T$. Equation 2.15 can then be written as

$$\vec{\tau} = J^T \vec{w} \quad (3.6)$$

The last column of J^T is the joint torque vector that, when applied (or any scalar multiple), will result in only endpoint torque and zero endpoint force.

For this manipulator, since the Jacobian is square and invertible, then Equation 3.4 can be rewritten to calculate the endpoint wrench as

$$\vec{w} = J^{-T} R F_0 \vec{a} \quad (3.7)$$

and therefore the transformation from feasible activation sets to feasible wrench sets is simplified. An example of a feasible wrench set analysis using a square 4×4 Jacobian can be found in (Valero-Cuevas et al. 1998). It should be noted that that example as well as the example presented above are special cases, and further analysis of *self-motion manifolds* (Burdick 2002) are necessary in general to create a square Jacobian in the general case of translational redundancy. There will be 2 “instantaneous” (i.e., for a specific set of joint angles) self-motion manifolds of the 5-DOF thumb for a given posture, corresponding to 2 dimensions along which torque may be exerted. The 2 dimensions that torque may be exerted, however, are not of constant global orientation and they change with posture. Therefore, it is not possible to simply use a 5×5 square Jacobian (3 global translational components and 2 global rotational components) for use in Equation 3.7

that holds for all sets of joint angles. To the best of our knowledge, no one has ever published results on using square Jacobians in the general case for obtaining the feasible wrench set for (translationally) redundant manipulators.

3.4.2 Feasible velocity and twist sets

As mentioned earlier, singular value decomposition (SVD) has been used to analyze the manipulability ellipsoids of the endpoint of a manipulator. Now we are referring to the feasible velocities that the endpoint can generate and not the forces (which are termed manipulating force ellipsoids). SVD of the manipulator Jacobian J can be used to obtain the orientation (given by the left singular vectors of J) and length (given by the non-vanishing singular values of J) of the major axes of the ellipsoid which encloses the feasible velocities of the endpoint, given that the joint angular velocity vector lies within the unit ball (i.e., $\|\dot{q}\| = (\dot{q}_1^2 + \dot{q}_2^2 + \dots + \dot{q}_n^2)^{1/2} \leq 1$). However, as noted before, the assumption that the Euclidean norm of the joint velocity vector is limited is not realistic, and for torque-driven systems, a more realistic assumption is that each joint velocity is limited (i.e., $|\dot{q}_i| \leq \dot{q}_{i,max}$).

However, for tendon-driven systems, the analysis of feasible velocity sets becomes much more complex than the analysis of feasible force sets. This is due to the mathematics of the analysis: in the force domain, superposition may be used and therefore vector addition types of operations are appropriate, whereas in the velocity domain, $\min(\cdot)$ types of operations are necessary for analysis rather than addition. To illustrate, we will turn to our trusty one-DOF manipulator, shown in Figure 3.6. We shall assume that the maximal tendon forces for each of the three tendons are equal and also that their

maximal velocities are also equal. If we are doing a force analysis, it is trivial to see that twice as much force can be exerted downward as upward, since we can activate both tendons 2 and 3 at the same time, producing twice the force downward that would be exerted by tendon 1 upwards if it was fully activated (note that we are neglecting the weight of the beam). So the force production capabilities of the endpoint are clearly asymmetrical. If we activate the maximal velocity of tendon 1, we get a certain maximal upward velocity v_{max} . However, we cannot get $2v_{max}$ velocity in the downward direction since the velocities will not add like forces do. If one of either tendons 2 or 3 has less maximal velocity, then the maximal endpoint velocity will be limited by the tendon with less maximal velocity. This is why a $\min(\cdot)$ operator is more appropriate than an addition operator. We are assuming that we do not want any of the tendons to go slack at any time, and that dynamical effects are not involved (the latter is a very questionable assumption, see below).

A specific joint angle velocity vector $\dot{\vec{q}}$ requires a specific tendon excursion velocity vector $\dot{\vec{s}}$. If the desired joint angle velocity vector is known, then the maximal magnitude of this vector is limited by one or more tendons when they reach their maximal velocities. To the best of our knowledge, the problem of computing the complete set of feasible velocities of the endpoint for a tendon-driven system has never been solved.

Twists are velocity vectors that have translational and rotational velocity components. Feasible force sets and feasible velocity sets are only concerned with translational components, whereas feasible wrench and twist sets are concerned with both translational and rotational components. The calculation of feasible twist sets is more involved than

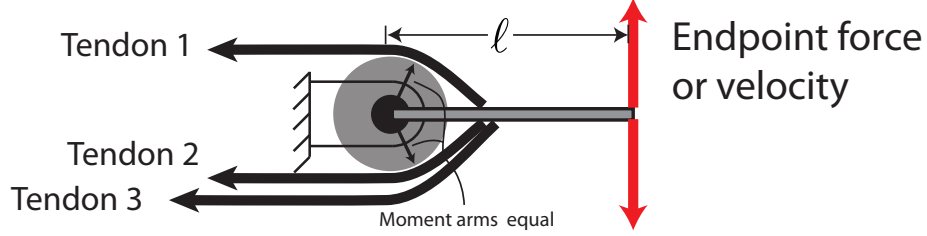


Figure 3.6: One-DOF manipulator.

the calculation of feasible velocity sets. Differing formulations of the Jacobian to include rotational components can be used to employ ellipsoidal measures of feasible twist sets.

3.4.3 Feasible acceleration sets

Feasible acceleration sets can be generated for manipulators if the kinetic characteristics of the systems are known (i.e., mass of each link and gravity constant). A general formulation for the dynamics of a tendon-driven system is given by the following equation (Kuo & Zajac 1993):

$$M(\vec{q})\ddot{\vec{q}} = R(\vec{q})\vec{T} + V(\vec{q}, \dot{\vec{q}}) + G(\vec{q}) \quad (3.8)$$

where M is the mass matrix, \vec{q} is the vector of joint angles, R is the moment arm matrix, \vec{T} is the column vector of tendon tensions, $V(\vec{q}, \dot{\vec{q}})$ is the vector of velocity-dependent terms (i.e., Coriolis forces), and G is the vector of gravity-dependent terms. If the initial configuration is static (i.e., $\dot{\vec{q}} = 0$, then the velocity term $V(\vec{q}, \dot{\vec{q}})$ is equal to zero and the joint angular accelerations can be written as a linear function of tendon tensions:

$$\ddot{\vec{q}} = M(\vec{q})^{-1}(R(\vec{q})\vec{T} + G(\vec{q})) \quad (3.9)$$

The feasible acceleration set can then be built up from the feasible tendon tension set (or alternatively, we may substitute $F_0\vec{a}$ for \vec{T} in Equation 3.9 and then build up the feasible acceleration set from the feasible activation set). In Equation 3.9, the angular acceleration vector $\ddot{\vec{q}}$ is linear with respect to the tension vector \vec{T} (also, the activation vector \vec{a}) if the manipulator is in a quasi-static configuration initially (so the Coriolis force terms are 0), and therefore it is only necessary to transform the vertices of the feasible activation set or the feasible tendon tension set to vertices in the angular acceleration space to find the feasible acceleration set. Once the set of feasible joint accelerations has been found, then an endpoint feasible acceleration set can also be constructed (if the manipulator is originally in a quasi-static state) since the endpoint accelerations provided by each joint angular accelerations will add linearly if the Coriolis acceleration term is 0.

Chapter 4

A Novel Synthesis of Computational Approaches Enables Optimization of Task-Independent Grasp Quality of Tendon-Driven Hands

4.1 Abstract

We propose a complete methodology to find the full set of feasible grasp wrenches and the corresponding wrench-direction-independent grasp quality for a tendon-driven hand with arbitrary design parameters. Monte Carlo simulations on two representative designs combined with multiple linear regression identified the parameters with the greatest potential to increase this grasp metric. This synthesis of computational approaches now enables the systematic design, evaluation and optimization of tendon-driven hands.

4.2 Introduction

Tendon-driven hands have been designed for the purposes of grasping and manipulation (Jacobsen et al. 1986, Salisbury & Craig 1982, Shadow Robot Company n.d., Grebenstein

et al. n.d., Ambrose et al. 2000, Jau 1995). While their shortcomings can include friction and tendon compliance (Chang et al. 2005), in certain applications (such as dexterous hands) they have distinct advantages over torque-driven systems including light weight, low backlash, small size, high speed, and remote actuation (Pons et al. 1999, Tsai 1995). They can also offer significant *design flexibility* in setting moment arms and maximal tendon tensions (Pons et al. 1999), which allows optimization of system output capabilities for a particular task while minimizing size and weight.

Several studies have addressed the problem of designing the topology, tendon routing, or link design of tendon-driven manipulators (or fingers) (Lee & Tsai 1991, Chen et al. 1999, Ou & Tsai 1996, Ou & Tsai 1993, Sheu et al. 2009, Salisbury & Craig 1982, Firmani et al. 2008, Tsai 1995, Tsai & Lee 1988). According to (Firmani et al. 2008), for example, “The knowledge of maximum twist and wrench capabilities is an important tool for achieving the optimum design of manipulators”. Optimization of kinematic hand parameters, such as finger placements, link lengths, and joint limits is addressed in (Salisbury & Craig 1982), but we still lack comprehensive methodologies to do large-scale optimization in these high-dimensional parameter spaces. In addition, special attention has been given to the design of manipulators with *isotropic* transmission characteristics (i.e., ability to transmit forces equally in all directions at the end effector) (Lee & Tsai 1991, Chen et al. 1999, Ou & Tsai 1996, Ou & Tsai 1993, Sheu et al. 2009, Salisbury & Craig 1982, Ou & Tsai 1996). However, it may be advantageous to design a finger with *non-isotropic* characteristics (Tsai 1995), as in the human hand (Valero-Cuevas 2005). In

addition, prior work on isotropic transmission does not consider limits on tendon tensions, which is critical when designing small, dexterous hands.

While there has been progress in designing and controlling tendon-driven robotic hands, a complete methodology for the evaluation and refinement of alternative topologies based on general-purpose grasp quality (i.e., wrench-direction-independent) has not yet been synthesized or implemented. Our novel synthesis of computational approaches now allows us to integrate and expand prior work to eliminate the following shortcomings of using previous techniques in isolation for optimization of wrench-direction-independent grasp quality of tendon-driven hands. The previously-isolated computational approaches and the integration we have accomplished are illustrated graphically in Figure 4.1.

1. Optimization intractability
2. Not considering tendon-driven architecture
3. Inability to calculate wrench-direction-independent grasp quality

The first shortcoming has been previously circumvented by using an approximation of the full grasp wrench set itself using mathematically convenient operations (Miller & Allen 1999, Miller & Allen 2004). If desired, our method can make computations more efficient by a different method: mesh simplification of the full grasp wrench set. This allows more accurate grasp quality calculations than prior approximations. The second shortcoming has not been addressed in several studies that only consider independent and identical contact points for grasp planning or analysis (Markcnscott & Yapadimitriou

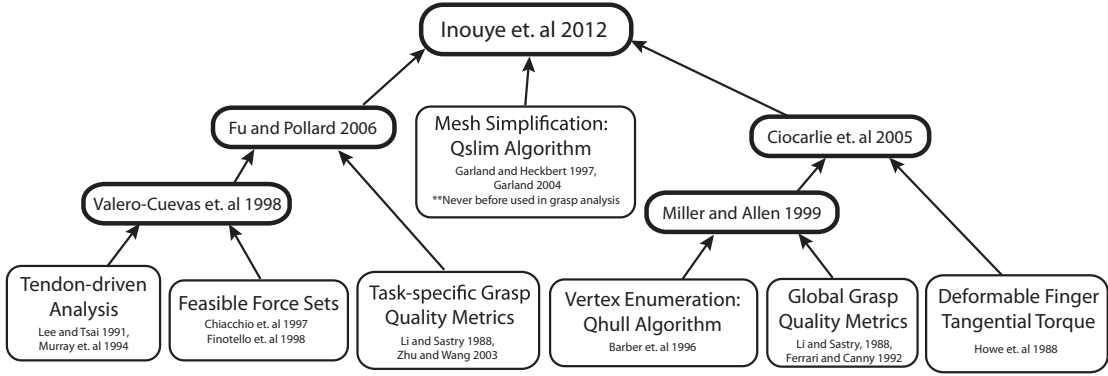


Figure 4.1: Illustration of integration of techniques that were previously isolated.

1987, Kirkpatrick, Mishra & Yap 1992, Ferrari & Canny 1992, Miller & Allen 1999, Miller & Allen 2004, Lin, Burdick & Rimon 2000, Mishra 1995). We have incorporated complete characterization of the force production capabilities of arbitrary tendon-driven hands. The third shortcoming was encountered in (Fu & Pollard 2006). They used an efficient linear programming approach to calculate a grasp quality metric for tendon-driven hands based on a very specific, pre-defined task wrench space, in which a finite number of required wrench magnitudes and directions was specified. They note that their methodology does not generalize to the full set of feasible grasp wrenches. Our integrated method does generalize to the full set of feasible grasp wrenches and allows efficient calculation of wrench-direction-independent grasp quality for tendon-driven hands.

Many other studies have addressed multi-fingered grasp (Murray et al. 1994, Surez Feijo et al. 2006, Dai & Kerr 1996, Ghafoor, Dai & Duffy 2004, Dai & Kerr 2000, Dai & Kerr 2002). Several other grasp quality metrics can be computed based on other criteria, but their application to the design of tendon-driven mechanisms is extremely limited (Surez Feijo et al. 2006). Compliances are included in grasp analysis for statically

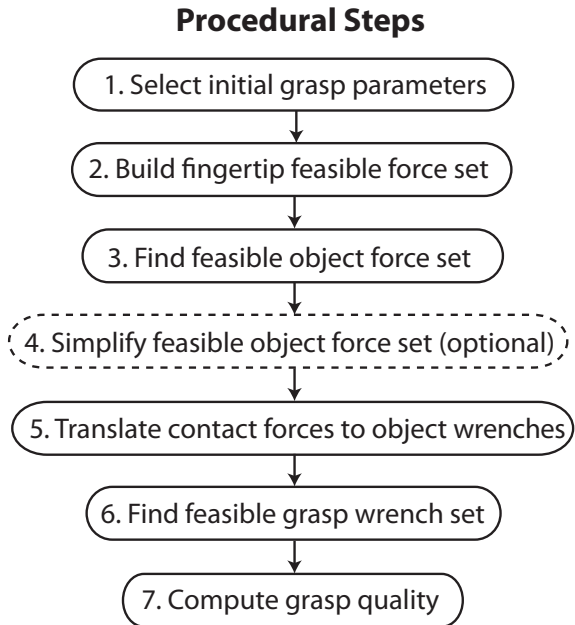


Figure 4.2: Flowchart of steps for finding feasible grasp wrench set and computing grasp quality.

indeterminate grasps in (Dai & Kerr 1996) and for grasp stiffness analysis in (Ghafoor et al. 2004, Dai & Kerr 2000). We calculate the boundaries of the grasp wrench set, where the forces are deterministic. A software environment for grasp synthesis is presented in (Dai & Kerr 2002), but it does not consider tendon-driven architecture.

We demonstrate this novel synthesis of techniques and compare grasp quality among two tendon-driven finger topologies, two grasp configurations, and thousands of parameter combinations. We then use Monte Carlo simulations to demonstrate how this computationally efficient method can be used to optimize grasp quality metrics by tuning specific design parameters.

4.3 Procedure

4.3.1 Finding the set of feasible grasp wrenches and computing grasp quality

Assessing the quality of a specific grasp with a specific hand/manipulator topology requires computing the feasible grasp wrench set and its associated grasp quality. A flowchart is in Figure 4.2.

4.3.1.1 Select initial grasp parameters

The calculation of grasp quality involves a few preliminary parameters to be specified, based on the finger geometry, number of fingers, and placement of grasping points. Grasp qualities will differ when these parameters are altered (although not substantially if they are not greatly altered, in general). So the finger geometry (i.e., D-H parameters of the finger), finger placements, finger postures, and object size and shape must all be specified before the rest of the steps of the procedure are carried out. Finger geometry is used to find the analytical manipulator Jacobian (see the appendix in Section 4.6 for further details) and the finger postures are determined from the finger geometry and choice of finger placements (which is based on object size and shape) on the object.

4.3.1.2 Build fingertip feasible force set

The next step is to build the set of 3-D forces that each finger can produce while maintaining a static posture. This set has been called the feasible force set (Valero-Cuevas 2005, Valero-Cuevas et al. 1998), or force manipulability set in the *strong sense*

(i.e., zero endpoint torque) using the language of (Finotello et al. 1998, Yoshikawa 2002)

¹. The user must specify the finger input parameters of topology (i.e., tendon routing), maximal tendon tensions, moment arm values, finger posture, and link lengths. Then the feasible force set can be calculated using the method described in detail in the appendix in Section 4.6. A visual example of a feasible force set is in Figure 4.3.

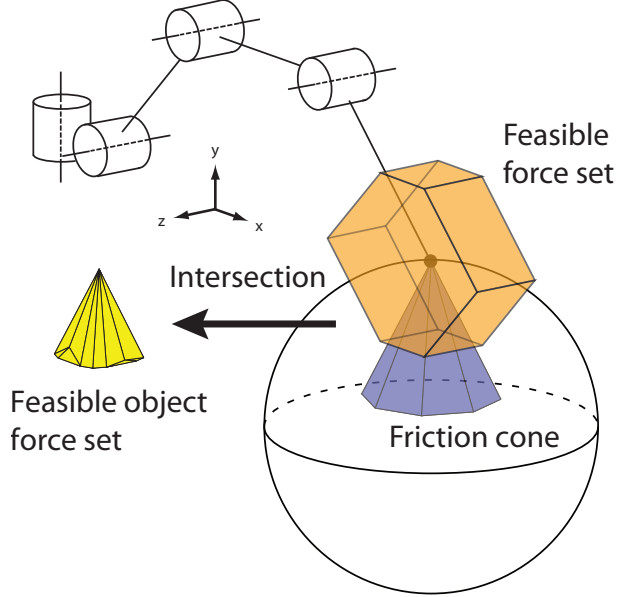


Figure 4.3: An example of a fingertip feasible force set and its intersection with a friction cone to produce a feasible object force set.

4.3.1.3 Find feasible object force set

The fingertip feasible force set does not represent the actual forces that can be applied to the surface of an object by the finger because fingertips can generally only push against surfaces. To find these feasible object forces, we must find the portion of the feasible

¹The force manipulability set in the weak sense is the set of all Cartesian forces that can be exerted by a manipulator with no constraints on endpoint torque. The strong sense force manipulability set is a subset of weak sense set with the added constraint of zero endpoint torque.

force set that also lies inside a Coulomb friction cone. We approximate this cone by using the convex hull of 8 vectors around the perimeter of the base of the cone, plus the origin, as in (Miller & Allen 2004, Murray et al. 1994). We intersect this cone with the feasible force set to find the convex hull of feasible forces that may be applied to the object. We call this set the feasible object force set, and an example is in Figure 4.3.

The inputs required for this step are the static coefficient of friction and the angle of finger contact (which is determined by object shape and finger placement). We use the Qhull vertex enumeration algorithm to complete the intersection of these convex sets.

4.3.1.4 Simplify feasible object force set

Due to the complexity and high number of vertices that may define the feasible object force set for each contact point, we may wish to simplify the set to make the analysis more computationally efficient². The analysis presented in this paper can still be completed without this step, but for thousands or millions of calculations, this step can be very beneficial with minimal loss in accuracy. To this end, we use edge collapse operations to perform 3-D mesh simplification, see Figure 4.4a. Due to the nature of tendon-driven feasible force sets, there may be many vertices that are very near each other. The edge collapse operations, in effect, combine these very close points into a few points or one point, as can be seen in Figure 4.4. This procedure was developed in computer graphics to reduce the processing and display time for 3-D objects (Garland & Heckbert 1997).

²The number of vertices of the grasp wrench set is on the order of m^n , where n is the number of feasible object force set vertices and m is the number of fingers (Miller & Allen 2004). So the computation time can become intractable for high numbers of vertices.

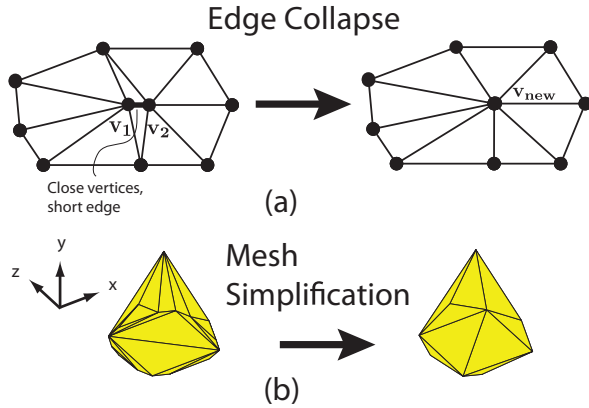


Figure 4.4: (a) An example of an edge collapse operation. The vertices v_1 and v_2 are collapsed into a new vertex v_{new} . (b) Example of using edge collapse operations to simplify the feasible object force set from 19 vertices down to 10 vertices. Note: this view is of the underside of the feasible object force set shown in Figure 4.3.

While some of the finer details of the feasible object force set are eliminated after this process, this algorithm accomplishes the simplification in a theoretically optimal manner (when considering the minimization of quadric error). Because of this, the algorithm automatically selects close vertices for edge collapse operations. Figure 4.4b shows a feasible object force set before and after simplification. We find it reduces computation time considerably with minimal effect on the results (see Results).

When the routing of the tendons is complex, such as in the human hand or in robotic hands with complex interconnections among tendons such as in the ACT Hand (Deshpande, Balasubramanian, Lin, Dallon & Matsuoka 2008), the mesh simplification will improve performance even more drastically than with simple routings. For example, simplification of the human finger feasible object force sets in (Inouye, Kutch & Valero-Cuevas 2011*b*) from approximately 60 down to 12 vertices reduced computation time from 50 s to 1.37 s, a 97% reduction!

The single parameter input for this step is the number of desired vertices for the simplified feasible object force set. Qslim is the program used to implement the edge collapse operations for mesh simplification (Garland 2004).

4.3.1.5 Translate contact forces to object wrenches

The combined forces of the fingertips produce a resultant wrench on the object. An object wrench vector, $\mathbf{w}_{i,j}$, produced statically by a point-contact force with friction, $\mathbf{f}_{i,j}$, at fingertip location i , is given by the following equation (Miller & Allen 1999):

$$\mathbf{w}_{i,j} = \begin{bmatrix} \mathbf{f}_{i,j} \\ \lambda(\mathbf{d}_i \times \mathbf{f}_{i,j}) \end{bmatrix} \quad (4.1)$$

where λ is the scaling factor that converts units of torque to comparable units of force, \mathbf{d}_i is the vector from the torque origin to the i th contact point, $i = 1, \dots, n$, where n is the number of fingertip contact locations, and $j = 1, \dots, m_i$, where m_i refers to the number of points defining the convex hull of the feasible object force set at fingertip location i . Each m_i may be unique, in contrast to analyses that treat all contact points equally and for which all m_i are equal. A reasonable choice for λ is $1/r$, where r is the distance from the torque origin to the furthest point on the object from that origin. As noted in (Miller & Allen 2004), this choice of λ guarantees that the feasible object wrench, and hence grasp quality metrics, are independent of object scale.

We use a soft finger model for two-finger grasp so that the grasp can produce force closure by withstanding tangential torque (Howe, Kao & Cutkosky 1988). The finger model assumes a certain contact area for the calculation of a rotational coefficient of

friction, but the contact is still considered to be a point contact that can withstand tangential torque, as described in (Murray et al. 1994). Past work has shown that an approximately elliptical friction limit suffices to encloses all combinations of tangential torque and shear force that the fingertip can withstand without slipping or rotating. However, a linear approximation of the friction limit surface is a valid conservative way to model a soft finger (Howe et al. 1988), which we use to make calculations more efficient: all we need to do is add and subtract the tangential torque limit to the appropriate object wrench torque component for each vertex of the feasible object force set. This process is similar to that used in (Ciocarlie, Miller & Allen 2005), but they do not consider any feasible force set (only a simple friction cone). We assume that the fingertip can resist any combination of tangential torque and tangential force for a constant normal force underneath the boundary of the linear approximation.

The inputs to this step are the finger placements (for an arbitrary grasp), and coefficient of rotational friction (which can be specified directly or calculated from the soft-finger contact radius) if the grasp is with two fingers, and linearization of the tangential torque capabilities is utilized for two-finger grasp.

4.3.1.6 Find feasible grasp wrench set

After computing all the feasible object wrenches that can be applied by each finger, these wrench vectors in 6-D are combined to form the set of all wrenches in 6-D space that can be applied to the object which the grasp can resist. This set is a convex polytope found by taking the convex hull of the Minkowski sum of the sets of feasible object wrench vectors,

where each set corresponds to a fingertip contact location. This operation is given by the following equation (Ferrari & Canny 1992):

$$FGWS = ConvexHull\left(\bigoplus_{i=1}^n \{\mathbf{w}_{i,1}, \dots, \mathbf{w}_{i,m_i}\}\right) \quad (4.2)$$

where $FGWS$ is the feasible grasp wrench set, \bigoplus is the Minkowski sum operator, n is the number of contact points, and $\{\mathbf{w}_{i,1}, \dots, \mathbf{w}_{i,m_i}\}$ denotes the m_i wrench vectors defining the feasible forces at the i th contact point. It should be noted that often the union and not the Minkowski sum is used in grasp quality calculations to greatly reduce computation time (Miller & Allen 1999, Miller & Allen 2004)³.

4.3.1.7 Compute grasp quality

Once we have calculated the feasible object wrench set, we can compute a grasp quality based on that set. The user can specify their own grasp quality metric of choice. We chose as an example the wrench-direction-independent grasp quality metric known as the radius of the largest ball. It was originally proposed in (Ferrari & Canny 1992). Determination of this grasp quality metric involves calculating the minimum offset (from the origin) of the halfspaces that define the convex hull of feasible grasp wrenches. The minimum of these offsets is equal to the radius of the largest ball, centered at the origin, that the hull can contain. The metric, in effect, is equal to the maximal magnitude of a wrench that can be applied to the object in all directions in wrench space without it losing

³The union limits the sum of finger forces (i.e., if one finger is exerts more force at a given time, then the other cannot produce as much force), while the Minkowski sum limits each finger force (i.e., the feasible object force sets are independent). While the union is computationally easier and still can provide important information about a grasp, for this study we concentrated on the more realistic Minkowski sum. For more discussion see (Miller & Allen 1999).

force closure (i.e., causing the grasp to fail). A wrench vector whose magnitude is less than the grasp quality can be applied to the object *in any direction in 6-D wrench space* without losing force closure. These calculations have been completed for independent and identical contact points in (Miller & Allen 1999).

We use the Qhull vertex enumeration algorithm for the calculation of grasp quality and it can also easily be implemented for 2-D or 3-D visualizations of the feasible object wrench set (Miller & Allen 2004).

4.3.2 Computing grasp quality metrics for specific manipulator designs

Here we describe the specifications of the designs we analyzed and the parameters that we used in the computations and Monte Carlo simulations presented in the results section.

4.3.2.1 Finger topology

We performed this analysis on the two different finger topologies in Figure 4.5a and 4.5b. Both of them had 4 kinematic DOFs: one universal joint at the base of the finger and 2 parallel hinge joints distally. For the purposes of kinematic clarity, the finger ad-abduction (i.e., side-to-side) axis was considered to be immediately proximal to the perpendicular axis of the first flexor-extensor joint, as demonstrated in Figure 4.5a. The first finger topology had a “2N” tendon arrangement, in which there are 2 opposing (or antagonistic) tendons for each degree of freedom, Figure 4.5a. This topology is similar to that in the Utah/MIT, DLR, and Shadow Hands (Jacobsen et al. 1986, Shadow Robot Company n.d., Grebenstein et al. n.d.)⁴. The second finger topology had an “N+1”

⁴These hands are not all fully actuated, and some have coupled joints. However, they are 2N designs in the sense that they use 2 antagonistic, symmetrically routed tendons to actuate each independent joint.

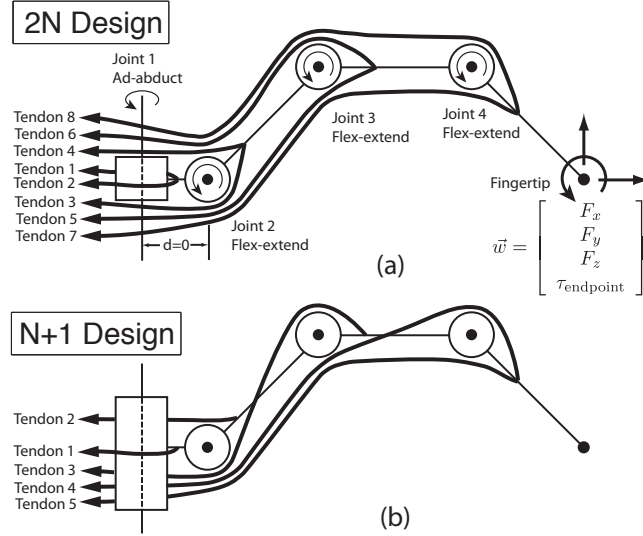


Figure 4.5: Grasp configurations analyzed. (a) 4-DOF robotic finger, 2N tendon arrangement, with endpoint wrench description. (b) 4-DOF robotic finger, N+1 tendon arrangement.

tendon arrangement, which has one more tendon than degree of freedom, and it is the minimum number of tendons that can be used to fully control the finger (Lee & Tsai 1991)⁵. N+1 topologies are analyzed for isotropic transmission in (Ou & Tsai 1993, Chen et al. 1999) and analyzed for implementation in the Stanford-JPL hand (Salisbury & Craig 1982). The particular N+1 topology we analyzed (there are many possible N+1 topologies) is in Figure 4.5b.

For the baseline results, each of the three links of each finger had length of 2 cm. The posture of the finger was 0° ad-abduction, 45° extension on joint 2, and 45° flexion on both joints 3 and 4. This is the posture in Figure 4.5. The link lengths and the posture

It should also be noted that there are many possible 2N, symmetric, antagonistic designs, and that we simply chose this particular one for demonstration purposes.

⁵ Any more than N+1 tendons is considered tendon redundancy, and typically not more than 2N tendons are used in dexterous robotic fingers. Manipulators or fingers with more than 2N tendons can have very interesting redundancy properties, as in (Kobayashi, Hyodo & Ogane 1998), and can be analyzed using our method as well.

were used to calculate the Jacobian matrix for these fingers. All of the moment arms for both topologies and all joints were given a value of 5 mm, which, along with the tendon configuration, defined the R matrix. This matrix was either 4×8 (2N design) or 4×5 (N+1 design). The sum of the maximal tendon tensions was 1000 N and divided up evenly among the tendons. This defined the F_0 matrix, which was a diagonal 8×8 (2N topology) or 5×5 (N+1 topology) matrix. The J , R , and F_0 matrices were then used to calculate the feasible force sets of the fingers.

The sum of maximal tendon tensions being equal is an important constraint due to the size, weight, and motor torque (and therefore tendon tension) limitations inherent in dexterous hands. For example, the torque capacity of motors is roughly proportional to motor weight, and minimization of weight was an important consideration in the design of the DLR Hand II(Butterfa, Grebenstein, Liu & Hirzinger 2001). In addition, the maximal force production capabilities of McKibben-style muscles are roughly proportional to cross-sectional area (Pollard & Gilbert 2002). Since the actuators typically will be located in the forearm, then the total cross-sectional area will be limited to the forearm cross-sectional area. In this first presentation of the methodology, we do not consider alternative constraints on the actuation system (e.g., electrical current capacity, tendon velocities, etc.).

4.3.2.2 Grasp configuration

Both two- and three-finger grasps were analyzed for each of the two topologies, and the finger placements are in Figure 4.6. The two-finger grasp simply had both fingertips on opposite sides of a sphere of radius 6 cm. The two-finger configuration is in Figure 4.6a

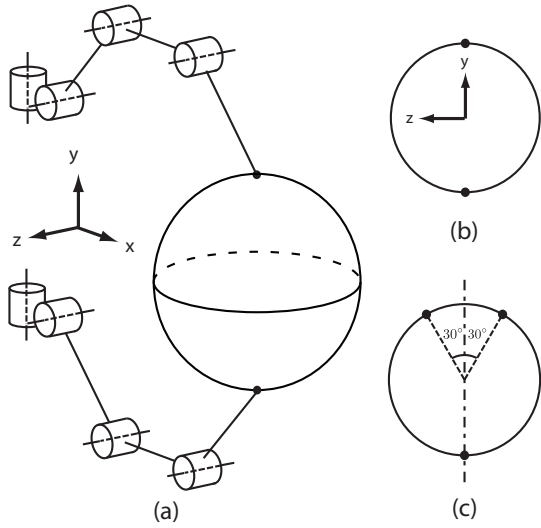


Figure 4.6: Grasp configurations analyzed. (a) Isometric view of 2-finger grasp. (b) Front view of 2-finger grasp. (c) Side view of 3-finger grasp.

and 4.6b. The three-finger grasp had one fingertip at the bottom and the other two fingers were placed so that they were 30° from a vertical line going through the bottom finger, Figure 4.6c.

4.3.2.3 Calculating grasp quality

For the two-finger grasps, the linear coefficient of friction was set to 0.5. The rotational coefficient of friction was set to 2.5 times the linear coefficient of friction (in mm). This corresponds to a very-soft finger contact radius of 5 mm (Howe et al. 1988).

The grasp analysis was performed in MATLAB[®] (R2010a, The MathWorks) on an Apple desktop computer (2 x 2.66 GHz Dual-Core Intel[®] XeonTM) running OS X Version 10.6.4. The programs Qhull (floating-point arithmetic vertex enumeration), LRS (exact arithmetic vertex enumeration), and Qslim (edge collapse operations) were used

as compiled binaries for Mac OS X and were called through the MATLAB ‘system’ command (Avis 2000, Barber, Dobkin & Huhdanpaa 1996, Garland 2004). The rest of the computations were completed using custom MATLAB code.

4.3.2.4 Monte Carlo simulations

To demonstrate the computational utility of our method, the baseline parameters of moment arms, maximal tendon tensions, and link lengths were perturbed simultaneously and independently (Valero-Cuevas et al. 2009). To do so, we drew from uniform distributions with the lower bound being 20% below each particular baseline parameter value and the upper bound being 20% above the baseline parameter value, for a total range of 40% variation, Figure 4.7. For each finger there are 14 non-zero moment arm values, 3 link lengths and 8 (for 2N topology) or 5 (for N+1 topology) maximal tendon tensions, for a total of 25 (2N topology) or 22 (N+1 topology) total independent parameters that were perturbed for each iteration. We performed 1000 iterations (each having their own set of parameters) for each of the 2 topologies and each of the 2 grasp configurations. This number of iterations was found to be sufficient for convergence, as in (Santos & Valero-Cuevas 2006) (discussed further in Results).

4.3.2.5 Regression analysis

To demonstrate the utility of these Monte Carlo simulations for design and analysis purposes, the grasp quality was regressed on the independent parameters that were varied during the simulations. Stepwise regression on only the linear terms was performed (i.e., no interaction or higher-order terms were used) using an initial model with no

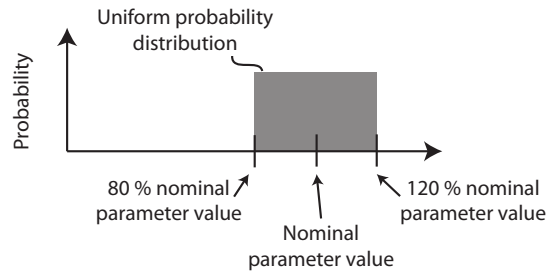


Figure 4.7: Uniform sampling distribution used for each independent parameter value perturbation in Monte Carlo simulations.

predictors, and predictors were added to the model with a cutoff p-value of 0.05. This was performed in MATLAB. Prior to the regression analysis, the independent parameters were normalized so that the baseline value was equal to 1. In addition, the dependent parameters were normalized so that their average was also 1. Therefore, the regression coefficients represent the expected percentage increase in the grasp quality with a 1% increase in the independent parameter.

4.4 Results

4.4.1 Baseline results

Table 4.1 shows the grasp quality results for the two “baseline” topologies (i.e., those with the nominal values for each design parameter) for the two- and three-finger grasps. Despite the fact that both topologies have the same sum of maximal tendon tensions (i.e., system input), the 2N topology is clearly superior to the N+1 topology (using the nominal parameters) in grasp quality, and hence can resist wrenches of higher magnitude in all directions.

	2N Topology (N)	N+1 Design (N)
2-finger	2.59	1.71
3-finger	8.66	5.60

Table 4.1: Baseline grasp quality results. Coefficient of static friction $\mu_s = 0.5$. Units of grasp quality are in Newtons.

In addition, as expected, the grasp quality is higher for the three-finger grasp than the two-finger grasp for both topologies. These baseline results were verified using the exact arithmetic vertex enumeration code LRS (Avis 2000), where the evaluation time was around 100 times greater than the Quickhull algorithm (Barber et al. 1996).

4.4.2 Monte Carlo simulations

Given that computation times for the baseline cases were fairly long (about 30 s), especially for the 3-finger grasp, we simplified the feasible object force sets to make Monte Carlo simulations feasible. We found that simplifying the feasible object force set down to 12 vertices reduced computation time by a minimum of 46% (reduction from 23.7 seconds to 12.7 seconds for N+1, 3-finger case) and a maximum of 77% (reduction from 39.9 seconds to 9.10 seconds for 2N, 3-finger case) out of the 4 baseline cases, and resulted in less than 2% error in grasp quality.

The 1000 Monte Carlo simulations reached “convergence” in the sense that the running mean and coefficient of variation varied less than 2% in the last 20% of iterations, similar to the criteria used in (Santos & Valero-Cuevas 2006). Average evaluation time for each of the 4 configurations is shown in Table 4.2. Figure 4.8 shows histograms of the Monte Carlo grasp quality results for 2-finger grasp. The different finger topologies for this grasp certainly have different mean characteristic lengths ($p < 0.00001$) when the

	2N Topology (s)	N+1 Topology (s)
2-finger	1.46 (0.30)	1.29 (0.42)
3-finger	9.79 (1.98)	9.77 (2.66)

Table 4.2: Average evaluation times (standard deviations) during Monte Carlo simulations, in seconds.

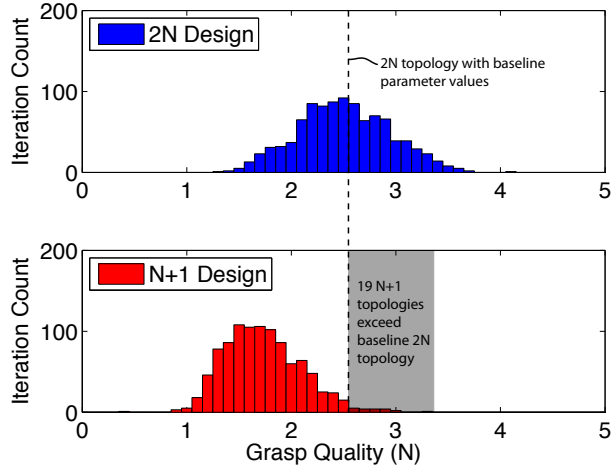


Figure 4.8: Histogram of grasp quality values from Monte Carlo simulations for two-finger grasp, 2N and N+1 designs, with Gaussian curves overlaid. The N+1 topologies exceeding the baseline 2N topology are shaded gray.

parameter values are perturbed by 20%. However, for the N+1 topology we find that 19 parameter combinations exceed the grasp quality of the 2N topology with baseline parameter values.

4.4.3 Regression analysis

The significant regression coefficients at a cutoff p-value of 0.05 for grasp quality for the N+1, 2-finger case are shown in Table 4.3, grouped by parameter type. The coefficient of determination R^2 is 0.930, signifying a good fit for the linear model. Link lengths, maximal tendon tensions, and moment arms should be adjusted according to Table 4.3 to produce the N+1 topologies that exceed the baseline 2N topology. We find that

decreasing the link lengths understandably increases grasp quality (because it improves the moment-arm:lever-arm ratio of the tendons), and decreasing the length of link 2 has the greatest predicted effect on grasp quality. As would be expected, the one significant regression coefficient for maximal tendon tension is positive (i.e., grasp quality can never be worsened by increasing one of the maximal tensions). However, not all maximal tendon tensions improve this grasp quality metric if increased. While all maximal tendon tensions change the size and shape of the feasible grasp wrench set, some have insignificant effects on grasp quality because increasing them increases the size of the feasible grasp wrench set in directions that do not increase the weakest wrench capability of the grasp. That is, they do not push out the boundary of the feasible grasp wrench set that is closest to the origin. However, the maximal tension of tendon 1 does affect that boundary and increasing it enhances this metric of grasp quality. Therefore, one of the “weak links” in this topology is the maximal tension of tendon 1, which if increased leads to better performance. Moment arms exhibit both positive and negative regression coefficients in their effect on grasp quality, as they affect the direction and magnitude of the wrench basis vectors (Valero-Cuevas 2005). The best N+1 topology from the Monte Carlo simulations (grasp quality of 3.31–94% greater than the N+1 baseline) has maximal tension of tendon 1 15% higher than the baseline and the moment arm of tendon 1 across the ad-abduction axis is 16% above baseline. These parameters have the greatest effect on grasp quality, as can be seen in Table 4.3.

Table 4.4 shows the effects of adjusting the significant moment arm parameters individually by 10% in the direction that increases grasp quality while keeping all the other

Parameter		Expected Percentage Increase in Quality for a 1% Increase in Parameter Value	95% Confidence Interval
Link length	Link 2	-0.436	(-0.466, -0.406)
	Link 1	-0.333	(-0.363, -0.302)
	Link 3	-0.290	(-0.320, -0.260)
Max tension	Tendon 1	0.995	(0.265, 1.03)
	Tendon 2	—	—
	Tendon 3	—	—
	Tendon 4	—	—
	Tendon 5	—	—
Moment arm	1,1	1.01	(0.975, 1.04)
	1,5	-0.593	(-0.623, -0.564)
	2,5	0.553	(0.522, 0.583)
	2,4	0.272	(0.243, 0.302)
	1,4	-0.259	(-0.289, -0.228)
	2,3	0.159	(0.128, 0.190)
	1,3	-0.143	(-0.174, -0.112)
	1,2	—	—
	2,2	—	—
	3,3	—	—
	3,4	—	—
	3,5	—	—
	4,4	—	—
	4,5	—	—

Table 4.3: Significant normalized regression coefficients for grasp quality with 95% confidence intervals on N+1 topology, 2-finger grasp. ‘—’ denotes not significant at the cutoff p-value of 0.05. Moment arms expressed as (Joint number,tendon number). $R^2 = 0.930$.

	Grasp Quality	Normalized Coefficient	Expected Increase	Actual Increase
Baseline	1.709	—	—	—
Moment arm 1,1 (+10%)	1.880	1.01	10.1%	10.0%
Moment arm 1,5 (-10%)	1.812	-0.593	5.93%	6.03%
Moment arm 2,5 (+10%)	1.809	0.553	5.53%	5.88%
Moment arm 2,4 (+10%)	1.756	0.272	2.72%	2.79%
Moment arm 1,4 (-10%)	1.758	-0.259	2.59%	2.86%
Moment arm 2,3 (+10%)	1.733	0.159	1.59%	1.40%
Moment arm 1,3 (-10%)	1.734	-0.143	1.43%	1.47%

Table 4.4: Expected (from linear regression on Monte Carlo iterations) and actual (from computational method implementation) effects of moment arm adjustments by 10% on grasp quality of N+1 design, 2-finger grasp. Moment arms expressed as (Joint number, tendon number).

parameters at baseline levels. We see that the predictions from even a simple linear regression are validated.

4.5 Discussion

In this work, we have demonstrated a novel synthesis of computational approaches for evaluating the grasp quality of arbitrary tendon-driven hand designs. Our formulation is efficient enough to consider all finger design parameters (number and routing of tendons, tension limits, and posture) and grasp (number and configuration of fingers, friction characteristics, and object shape and size) and computes the full feasible grasp wrench set, from which a variety of grasp quality metrics can be obtained. In this first demonstration of our methodology, we compared the wrench-direction-independent grasp quality for two topologies, two grasp configurations, and thousands of parameter combinations when grasping a sphere, and we present the steps for extending this methodology to completely arbitrary hand designs, objects, and finger placements.

Our Monte Carlo exploration of the design space demonstrates the computational efficiency and utility of our method and shows that, as expected, the 2N topology is generally superior to the N+1 topology in grasp quality and hence can resist wrenches of higher magnitude in all directions. This is because this 2N topology can exert a wider range of forces on the object than the N+1 topology, resulting in higher grasp quality. Importantly, however, our parameter exploration found certain designs (within the allowed $\pm 20\%$ variability) for which the N+1 topology can outperform the nominal 2N topology. If a designer favors the N+1 topology due to actuator/space/weight constraints, there are N+1 topologies that can meet or exceed the performance of a nominal 2N topology (which may have less design flexibility because of more tendons). These results would apply to most objects of similar size since the main difference would be a small change in finger contact angle.

In addition, the extensive exploration of the high dimensional parameter spaces (i.e., 22 or 25 dimensions) allows us to identify some critical design parameters for grasp quality (i.e., with a high R^2 value of 0.930, noted in Table 4.3). Regressions for our N+1, 2-finger case (Table 4.3), for example, it is clear that one tendon and one moment arm are, from among 22 parameters, the most critical individual parameters in the design; altering them in isolation has the greatest effect on characteristic length. Exploring second and third order parameter sensitivities is likely intractable with this or most other techniques because of the geometric growth of iterations needed. Second order terms in a regression would bring the number of regressed independent variables to over 400, and third order terms would raise that number to over 8000.

Nevertheless, our approach demonstrates sufficient computational efficiency to enable, for the first time, exploring large-dimensional design spaces. Optional adjustments in mesh simplification procedures or friction cone approximations can and do bring improvements to speed with minimal loss in accuracy but they are not central to our methodology. Additionally, other techniques, such as hull approximation or Voronoi filtering, could be used to simplify the grasp wrench set. Importantly, we tested and found that our computationally streamlined floating-point computations produced results equivalent to the 100 times slower exact arithmetic calculations.

This approach is innovative because it now enables optimizing the design of dexterous tendon-driven hands by testing hundreds or thousands of alternative hand topologies quickly. For anthropomorphic hands or prosthetic hands, link geometry is relatively fixed, but all tendon routing and moment arm values can be varied. For general-purpose manipulators, everything from number and arrangement of fingers, to DOFs and link lengths of each finger, to number, routing and strength of tendons may be varied and evaluated. Any number of optimization algorithms, including gradient-descent, genetic, or random search algorithms, could be employed with this methodology to explore the design space and optimize the topology of dexterous hands. The efficacy and efficiency of random search algorithms are being explored in current research.

This method can also be used to determine the optimal grasping points of a particular object for a particular set of tendon-driven hand design parameters. If this is desired, then many finger placements can be tested to determine the one with the optimal grasp quality.

We calculate the grasp quality for precision grasp (i.e., grasp by the fingertips) in this study. This is the grasp that is necessary to manipulate an object. Power grasp capabilities (where the fingers are wrapped completely around an object) could be calculated with a modified version of this algorithm. However, in general, power grasp quality and precision grasp quality will tend to be highly correlated due to the fact that a high flexion force in the fingers is desirable for both grasps.

The shaping of the feasible output of a robotic system via variation of mechanical design parameters has been of interest for several decades (Lee & Tsai 1991, Chen et al. 1999, Ou & Tsai 1996, Ou & Tsai 1993, Sheu et al. 2009, Salisbury & Craig 1982). Our novel synthesis of computational approaches now enables its pursuit for large dimensional, tendon-driven systems. Grasp quality, manipulability metrics, and hand complexity metrics such as number of fingers, number of joints per finger, and number of tendons could also be integrated into a multi-objective optimization algorithm.

Many other grasp quality metrics are easily computed using the basic procedure we have described. One example is the volume of the feasible wrench set (Miller & Allen 1999). Qhull can be easily queried to calculate this volume at the same time it is calculating the weakest wrench metric we analyzed in this study. Another example is task-specific grasp quality metrics such as those used in (Fu & Pollard 2006, Zhu & Wang 2003, Li & Sastry 1988). Once the grasp wrench set is calculated, the straightforward linear programming technique used in (Fu & Pollard 2006) can be used to calculate this metric for polytopes or using singular value decomposition (Li & Sastry 1988) for ellipsoids.

Future work will use this methodology to design dexterous, tendon-driven hands with higher grasp capabilities than are currently available, and simpler hands with specific capabilities. Furthermore, this work on static grasp can be extended to manipulability sets or feasible acceleration sets, which quantify the velocities or accelerations with which an object can be manipulated. This methodology could also be used in grasp planning, where an optimal or near-optimal grasp found for a specific tendon-driven hand may actually be a bad grasp for another tendon-driven hand. This methodology also enables the quantitative analysis of biological hands and grasps (including human (Inouye et al. 2011*b*)), and also can help to answer questions about its anatomical structure, so we can perhaps draw inspiration from it for novel robotic designs. Lastly, this analysis can also be applied to design and optimize arbitrary tendon-driven and reconfigurable robots, such as tensegrity structures, to perform complex manipulation and locomotion tasks(Paul, Valero-Cuevas & Lipson 2006, Rieffel, Valero-Cuevas & Lipson 2009).

4.6 Appendix: Calculation of the feasible force sets of tendon-driven manipulators

Fundamental to feasible force set analysis is the calculation of the posture-dependent manipulator Jacobian, $J(\mathbf{q})$. \mathbf{q} is the vector of joint angles (i.e., finger posture). The Jacobian represents a linear mapping from angular velocities of the joints to endpoint velocity as shown in the following equation:

$$\dot{\mathbf{x}} = J(\mathbf{q})\dot{\mathbf{q}} \quad (4.3)$$

where $\dot{\mathbf{x}}$ is the endpoint velocity vector (it can include both translational and rotational components, and so can be up to 6-dimensional, see (Yoshikawa 2002) for more details), $J(\mathbf{q})$ is the manipulator Jacobian, \mathbf{q} is the vector of joint angles (i.e., finger posture), and $\dot{\mathbf{q}}$ is the vector of joint angle velocities.

If an underactuated finger is being analyzed, then the Jacobian is only constructed with columns that correspond with joint angles that can be independently actuated, and the analytical expressions for each entry of the Jacobian matrix, which would normally include all joint angles, will only include the actuated joint angles. If the last 2 joints are coupled such as in the human hand or Shadow Hand (Leijnse, Quesada & Spoor 2010, Shadow Robot Company n.d.), then the last joint angle q_4 would be a (presumably) linear function of q_3 (e.g., $q_4 = q_3/2$). The Jacobian could be reduced from 4 to 3 columns, and the analytical expressions for each entry of the Jacobian matrix could be constructed as a function of 3 joint angles by substituting in for the last joint angle (e.g., substituting $q_3/2$ in for q_4). The Jacobian would then be 3×3 (instead of 3×4) even though there are 4 joint angles. Advanced kinetostatic analysis of underactuated fingers is performed in (Birglen & Gosselin 2004), although the simple procedure just described should be sufficient for the calculation of feasible force sets for most robotic applications. Furthermore, minimally underactuated hands with, for example, one tendon for flexion and springs for extension could be analyzed in the torque domain and appropriate dimensionality reduction of the Jacobian matrix.

Once the Jacobian is calculated, using the principle of virtual work, we can find the linear mapping between endpoint wrench (i.e., generalized forces which can include force and torque components and therefore can be up to 6-dimensional, depending on the

formulation of the Jacobian used), \mathbf{w} , and joint torques, $\boldsymbol{\tau}$, as shown in the following equation:

$$\boldsymbol{\tau} = J^T \mathbf{w} \quad (4.4)$$

Since we are analyzing tendon-driven systems, we also need the moment arm matrix, R , which contains the values of the moment arms for each of the tendons across each of the joints. It is an $n \times \ell$ matrix, where n is the number of joints and ℓ is the number of tendons of the manipulator. The entries are $r_{i,j}$, which is a signed moment arm value (positive values indicate positive torque generated at a joint when tension is applied to the tendon, and v-v), i is the joint number and ranges from 1 to n , and j is the tendon number, which ranges from 1 to ℓ . The moment arm matrix can be used to transform tendon tensions, \mathbf{T} , to joint torques using the following equation:

$$\boldsymbol{\tau} = R\mathbf{T} \quad (4.5)$$

We can use an activation vector, \mathbf{a} , to represent the degree to which a tendon is activated. Each element of \mathbf{a} ranges between 0 (no activation) and 1 (full activation). Further discussion may be found in (Valero-Cuevas 2005). If we define F_0 as a diagonal matrix of maximal tendon tensions, then we get the following relation between activations and tendon tensions:

$$\mathbf{T} = F_0 \mathbf{a} \quad (4.6)$$

The first step to calculating the feasible force set is to find the feasible torque set by taking the convex hull of points generated by mapping each vertex of the feasible activation set to joint torque space by combining Equations 4.5 and 4.6:

$$\boldsymbol{\tau} = RF_0\mathbf{a} \quad (4.7)$$

The feasible 3-D force set can be found from this feasible torque set by intersecting the feasible torque set with the linear subspace spanned by the columns of J^T (Fu & Pollard 2006, Chiacchio et al. 1997). This can be accomplished with any vertex enumeration algorithm. The vertices of this reduced-dimensionality set can then be transformed to endpoint force space using the Moore-Penrose pseudoinverse so that

$$\mathbf{w} = J^{+T}\boldsymbol{\tau} \quad (4.8)$$

where J^{+T} denotes the Moore-Penrose pseudoinverse of J^T ⁶.

If the 3-D feasible force set is being calculated (as in this study), then the wrench vector in Equation 4.8 will be of length 3 and will have components of F_x , F_y , and F_z .

Acknowledgements

The authors gratefully acknowledge the useful comments by M. Kurse, B. Holt, and C. Raths.

⁶If the Jacobian is square and invertible, the inverse J^{-T} can be taken and the feasible torque set subspace intersections are unnecessary.

Chapter 5

Quantitative Prediction of Grasp Impairment in Peripheral Neuropathies of the Hand

5.1 Abstract

5.2 Introduction

Grasping is a fundamental hand function that is impaired or eliminated following peripheral neuropathies of the hand (Riordan 1969). Using a novel computational framework for calculating grasp quality of tendon-driven hands (Inouye, Kutch & Valero-Cuevas 2012), we predicted grasp quality for various degrees of simulated peripheral neuropathies: (i) carpal tunnel syndrome, (ii) low median nerve palsy, (iii) low ulnar nerve palsy, and (iv) low radial nerve palsy.

5.3 Methods

Calculation of grasp quality for tendon-driven hands involves several steps (Inouye et al. 2012). The first is determination of the fingertip forces that each tendon produces when

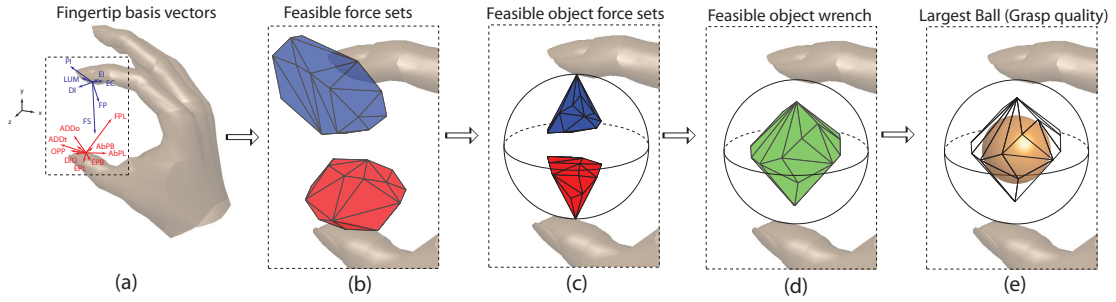


Figure 5.1: Grasp quality calculation steps. (a) Basis vectors. (b) Feasible force sets. (c) Feasible object force sets. (d) Feasible object wrench illustrated in 3-D. (e) Grasp quality metric of radius of largest ball (illustrated in 3-D; actual calculation is in 6-D).

tension is applied. We use previously-published cadaveric data from the thumb and index finger (Pearlman, Roach & Valero-Cuevas 2004, Valero-Cuevas, Towles & Hentz 2000) to determine these basis vectors (Figure 5.1a), from which the feasible force set (the set of 3-dimensional forces that the fingertip can produce) can be calculated, shown in Figure 5.1b. These sets are then intersected with friction cones, producing feasible object force sets: the sets of forces that the fingertip is able to apply to the object, shown in Figure 5.1c. From these sets, the set of all forces and torques on the object (i.e., the feasible object wrench) that the grasp can resist may be calculated, shown in Figure 5.1d.

The first grasp quality metric we used was the weakest wrench (combination of force and torque) magnitude (in Ntorque is scaled to N with the radius of the object) that could be resisted by the grasp. This is equivalent to the radius of the largest ball, centered at the origin, that the feasible object wrench set can contain, and is illustrated in Figure 5.1e in 3-D, although the actual measure is in 6-D (3 dimensions for force and 3 for torque). For example, if the grasp quality is 5, then the grasp can resist at least 5N of force or scaled torque in any direction. We call this the radius of largest ball.

Finger	Muscle	Innervation group
Index	Flexor digitorum profundus (FDP)	M
	Flexor digitorum superficialis (FDS)	M
	Extensor indicis proprius (EIP)	R
	Extensor digitorum communis (EDC)	R
	First lumbrical (LUM)	M, CTS
	First dorsal interosseous (FDI)	U
	First palmar interosseous (FPI)	U
Thumb	Abductor pollicis brevis (AbPB)	M, CTS
	Abductor pollicis longus (AbPL)	R
	Adductor pollicis oblique (ADDo)	U
	Adductor pollicis transverse (ADDt)	U
	First dorsal interosseous (DIO)	U
	Extensor pollicis brevis (EPB)	R
	Extensor pollicis longus (EPL)	R
	Flexor pollicis brevis (FPB)	M, CTS
	Flexor pollicis longus (FPL)	M
	Opponens pollicis (OPP)	M, CTS

Table 5.1: Muscles in each nerve pathology group. M: median, R: radial, U: ulnar, CTS: Carpal Tunnel Syndrome.

The second grasp quality metric we used was the radius of the 6-D ball with the same volume as the feasible object wrench, which we call the characteristic length.

Using this framework, we simulated various degrees of nerve palsies and carpal tunnel syndrome by progressively weakening muscles controlled by these innervation groups from their maximal force (Pearlman et al. 2004, Valero-Cuevas et al. 2000). We modeled carpal tunnel syndrome as low median nerve palsy that does not affect extrinsic muscles, since they are innervated proximal to the wrist (Katz & Simmons 2002). The muscles for each innervation group are shown in Table 5.1.

5.4 Results and Discussion

The impairment of grasp quality with simulated advancement of peripheral neuropathy is shown in Figure 5.2. We see that low median nerve palsy quantitatively affects both measures of grasp quality most severely. In addition, we observe that complete loss of any innervation group causes the radius of largest ball to be zero. This means that there are some directions of perturbation in 6-D wrench space that the grasp cannot resist, and therefore the grasp does not have force closure, which is considered to be a maximally deficient grasp. As expected, carpal tunnel syndrome decreases grasp quality less than full low median nerve palsy. Although low radial nerve palsy affects the extensors of the fingers, it has a comparable effect to carpal tunnel syndrome because they, counterintuitively, also contribute to grasp, as described earlier (Valero-Cuevas et al. 1998).

Acknowledgements

NSF EFRI 0836042 and NIH AR050520 and AR052345 to FVC. Thanks to Sudarshan Dayanidhi for helpful discussions

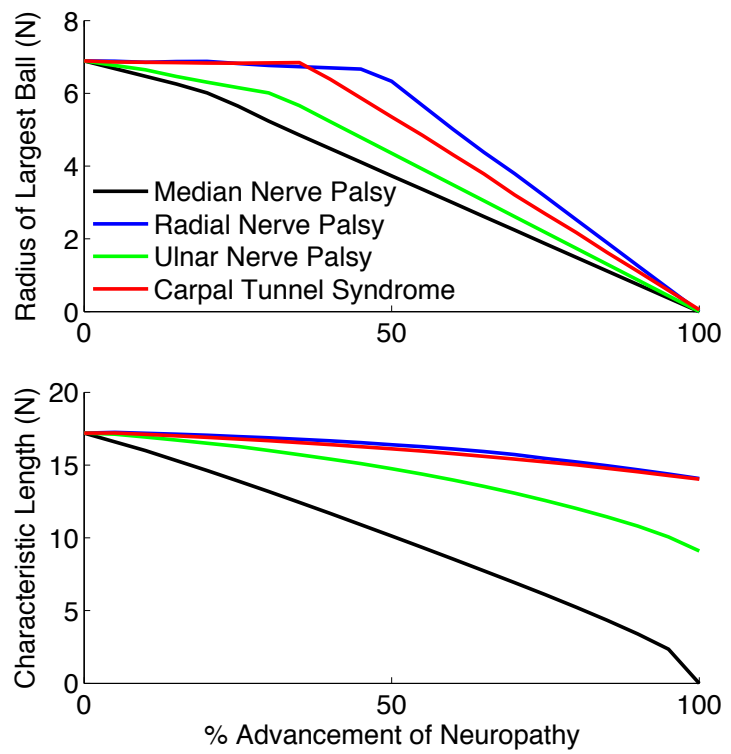


Figure 5.2: Grasp quality deterioration as a function of % advancement of neuropathy.

Chapter 6

Bettering the Human Hand: Anthropomorphic Tendon-Driven Robotic Hands can Exceed Human Grasping Capabilities

6.1 Abstract

There is great debate about how effectively the human hand is able to grasp and manipulate objects and whether it is optimized in any sense. Here we compare the grasping capabilities of the physiological human hand and thousands of tendon-driven anthropomorphic hand designs. The anthropomorphic hands are given constraints that allow for fair comparisons to the human hand (friction coefficients, maximal moment arms, and maximal tendon tensions). The layout of the anthropomorphic hand and the D-H parameters of each finger (a 4-DOF index finger and a 5-DOF thumb) are set to those of the commercially available Shadow Hand. We use a previously-developed computational technique to assess the grasp quality of each anthropomorphic hand design. We initially tested designs that had randomly-generated, admissible structure matrices along with equal moment arms and maximal tendon tensions. Next, we used an optimization

scheme that employed crossover operations (similar to those used in genetic algorithms) and greedy Markov-Chain Monte Carlo optimization. We find that none of the randomly-generated designs are able to exceed the grasp quality of a human hand and the best one has a grasp quality 45% below that of the human hand, with a mean grasp quality 78% below the human hand. However, optimization of the joint centers of rotation and the distribution of maximal tendon tensions produces hands with grasp qualities that exceed the human hand by 13-45%. In addition, one optimized design was able to outperform a naïve 2N design by 501%. This huge difference implies that grasping performance of dexterous prosthetic or anthropomorphic hands can be vastly improved by altering some of the numerous parameters. In addition, we conclude that the human hand is optimized for grasping, at least to an extent, when considering that it vastly outperforms randomly-generated designs.

6.2 Introduction

Anthropomorphic tendon-driven hands have been designed over the past few decades for the purposes of grasping and manipulation (Ambrose et al. 2000, Jacobsen et al. 1986, Jau 1995, Massa et al. 2002, Salisbury & Craig 1982). These dexterous prosthetic and robotic hands take their inspiration from the tendons present in the entirety of the human body. The most fantastic example of a tendon-driven system either in nature or in robotics is the human hand. The complexity, intricacy, and functionality of its elaborate architecture and 46 muscles have never been duplicated, even without consideration of its spectacular sensory and regeneration capabilities. It is unrivaled in its ability to grasp and manipulate

objects, while having very compact size and excellent durability when compared with robotic and prosthetic hands available today. One part of the elegance of the human hand is due to the control imparted to the muscles via the nervous system. The other part is the mechanics of the tendon and muscle arrangements. This paper focuses on the latter, in relation to grasp quality.

While bio-inspired artificial hands have been criticized for issues such as friction and tendon compliance (Chang et al. 2005), they have distinct advantages over torque-driven hands including light weight, low backlash, small size, high speed, and remote actuation (Tsai 1995). Another important advantage is that they offer significant design flexibility in setting moment arms and maximal tendon tensions (Pons et al. 1999), which allows optimization of capabilities for particular families of tasks (such as grasping).

Previous research on grasp quality for tendon-driven hands has enabled computation of a grasp quality metric based on a very specific, pre-defined task wrench space (Fu & Pollard 2006). However, they note that their methodology, which utilizes a linear programming approach, does not generalize to the full set of feasible grasp wrenches. A recent study (Inouye et al. 2012) has developed a comprehensive framework for evaluating global grasp quality metrics of tendon-driven hands. We use this methodology for computing and optimizing grasp quality in this paper.

A previous study has optimized a robotic finger to mimic the force production capabilities of the human index finger (Pollard & Gilbert 2002). This optimization was based on minimizing total maximal tendon tensions while meeting or exceeding the static forces that the human finger was able to produce. Size constraints were in place to allow for fair comparison. They also performed some optimization techniques on moment arms.

However, to the best of our knowledge, there has been no study to compare the grasp quality of the human hand with anthropomorphic hands which have the same mechanical constraints (e.g., size, muscle strength).

Here we compare the grasp quality of the human hand with that of random and optimized anthropomorphic hands with human hand constraints. We show that the human hand has much higher grasp quality than random designs, but that careful use of optimization techniques can produce designs that meet or exceed the grasp qualities of the human hand.

6.3 Procedure

6.3.1 Calculating human hand grasp quality

In order to find the grasp quality of the human hand, we combined previously-published cadaveric data (Valero-Cuevas et al. 2000, Pearlman et al. 2004) with a computational method for calculating grasp quality that was recently developed (Inouye et al. 2012). The cadaveric data are given by basis vectors in fingertip endpoint wrench space that each of the tendons produce when tension is applied. Maximal tendon tensions are also given. For the index finger, the data are given in 4 dimensions: 3 in force space and one in torque space. For the thumb, the data are given in 3 dimensions, all in force space. The force space components of the basis vectors for each finger are shown in Figure 6.1a. The feasible force set of each fingertip is built from these basis vectors and maximal tendon tensions using the approach outlined in (Inouye et al. 2012, Valero-Cuevas 2005) and is shown in Figure 6.1b. The remaining procedure of intersecting the feasible force sets

with friction cones (Figure 6.1c) and calculating the feasible grasp wrench set (Figure 6.1d) and associated global grasp metrics is described in (Inouye et al. 2012). Since the grasp quality measures of characteristic length and radius of largest ball are both linear measures and have identical units, we assign a single grasp quality metric to the human hand that simply sums the two measures. Figure 6.1e shows how computation of the feasible object wrench predicts whether a grasp can be maintained against an external force.

The linear coefficient of friction is set to 0.5, and the ratio of the linear coefficient of friction to the rotational coefficient of friction is set to 7. Both of these values are in the range of physiologically-reported friction coefficients for human fingertips (Kinoshita, Backstrom, Flanagan & Johansson 1997). The hand is assumed to grasp a ball of diameter 6cm with the thumb fingertip on the bottom and the index finger on the top, as pictured in Figure 6.1c.

6.3.2 Calculating anthropomorphic hand grasp quality

We used the kinematic layout of the Shadow Hand (a tendon-driven, commercially-available, anthropomorphic hand) (Shadow Robot Company n.d.) in order to determine finger link lengths, placements, and postures for grasp. The grasping posture of the anthropomorphic hand was selected to closely resemble that of human posture while still grasping the 6cm ball, shown in Figure 6.2.

The index finger has 4 degrees of freedom: 3 flexion-extension and one ad-abduction. The thumb has 5 degrees of freedom: 3 flexion-extension and 2 ad-abduction. The process for finding the feasible force set of the 4-DOF index finger has been studied

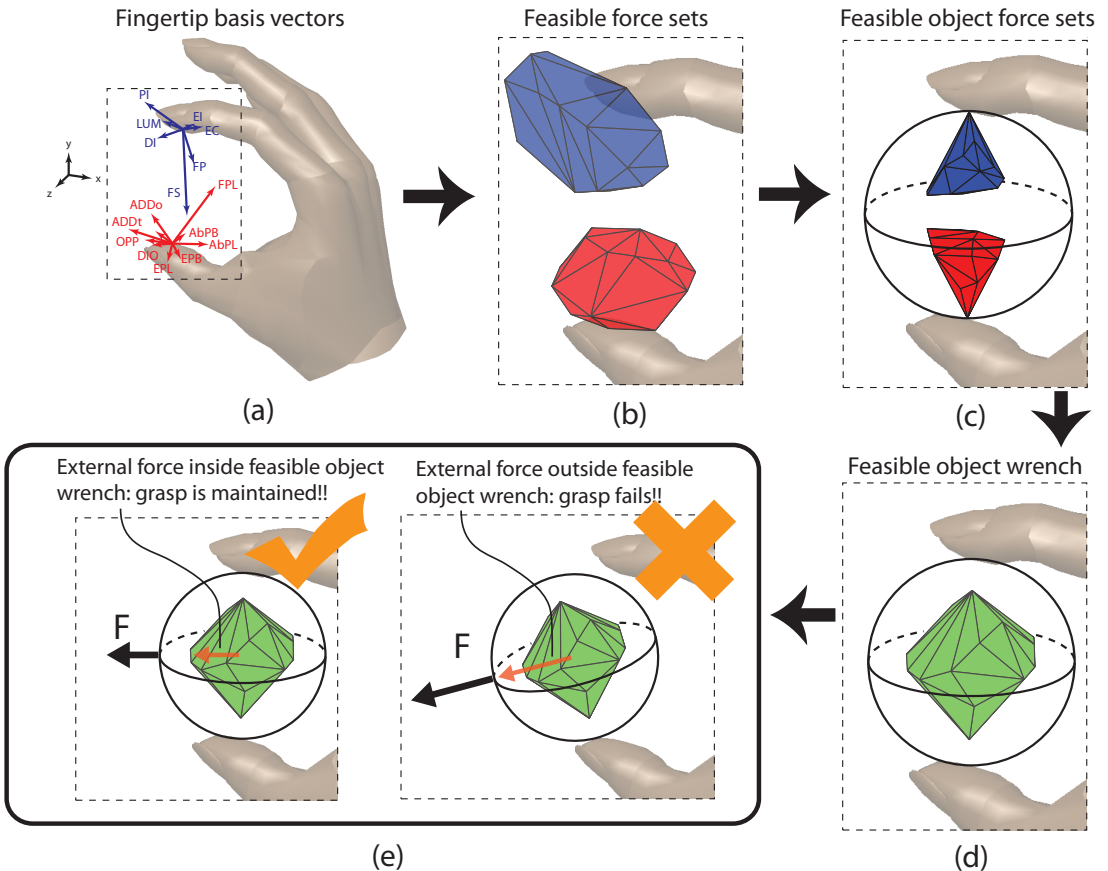


Figure 6.1: Computation of human hand grasp quality. Index finger and thumb basis vectors and feasible force sets not equal scales. (a) Fingertip basis vectors. (b) Feasible force sets built from basis vectors. (c) Feasible object force sets: intersection of feasible force sets with friction cones. (d) Feasible object wrench (only 3-D feasible forces shown). (e) Examples of maintained and failed grasps.

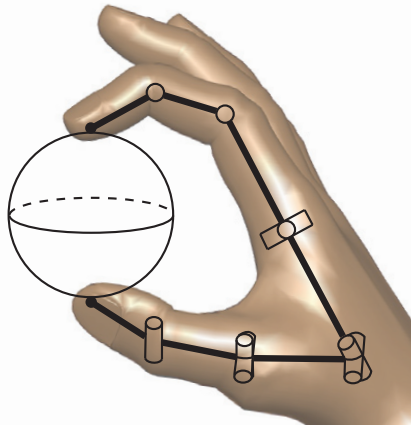


Figure 6.2: Anthropomorphic hand grasp.

and implemented previously (Inouye et al. 2012, Valero-Cuevas et al. 1998). However, while the procedure for determining the feasible force set of a tendon-driven, redundant, serial-chain manipulator has been outlined theoretically in (Fu & Pollard 2006), to our knowledge no study has ever actually implemented an algorithm for this purpose. We have developed and implemented a practical algorithm that uses vertex enumeration (Barber et al. 1996) to perform the necessary computations and find the feasible force set of the 5-DOF thumb (or any tendon-driven, redundant, serial-chain manipulator for that matter).

To allow a fair comparison of the grasp qualities of the anthropomorphic hand designs with the human hand, we tried to adhere as much as possible to the constraints that the human hand is subjected to. We set the coefficients of friction for the fingertips equal to those of human fingertips. Moreover, the sum of the maximal tendon tensions for each finger was set to that of the human fingers: 764N for the index finger and 478N for the thumb (Valero-Cuevas et al. 2000, Pearlman et al. 2004). Also, the moment arm values were constrained so that the size of each joint would not exceed that of the corresponding

Joint		Joint Diameter (mm)
Index finger	MCP Adduction-Abduction	10.9
	MCP Flexion-extension	21.0
	PIP Flexion-extension	9.25
	DIP Flexion-extension	5.14
Thumb	CMC Adduction-Abduction	35.6
	CMC Flexion-extension	40.4
	MP Adduction-Abduction	15.5
	MP Flexion-extension	20.2
	IP Flexion-extension	11.0

Table 6.1: Maximal joint diameters (i.e., differences between largest moment arms for each joint) according to data obtained from the literature.

human joints. The moment arms for the human index finger and thumb were taken from the literature (Valero-Cuevas et al. 1998, Valero-Cuevas, Johanson & Towles 2003), and the implied “joint diameters” (i.e., the maximal differences between moment arm values for a joint) were used to constrain the joint diameters for the anthropomorphic hand designs. For example, the maximal positive moment arm value for the index finger MCP joint is 13.2mm and the maximal negative moment arm value for the index finger MCP joint is -7.8mm (Valero-Cuevas et al. 1998). Therefore, the “joint diameter” is 21.0mm. The anthropomorphic hand designs were constrained so that their joint diameters were equal to those of their human hand counterparts. The joint diameters are shown in Table 6.1.

Moreover, after some initial testing and optimization, it was found that using only the above constraints resulted in optimized designs that were extremely good at grasping (more than 100% greater grasp quality than the human hand), but were extremely poor in exerting force in all directions: the *maximum isotropic value*, or MIV (the maximum force that can be exerted at the end effector in all directions, described in (Finotello

et al. 1998)), for optimized designs was less than 0.05 N. This was due to the optimization process placing all the emphasis on flexion force and none on extension force. Since this is such a low force, we felt it was necessary to constrain the MIV for anthropomorphic hand designs to be at least that of the human hand. The MIV for the human index finger is 2.89N and the MIV for the thumb is 5.37N. This ensures ability to release a grasp and for each finger to exert at least as much force in all directions as human fingers.

6.3.3 Optimizing anthropomorphic hand grasp quality

We used 3 separate steps for initializing and optimizing anthropomorphic hand designs: Monte Carlo on the structure matrices, Markov-Chain Monte Carlo on the joint centers of rotation, and Markov-Chain Monte Carlo on the distribution of maximal tendon tensions. Monte Carlo over the structure matrices was used due to the fact that the feasible force sets of the fingers, and therefore the grasp quality of the hand, are complex functions of the high-dimensional structure matrices. The Markov-Chain Monte Carlo methods were deemed appropriate due to the high dimensionality of the system and the large computational cost of computing approximate gradients (i.e., for using steepest-ascent, Newton's method, etc.).

6.3.3.1 Monte Carlo on structure matrices

For finding tendon layouts on which to perform optimization, we first performed a Monte Carlo exploration of the space of structure matrices for the fingers. We explored the space of 4 different tendon designs: $N+1$, $N+2$, $N+3$, and $2N$, where N is the number of degrees of freedom for each finger. In order to do so, we randomly generated 1000 pairs of

admissible structure matrices (one for the index finger, one for the thumb) for each of the 4 designs. These structure matrices were in a pseudotriangular form, as described in (Lee & Tsai 1991). The process of generating a random matrix for each finger is illustrated in Figure 7.1. We first began with a fixed matrix consisting of some zeros and some “#” entries where non-zero moment arm values would be inserted. Next, we randomly replaced each “#” with either a 1 or -1. We then would check feasibility conditions for controllability of a tendon-driven finger, also described in (Lee & Tsai 1991). Basically, we checked if the matrix was full rank, there was at least one sign change in each row, and we found a null vector whose elements all had the same sign using SVD. If the structure matrix was found to satisfy these conditions, we would calculate the MIV for that structure matrix. If the structure matrix was not admissible, we would randomize the structure matrix again. After a pair of admissible structure matrices were found for the index finger and thumb, we calculated the grasp quality for the pair. Therefore, we found 4000 randomized hand designs and calculated the grasp quality of each.

6.3.3.2 Optimization of joint centers of rotation

After we computed the MIV for each structure matrix, we took the 10 index finger structure matrices and the 10 thumb structure matrices with the highest MIVs and crossed them over with each other, creating 100 combinations of index finger and thumb structure matrices. This crossover operation resembles that performed in a standard genetic algorithm. The crossover we performed is illustrated in Figure 6.4. The grasp quality was then calculated for these 100 hand designs produced from crossover operations. It was reasoned that the structure matrices with the highest MIVs would be the most flexible

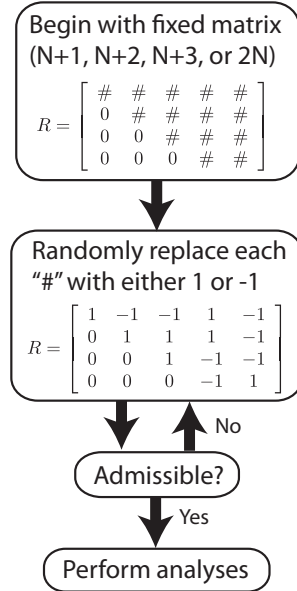


Figure 6.3: Procedure for finding randomized designs via Monte Carlo sampling.

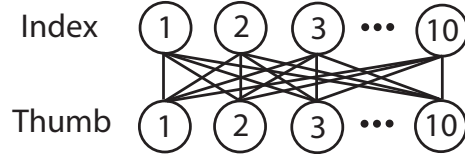


Figure 6.4: Crossover of the 10 structure matrices with the highest MIVs for each finger.

during the later stages of the optimization. In addition, the designs with the very highest grasp quality either did not meet the minimum MIV requirements or were very close to violating them.

The top 10 designs by grasp quality were then selected from the crossover results for optimization of the joint centers of rotation. This is in the sense of moment arms on one side of the joint becoming larger than those on the other side of the joint, with the total range of the moment arms being equal to the joint diameter. A greedy Markov-Chain Monte Carlo algorithm was employed on each finger separately. The initial centers

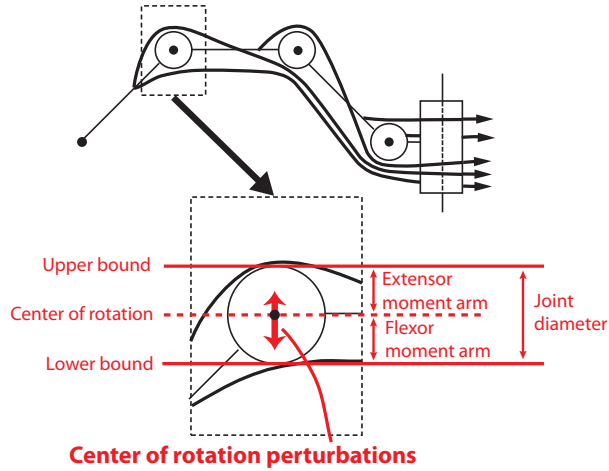


Figure 6.5: Illustration of perturbations of the joint center of rotation.

of rotation were in the middle of the joints and the grasp quality was calculated. The index finger joint centers of rotation were then perturbed simultaneously (all 4 at once) by independent, normally distributed random numbers u_i (for the i th joint) with zero mean and a standard deviation of 2% of the joint diameter. The centers of rotation were constrained so that they did not go outside the joint diameters, and a reflection technique was used similar to that in (Santos, Bustamante & Valero-Cuevas 2009). Perturbation of the center of rotation is demonstrated in Figure 6.5.

6.3.3.3 Optimization of maximal tendon tensions

The last step in our optimization process involved performing a similar Markov-Chain Monte Carlo algorithm on the maximal tendon tension distribution. Starting with all the tendons having equal maximal tendon tensions, we perturbed the distribution of the maximal tendon tensions using a multivariate normal distribution with standard deviation of 2% of the maximal tendon tension sum (764N for the index finger, 478N for

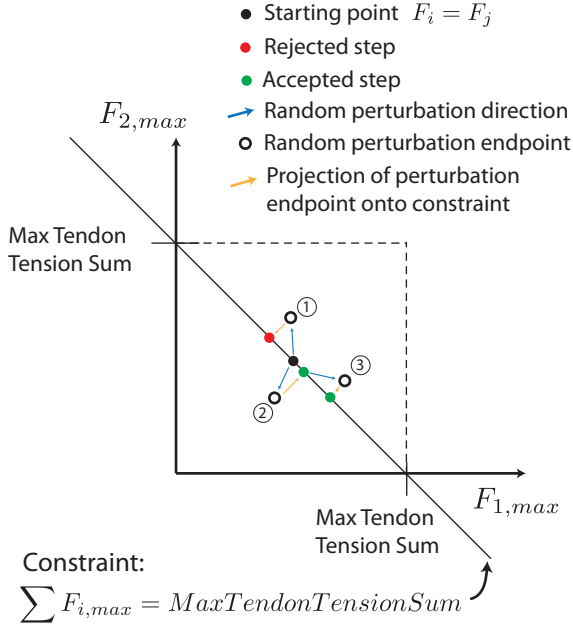


Figure 6.6: Illustration of Markov-Chain Monte Carlo algorithm for distribution of maximal tendon tensions.

the thumb). This perturbation was effectively like one inside an n -dimensional hypercube in the positive orthant with side length equal to maximal tendon tension sum, where n is the number of tendons for each finger. After perturbation inside the hypercube, we projected the point onto the hyperplane given by the following equation:

$$\sum_{i=1}^n F_{i,max} = \text{MaxTendonTensionSum} \quad (6.1)$$

where $F_{i,max}$ is the maximal tension of tendon i . This would give us a new distribution of maximal tendon tensions, and we would then evaluate the grasp quality. If it was higher, we would take that point as the starting point for the next perturbation. The same reflection technique as that of the previous section was used. The overall process is shown graphically for a simplified 2-tendon example in Figure 6.6.

A detailed explanation of the effects of different structure matrices and distributions of maximal tendon tensions on the kinetostatic (i.e., force-production) capabilities of manipulators and biological hands can be found in (Valero-Cuevas 2005, Inouye et al. 2012, Lee & Tsai 1991, Finotello et al. 1998, Ou & Tsai 1993, Ou & Tsai 1996, Tsai 1995).

6.4 Results

The results of the initial Monte Carlo and the two Markov-Chain Monte Carlo optimization steps are shown in Figure 6.7. We see that random Monte Carlo designs do very poorly in relation to the human hand. However, optimization of the joint centers of rotation and the distributions of maximal tendon tensions produces designs whose grasp quality exceeds that of the human hand, while still adhering to human hand constraints. In addition, we see that intelligently choosing parameters for hand design can result in grasp quality that is 501% higher than that of a naïve 2N design!

6.4.1 Random Monte Carlo designs

The structure matrix Monte Carlo effectively randomized the routing of the tendons prior to the other optimization procedures. We see from Figure 6.7 that there is a large range of grasp qualities for fully controllable hands. Figure 6.8 shows 3 different tendon routings for the index finger. Figure 6.8a shows the best index finger crossover design (i.e., after crossing over the fingers with the highest MIVs, as described in the methods section) that was selected for optimization. We do not show the design that had the highest grasp quality from the Monte Carlo designs because the MIVs of the fingers were too low to meet human hand constraints. Figure 6.8b shows an index finger tendon routing that

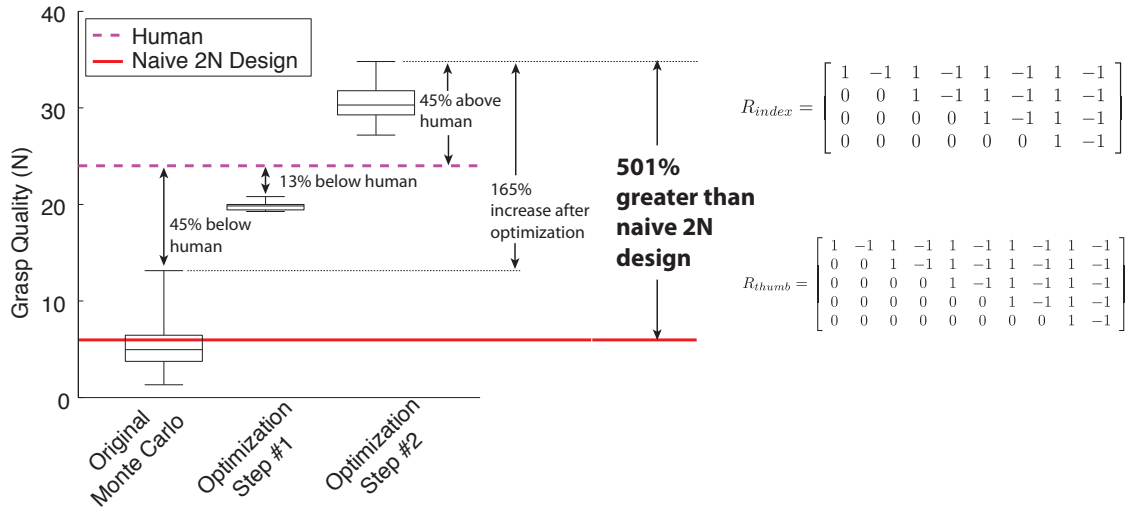
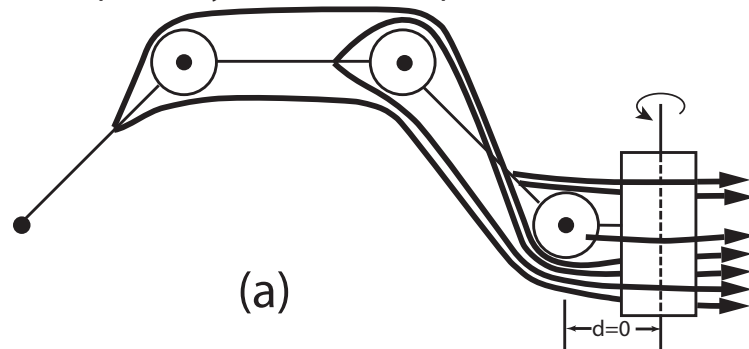


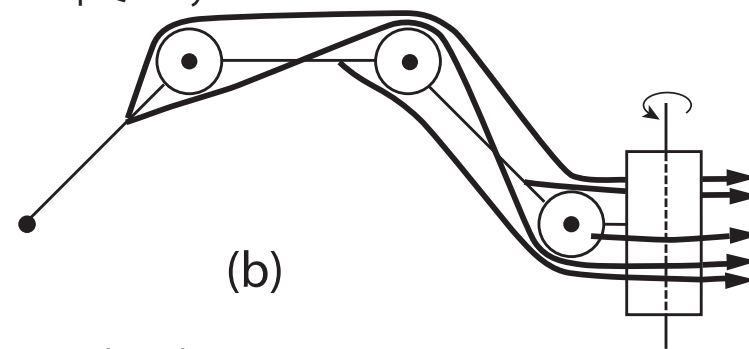
Figure 6.7: Comparison of human grasp quality with boxplots of anthropomorphic hand designs. Optimization step #1 is for the joint centers of rotation. Optimization step #2 is for the distribution of maximal tendon tensions.

produced a very poor grasp quality. Figure 6.8c shows a typical 2N design, which is similar to that used in the current Shadow Hand design and other tendon-driven designs. Its grasp quality (combined with a similar 2N routing for the thumb) is only about half of that of the design from Figure 6.8a. It should be noted that this figure does not draw the moment arms to scale. It only shows which sides of the joints the tendons cross. In addition, for the purposes of kinematic clarity, the finger ad-abduction (i.e., side-to-side) axis was considered to be immediately proximal to the perpendicular axis of the first flexor-extensor joint, as demonstrated in Figure 6.8a.

Very good Monte Carlo design.
Grasp Quality: 11.9 (before optimization).



Very bad Monte Carlo design.
Grasp Quality: 2.33



Typical 2N design.
Grasp Quality: 5.96

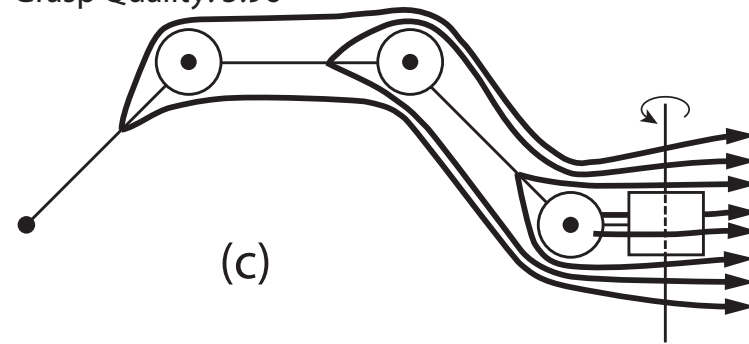


Figure 6.8: Various index finger tendon routings. Not to scale. (a) Best crossover index finger design selected for optimization. (b) Example of an index finger tendon routing that produced a very low grasp quality. (c) Typical 2N design.

6.4.2 Optimization of joint centers of rotation and distribution of maximal tendon tensions

We optimized the top 10 hand designs produced from the crossover operations. We used 150 iterations for the joint centers of rotation optimization for each finger separately. Results from using 10 random starting locations for the index finger within the space of allowable centers of rotation as well as a starting location in the middle of all the joints showed that the random seeds all converged to roughly the same point, with a small range in final grasp quality, as shown in Figure 6.9a. The range of grasp qualities for the random seeds was 16.08-16.19N, or 0.7% of the mean.

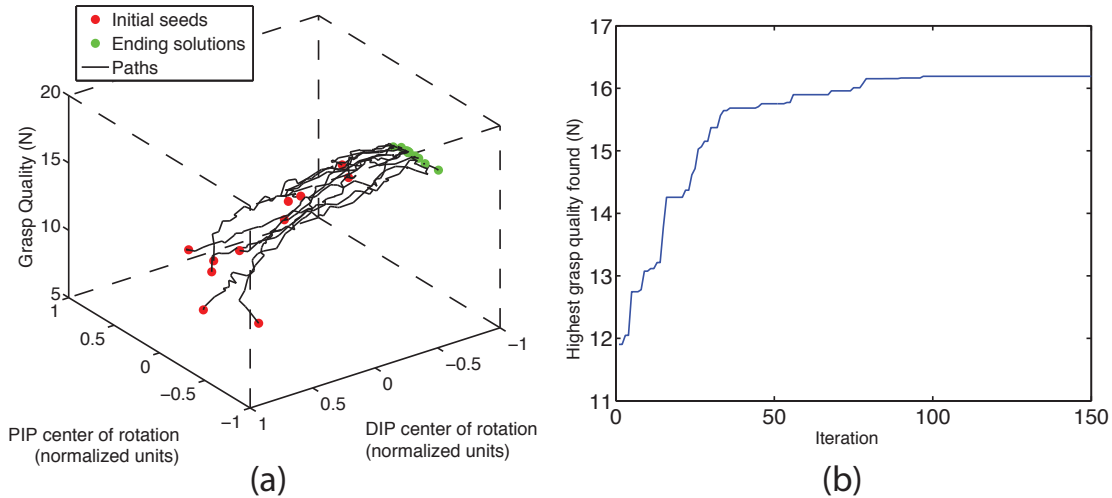


Figure 6.9: Markov-Chain Monte Carlo optimization. (a) Visualization of optimization paths of 10 random seeds and one center seed. (b) Optimization progress over 150 iterations.

Therefore, we deemed that the 150 iterations allowed sufficient convergence for our study, and also that running multiple Markov Chains for each design was unnecessary. It should be noted that although the 10 random seeds were randomly selected from a

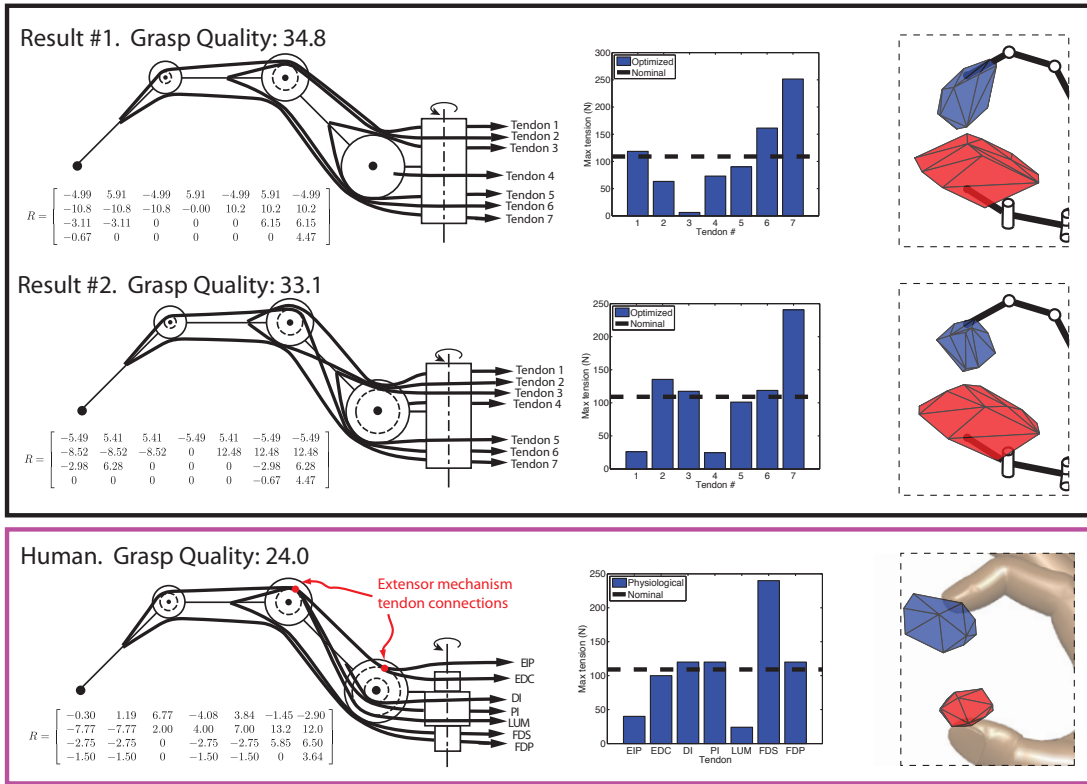


Figure 6.10: Index finger tendon layout, maximal tendon tension distribution, and feasible force sets for top 2 optimized designs and the human hand. Tendon layouts shown roughly to scale. Feasible force sets shown to scale.

uniform distribution in the theoretically allowable range (i.e., within the unit hypercube; 2 selected dimensions shown in Figure 6.9a), some seeds did not meet minimum MIV requirements, and they were discarded and re-randomized. The final solutions shown in Figure 6.9a are slightly dispersed in the PIP center of rotation, but the range of grasp qualities is very small, suggesting a very flat fitness landscape in that vicinity along that direction.

In addition, we see the progress of the best found result versus iteration number in Figure 6.9b. Graphically, it can be seen that over the course of 150 iterations, most of the improvement (almost 85%) comes in the first 50 iterations. While we allowed the

optimization to run for 3 times that long, we felt that any more iterations would result in diminishing returns and marginal improvements in results. It took about 3.7 seconds, on average, to compute the grasp quality for each iteration. The optimization of the joint centers of rotation produced designs with grasp qualities between 19.3N and 20.8N, falling short of the human grasp quality by 13-20%, and 17% on average, as shown in Figure 6.7.

We used 150 iterations as well for the Markov-Chain Monte Carlo optimization of the distribution of maximal tendon tensions for each finger separately. We tried random seeding, but the result of using 10 random seeds (same technique as that used in the joint center of rotation random seeds) produced grasp qualities with a very small range (5.5% of the mean). Again, this indicated that multiple chains were unnecessary for our purposes. A plot of typical optimized grasp quality versus iteration number was very similar to that shown in Figure 6.9b (in fact, with 96% of the improvement coming within the first 50 iterations), and therefore the 150 iterations were deemed sufficient. The optimization of maximal tendon tension distributions produced designs with grasp qualities that were on average 55% higher than those with evenly distributed maximal tendon tensions.

The full optimization of the best crossover designs produced hands whose grasp quality exceeded that of the human hand by 13-45%, shown in Figure 6.7. The index finger routing, the distribution of maximal tendon tensions, and the feasible force sets for the best 2 designs and the human hand design are shown in Figure 6.10. Interestingly, the feasible force set of the human index finger is much larger than that of the thumb, while the opposite is true with the optimized designs. It can be seen that the optimization

caused the feasible force sets to be weighted more heavily toward the palmar direction (i.e., the direction of force production during grasping).

6.5 Discussion

In this study, we have successfully compared thousands of random and optimized hand designs to the human hand in terms of grasp quality. We demonstrate the use and power of the methodology developed in (Inouye et al. 2012) to compare and optimize hand designs in a high-dimensional parameter space, while still adhering to specific design constraints.

As mentioned earlier, the optimization caused the feasible force sets to be weighted more heavily toward the palmar direction. In the human index finger however, the feasible force set is weighted both in the palmar direction and also in the *distal* direction, as can be seen in Figure 6.10. The feasible force set being weighted in this direction would indicate optimization for other tasks that would utilize this direction. Consider a hand picking up a heavy bar, shown in Figure 6.11. In this case, we have a power grasp, and the fingertip is not supporting much of the weight of the bar, but the finger itself must exert a force in that direction. This could suggest that power grasp of very heavy objects in this manner is also something the human hand, to a certain extent, is optimized for.

As can also be seen in Figure 6.10, the optimized thumb feasible force sets were much larger than that of the human. One explanation for this is that all the tendons in the optimized designs were at the boundaries of their joint diameters. In the human, the extreme moment arms defined the joint diameters, but the rest of the tendons typically

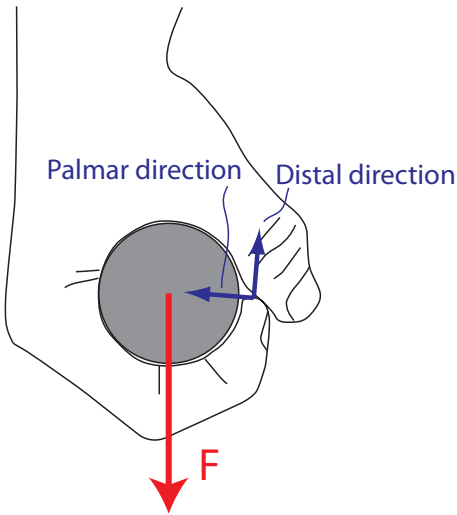


Figure 6.11: Power grasp of a heavy bar. The hand must resist a force that is opposite the distal direction of the index finger.

were not nearly as large as these extremes. For example, the maximal human MCP flexion moment arm was 13.2mm and the maximal extension moment arm was 7.77mm, giving a joint diameter of 21.0mm. If this was an optimized robotic hand, all the flexion moment arms would be 13.2mm and all the extension moment arms would be 7.77mm. However, in the human, only one flexor has a moment arm this large and only one other extensor has a moment arm this large. The other 4 tendons have smaller moment arms at this axis. Due to the fact that the joint diameters for the thumb CMC joint were quite large, the optimized designs were able to take full advantage of having many large moment arms, while the human thumb only used 2 moment arms to the maximum extent possible.

Our study concentrated on the grasp of one object of a reasonable size in a specific posture. We did not perform extensive sensitivity analysis on certain factors such as differing postures, finger placements, friction coefficients, surface curvatures, object shapes,

etc. The methodology that we employed would allow simulations to take most of these factors into account, but we felt that this was not necessary to arrive at our basic conclusions. In addition, we assumed no force-length interaction in the human muscles to affect the maximal tendon tensions (Zajac 1989).

Furthermore, we have only scratched the surface of the optimization techniques that could be employed in order to even further improve the results. Varying the optimization techniques, parameters, or orders of steps could affect the upper limit of grasp qualities found. We did not feel that it was necessary or feasible to find a global optimum, and we felt that our results would not be significantly affected by spending much more time and effort trying to get, say, 10-20% higher grasp quality than we found for the optimized designs. Also, the optimization only occurred on specific initial structure matrices for the various designs. However, thousands of other initial structure matrices could also be used and optimized (Sheu et al. 2009).

This paper concentrates on the upper limit of the mechanical capabilities of hands in relation to grasp quality. Nearly all (grasping) tasks performed are far from the mechanical boundaries defined by theoretical or practical means. However, it is generally desirable to perform tasks that are not too close to the mechanical boundary limit and to have some sort of “safety factor” in place. If the task is well-defined, then the linear programming approach used in (Fu & Pollard 2006) is well-suited to calculating this safety factor. In the general case where many tasks must be performed or the hand is performing tasks in unstructured environments, global grasp metrics (such as those used in this study and in (Inouye et al. 2012) must be used to assess the fitness of various designs.

We note that in any useful biological or robotic hand, the mechanics *and* control must both be considered and developed. The best control algorithms cannot perform any task that the mechanics are not designed for. Moreover, a globally-optimal hand from a mechanics standpoint is useless without effective control to utilize these capabilities. The consequences to control of various designs have not been considered in this paper, and this is the subject of future work: is a tendon-driven hand with an optimized grasp quality difficult to control?

One exciting conclusion of this study is that utilizing even the fairly simple Monte Carlo exploration and optimization techniques we employed can improve grasp quality of robotic hands by nearly an order of magnitude (501% increase) when compared with the naïve 2N design. While the scientific insight (involving the human hand) of this study is interesting from an intellectual and academic perspective, we feel that the implications for the industrial design of robotic hands are perhaps the most useful findings from this study.

Acknowledgements

The authors gratefully acknowledge the useful discussions with J. Kutch.

Chapter 7

Asymmetric Routings With Fewer Tendons Can Offer Both Flexible Endpoint Stiffness Control and High Force-Production Capabilities in Robotic Fingers

7.1 Abstract

The force-production and passive stiffness capabilities of fingers are two critical design specifications for dexterous robotic hands. We used the link and joint kinematic parameters of the 4-DOF DLR index finger to explore the tradeoff between these two design specifications as a function of the number, routing, stiffness, and strength of each tendon. Our innovative computational approach allowed building the Pareto front of optimized passive endpoint stiffness (measured by the eccentricity of the endpoint stiffness ellipsoids) vs. maximal force-production capabilities (measured by the size and shape of the force polytope) for 1,200 randomly generated valid routings with 5, 6, 7, or 8 tendons. Our results show that this parametric optimization can increase realizable isotropic forces by up to 80% compared to the default tendon tension distribution. In addition, designs

with 5 or 6 tendons can have endpoint stiffness ellipsoids with optimized low eccentricities and with force production capabilities comparable to designs with 7 or 8 tendons. Interestingly, we did not find a systematic tradeoff between force-production and passive stiffness capabilities, given a specific routing. However, the choice of number, routing and strength of each tendon greatly affects force and passive stiffness capabilities of robotic finger, which reveals the many design opportunities afforded by tendon-driven manipulators and offers insight into the anatomical features of the human musculoskeletal system.

7.2 Introduction

Robotic fingers and hands have been designed for the past few decades for the purposes of grasping and manipulation (Jacobsen et al. 1986, Salisbury & Craig 1982, Shadow Robot Company n.d., Grebenstein et al. n.d., Ambrose et al. 2000). There are many factors involved in the design decisions for these hands, but two important ones are force-production capabilities and passive stiffness. The fingers clearly must be able to generate sufficiently high forces to perform a specific or general task. In addition, the integration of passive stiffness control into the design of robotic hands is important for preventing damage to itself and its surroundings, enabling the ability to perform highly dynamic tasks, and increasing the safety of interacting humans (Wolf & Hirzinger 2008, Pratt & Williamson 1995, Grebenstein & van der Smagt 2008).

Several studies have addressed the problem of identifying the force-production (or more formally, wrench-production) capabilities of both parallel and serial manipulators (Bouchard et al. n.d., Chiacchio et al. 1997, Firmani et al. 2008, Finotello et al. 1998,

Gouttefarde & Krut 2010, Zibil et al. 2007, Kuxhaus et al. 2005, Valero-Cuevas et al. 1998). According to (Firmani et al. 2008), "The knowledge of maximum twist and wrench capabilities is an important tool for achieving the optimum design of manipulators". Two common approaches to the problem of quantifying these capabilities are manipulating force ellipsoids (which apply accurately only to torque-driven systems) and force polytopes (also known as feasible force sets, which apply exactly to tendon driven systems (Valero-Cuevas et al. 2009). From these force-production capabilities, a performance metric can then be assigned based on the size and/or shape of the ellipsoid or polytope.

For tendon-driven robotic fingers, one key design element is the tendon routing, which defines the structure matrix, of the finger. This structure matrix defines the torque and force produced by the finger based on tensions of the tendons. Certain studies have addressed the problem of designing a structure matrix for isotropic force transmission characteristics (i.e., ability to transmit forces equally in all directions at the end effector) (Tsai 1995, Sheu et al. 2009, Lee & Tsai 1991, Chen et al. 1999, Ou & Tsai 1996, Ou & Tsai 1993). However, these studies have not considered the distribution of maximal tensions across tendons, which is certainly important in small, dexterous hands where weight and size minimization are significant priorities. Altering the maximal tendon tension distribution in tendon-driven hands is known to have a significant effect on force-production capabilities (Pollard & Gilbert 2002, Inouye et al. 2011*b*). Additionally, the number of tendons used in the design is fundamental to the design of the structure matrix, and using fewer tendons "has the advantage of reducing the number of tendons and actuators and therefore reduces the weight, size, and complexity of the manipulator..." (Tsai 1995).

The importance of stiffness control of manipulators has been widely recognized in the literature(Wolf & Hirzinger 2008, Pratt & Williamson 1995, Grebenstein & van der Smagt 2008, Grebenstein et al. n.d., Hashimoto & Imamura 1994, Hogan 1985*a*, Ott 2008, Starr 1988). Manipulators can have active or passive stiffness control, or a combination of both. Active stiffness control can be programmed using a feedback control law (Hogan 1985*a*), but is limited by the control loop frequency, and a sudden impact to the manipulator can cause damage to the robot or its surroundings before the control loop is activated to absorb the energy (Grebenstein et al. n.d.). Thus, passive stiffness is also important, especially in unstructured environments where unexpected obstacles, objects, or humans may make contact with the manipulator. Passive stiffness control is typically implemented by variable-stiffness actuators (Laurin-Kovitz, Colgate & Carnes 1991, Wimbock, Ott, Albu-Schaffer, Kugi & Hirzinger 2008, Wolf & Hirzinger 2008, Pratt & Williamson 1995, Sugano, Tsuto & Kato 1992, Grebenstein, Chalon, Hirzinger & Siegwart 2010, Kobayashi et al. 1998). Synthesis of endpoint stiffness for serial manipulators with adjustable joint stiffnesses is studied in (Huang & Schimmels 2000). An extensive analysis of the joint stiffness matrices for tendon-driven manipulators is conducted in (Kobayashi et al. 1998).

Therefore, it is clearly desirable to design a robotic hand with both adequate passive stiffness and high force-production capabilities. In addition, it can be beneficial to design a finger with as few tendons as possible. Utilizing computational methods and applying theoretical analyses, we quantify the ability of 1,200 tendon routings to produce maximal isotropic forces and endpoint stiffness ellipsoids with low eccentricity. This novel approach enables the systematic exploration of the design space. For example, we show that fewer tendons does not imply worse passive stiffness, but designs with fewer tendons typically

cannot produce as much isotropic force as designs with more tendons. Tuning tendon stiffnesses can lead to endpoint stiffness ellipsoids with low eccentricity, and adjusting the distribution of maximal tension across tendons can lead to large increases in isotropic force-production capabilities. Our study demonstrates, to the best of our knowledge, the first practical computational exploration of the effect of tendon routing simultaneously on these two characteristics.

7.3 Methods

The minimal number of tendons required to fully control all of the degrees of freedom (DOFs) of an n -joint robotic finger is $n + 1$ (Ou & Tsai 1993). Because tendons have unidirectional actions (i.e., they can only pull), this minimal number of tendons must also be routed judiciously (Valero-Cuevas et al. 2009). A finger with this many tendons employs what is called an “N+1” design. The DLR finger and most anthropomorphic fingers have 4 DOFs (that do not use coupled joints), which means that the minimal number of tendons for full controllability of the finger is 5. However, many hands have been designed using a “2N” design, which uses a number of tendons equal to 2 times the DOFs—with a pair of agonist-antagonist tendons dedicated to each joint (Grebenstein et al. n.d., Jacobsen et al. 1986, Shadow Robot Company n.d.). In general, increasing the number of tendons beyond 2N is impractical or undesirable for robotic fingers because of size constraints¹. In addition, any number of tendons between N+1 and 2N may be

¹However, most vertebrate limbs have more than 2N muscles—which is a subject of continual debate. See (Valero-Cuevas et al. 2009, Kutch & Valero-Cuevas 2011)

used. We carried out analyses on 4 categories of designs: having 5 ($N+1$), 6 ($N+2$), 7 ($N+3$), or 8 ($2N$) tendons.

The routing and moment arms of tendons in a finger are critical, and can be mathematically described by an $n \times m$ structure matrix (also called a moment arm matrix) R , where n is the number of DOFs of the finger and m is the number of tendons. The entries $r_{i,j}$ are signed moment arm values for the i^{th} joint and j^{th} tendon (Tsai & Lee 1988). For simulation purposes, we randomly selected 300 admissible structure matrices from each of the tendon categories by randomizing the signs of the non-zero entries and then checking for controllability conditions ² as described in (Lee & Tsai 1991). This process is shown in Figure 7.1, with the non-zero entries represented by '#'. The number of admissible structure matrices for all categories combined is 222,208 (using a combinatoric search of the '#' entries in Figure 7.1 for each category). Therefore, evaluating all of these designs is relatively intractable for our purposes and we deemed that randomly selecting 300 from each category for a total of 1,200 evaluated routings was sufficient to prove the point of this study.

To compare and contrast the force-production and stiffness capabilities of various finger designs, we identified a fitness metric describing each aspect. We calculated these metrics at 3 different postures for each of the 1,200 routings, and averaged the metrics over the 3 postures, which are shown in Figure 7.2.

The fitness metric used for stiffness control was the ESE (endpoint stiffness eccentricity) and the metric used for force production was the MIV (maximal isotropic value). The calculation of these metrics is described in the next sections.

²The basic idea behind the controllability conditions is that each joint can be actuated independently in torque and motion, given that tendons can only pull and not push.

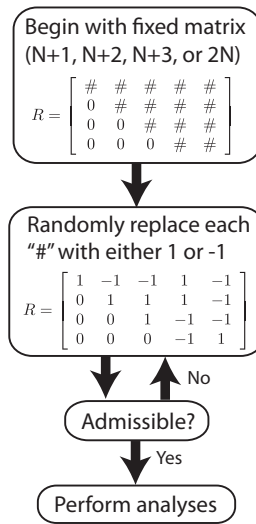


Figure 7.1: Procedure for finding admissible structure matrices. N+1 structure matrix shown.

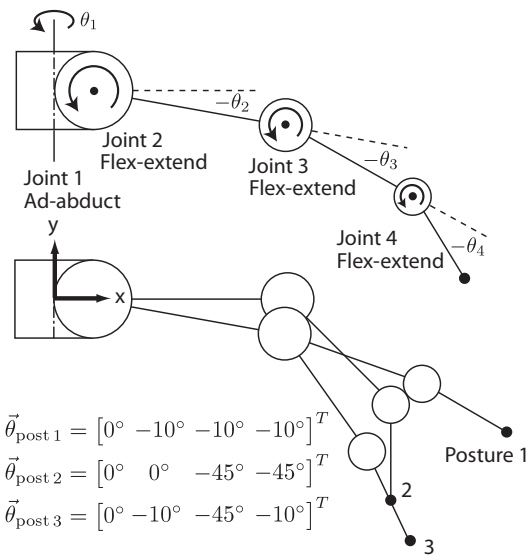


Figure 7.2: Postures analyzed for each tendon routing. Link lengths and joint diameters shown to scale (i.e., with kinematic parameters of the DLR hand).

7.3.1 Analysis and Synthesis of Stiffness

7.3.1.1 Joint Stiffness Adjustability

The endpoint Cartesian stiffness matrix, K_{end} , relates the endpoint displacements (from an equilibrium position), $\vec{\partial x}$, to endpoint forces, \vec{F} , as shown in the following equation:

$$\vec{F}_{end} = -K_{end}\vec{\partial x} \quad (7.1)$$

The joint stiffness matrix, K_{joint} , relates the joint displacements (from an equilibrium position), $\vec{\partial \theta}$, to joint torques, $\vec{\tau}$, as shown in the following equation:

$$\vec{\tau} = -K_{joint}\vec{\partial \theta} \quad (7.2)$$

The endpoint stiffness matrix can be found from the joint stiffness matrix using the following well-known equation (Pashkevich, Klimchik & Chablat 2011, Hogan 1990, Chen & Kao 2000, Alici & Shirinzadeh 2005, McIntyre, Mussa-Ivaldi & Bizzi 1989):

$$K_{end} = J^{+T}(K_{joint} - \frac{\partial J^T}{\partial \theta} \vec{F}_{tip})J^+ \quad (7.3)$$

where J is the posture-dependent Jacobian relating joint angle velocities to endpoint velocities, J^+ is the Moore-Penrose pseudoinverse of J (if the manipulator is redundant, as is the case in this study), and \vec{F}_{tip} is the external force vector on the tip of the finger. The joint stiffness matrix for a tendon-driven finger may be found from the structure matrix R and the diagonal tendon stiffness matrix K_t using the following equation (McIntyre, Mussa-Ivaldi & Bizzi 1996):

$$K_{joint} = R K_t R^T \quad (7.4)$$

For the purposes of this computational study, we assume that the external force on the fingertip is zero. However, similar computational studies could be conducted with an external fingertip force. Combining Eqs. 7.3 and 7.4 with the external force being zero, we get the endpoint stiffness matrix as a function of tendon stiffnesses and tendon routing:

$$K_{end} = J^{+T} (R K_t R^T) J^+ \quad (7.5)$$

For the DLR index finger in an unloaded configuration (Equation 7.3 changes if there is a constant load applied to the endpoint (McIntyre et al. 1996)), K_{end} is a 3×3 symmetric, positive semi-definite matrix, K_{joint} is a 4×4 symmetric, positive semi-definite matrix, J is a 3×4 matrix, R is a $4 \times m$ matrix (m is the number of tendons ranging from 5-8), and K_t is an $m \times m$ diagonal matrix.

We can see clearly from Equation 7.3 that the endpoint stiffness is a function of joint stiffness, and that realizing a completely arbitrary endpoint stiffness can be difficult in general due to the multiplication by the Jacobian and the inversions involved. Depending on the configuration, it may or may not be possible to realize an arbitrary endpoint stiffness matrix (Huang & Schimmels 2000) because of the constraint that the joint stiffness matrix must be positive definite. It can be noted that an arbitrary 3-D endpoint stiffness matrix involves 6 free parameters. Therefore, if there are not at least 6 free parameters in the joint stiffness matrix, it is not possible to realize an arbitrary endpoint stiffness.

For the 4-DOF DLR finger, the joint stiffness matrix is 4×4 , and so there are 10 free parameters. Reformulating Equation 7.4 enables quantification of the *joint stiffness adjustability* (JSA), which can be interpreted as the flexibility of realizing a joint stiffness matrix for a specific routing when tendon stiffness selection is arbitrary. The reformulation (Kobayashi et al. 1998) involves rearranging the independent parameters of the joint stiffness matrix into a vector, which is then a linear function of the tendon stiffness, also rearranged into a vector:

$$\vec{K}_{joint} = \tilde{R} \vec{K}_t \quad (7.6)$$

where \vec{K}_{joint} , \tilde{R} , and \vec{K}_t are reformulated as shown in Figure 7.3. (\bullet) denotes element-by-element multiplication, and R_i is the i^{th} row of R . Note that \vec{K}_{joint} has length $n(n+1)/2$ (where n is the number of DOFs of the finger), \tilde{R} is an $n(n+1)/2 \times m$ matrix (where m is the number of tendons of the finger), and \vec{K}_t has length m , and all of its elements must be positive. Mathematically, the rank of \tilde{R} is the number of free parameters of the joint stiffness matrix that can be independently chosen. Of course, the tendon stiffnesses must be positive, and the range of realizable joint stiffnesses is constrained by a particular routing, but this is nevertheless an estimation of the freedom in choosing an arbitrary joint stiffness matrix (Kobayashi et al. 1998), which in turn affects the freedom to choose an arbitrary endpoint stiffness matrix. The rank of \tilde{R} is the joint stiffness adjustability (JSA):

$$JSA = \text{rank}(\tilde{R}) \quad (7.7)$$

$$\begin{aligned}
K_{joint} &= \begin{bmatrix} K_{11} & K_{12} & \cdots & K_{1n} \\ K_{12} & K_{22} & \cdots & K_{2n} \\ \vdots & \vdots & \ddots & \vdots \\ K_{1n} & K_{2n} & \cdots & K_{nn} \end{bmatrix} \\
\downarrow & \\
\vec{K}_{joint} &= \begin{bmatrix} K_{11} \\ K_{12} \\ \vdots \\ K_{1n} \\ K_{22} \\ \vdots \\ K_{2n} \\ \vdots \\ K_{nn} \end{bmatrix} \quad K_t = \begin{bmatrix} K_{t,1} & K_{t,2} & \cdots & K_{t,m} \\ 0 & & & \\ & & \ddots & \\ & & & K_{t,m} \end{bmatrix} \\
\downarrow & \\
\vec{K}_t &= \begin{bmatrix} K_{t,1} \\ K_{t,2} \\ \vdots \\ K_{t,m} \end{bmatrix} \\
R &= \begin{bmatrix} \text{---} & R_1 & \text{---} \\ \text{---} & R_2 & \text{---} \\ \vdots & & \vdots \\ \text{---} & R_n & \text{---} \end{bmatrix} \\
\tilde{R} &= \begin{bmatrix} R_1 \bullet R_1 \\ R_1 \bullet R_2 \\ \vdots \\ R_1 \bullet R_n \\ R_2 \bullet R_2 \\ \vdots \\ R_2 \bullet R_n \\ \vdots \\ R_n \bullet R_n \end{bmatrix}
\end{aligned}$$

Figure 7.3: Reformulation of variables in Equation 7.4 for use in Equation 7.6. (\bullet) denotes element-by-element multiplication. R_i is the i^{th} row of R . Joint stiffness adjustability (JSA) is equal to $\text{rank}(\tilde{R})$.

Note again that this measure assumes that each tendon stiffness can be independently chosen, regardless of tendon tension.

7.3.1.2 Endpoint Stiffness Eccentricity

As suggested above, higher JSA will, in general, translate to a larger set of realizable endpoint stiffnesses. We quantify the ability of a specific routing to realize an endpoint

stiffness ellipsoid³ with low eccentricity by formulating the following optimization problem:

$$\underset{K_t}{\text{minimize}} \quad \kappa(K_{end})$$

$$\text{subject to} \quad K_t \geq 0$$

where $\kappa(\cdot)$ denotes the condition number: the ratio of the largest to the smallest singular values of the matrix. It is a measure of the eccentricity of the endpoint stiffness ellipsoid(Stroeve 1999). We will call this the *endpoint stiffness eccentricity*, or ESE.

$$\text{ESE} = \kappa(K_{end}) \tag{7.8}$$

We implemented the above optimization in Matlab using the ‘fmincon’ command. Condition number minimization is a difficult problem in general (Elsner, He & Mehrmann 1995, Lu & Pong 2010, Chen, Womersley & Ye 2011). It is quasi-convex over the entries of the matrix, but the entries of the matrix are non-convex functions of the elements of \vec{K}_t in our problem due to the matrix inversions. However, taking the best result from 5 random starting points in the positive unit hypercube (i.e., positive orthant) seemed to give good, repeatable results. The optimized endpoint stiffness eccentricity, ESE*, quantifies the eccentricity of the best-conditioned stiffness ellipsoid that the optimization was able to find. It can be noted that minimizing the eccentricity of the ellipsoid is equivalent to

³The stiffness ellipsoid is formed by projecting a unit sphere from differential displacements to differential endpoint forces using the linear transformation K_{end} , as in Equation 7.1. It assumes infinitesimal displacements that have negligible effects on the Jacobian matrix. Large displacements will not be as accurately represented by ellipsoids due to larger changes in the Jacobian matrix.

maximizing its isotropy. A perfectly spherical stiffness ellipsoid has a condition number of 1.

7.3.2 Analysis and Optimization of Force Polytopes

The feasible force set is the convex polytope of all forces that can be exerted by the endpoint of a tendon-driven finger, given a posture, tendon routing, and maximal tendon tensions (Valero-Cuevas et al. 1998, Pollard & Gilbert 2002, Chiacchio et al. 1997). Any force vector outside of this 3-D set (or 2-D set, for planar analyses) cannot be achieved by the endpoint. A quality metric that can be assigned to this set is known as the maximal isotropic value (MIV) (Finotello et al. 1998). It is the radius of the largest ball, centered at the origin, that the feasible force set can contain. A finger can exert at least that many units of force in any direction.

To find the feasible force set, we first specify the posture (which allows computation of the Jacobian J) and tendon routing R of the finger. These matrices involve the following relations:

$$\dot{x} = J\dot{\theta} \quad (7.9)$$

$$\vec{\tau} = R\vec{T} \quad (7.10)$$

where \dot{x} is the endpoint translational velocity vector, $\dot{\theta}$ is the joint velocity vector, and \vec{T} is the vector of tendon tensions.

We can use an activation vector, \vec{a} , to represent the degree to which a tendon is activated. Each element of \vec{a} ranges between 0 (no activation) and 1 (full activation).

Further discussion may be found in (Valero-Cuevas 2005). If we define T_{max} as a diagonal matrix of maximal tendon tensions, then we get the following relation between activations and tendon tensions:

$$\vec{T} = T_{max} \vec{a} \quad (7.11)$$

If we combine Eqs. 7.10 and 7.11, then we get:

$$\vec{\tau} = RT_{max} \vec{a} \quad (7.12)$$

The feasible 3-D force set can be found from this feasible torque set by intersecting the feasible torque set with the linear subspace spanned by the columns of J^T (Fu & Pollard 2006). The vertices of this reduced-dimensionality set can then be transformed to vertices in endpoint force space:

$$\vec{F} = J^{+T} \vec{\tau} \quad (7.13)$$

where J^{+T} denotes the Moore-Penrose pseudoinverse of J^T . The convex hull of all of these vertices in force space is a polytope and defines the feasible force set. We use the Quickhull algorithm (Barber et al. 1996) implemented in the Qhull software package to find the MIV.

Different routings and maximal tendon tensions both affect the size and shape of the feasible torque set shown in Equation 7.12, which in turn affects the size and the shape of the feasible force set. If we have a fixed routing and posture, then we can change the

feasible force set and MIV by varying the maximal tendon tensions (given by diagonal matrix T_{max}). If we constrain the sum of the maximal tendon tensions to be constant (a reasonable constraint due to the size and weight constraints inherent in dexterous hands (Pollard & Gilbert 2002)), then we can optimize the MIV using the following formulation:

$$\underset{F_0}{\text{maximize}} \quad \text{MIV} = f(J, R, T_{max})$$

$$\text{subject to } T_{max} \geq 0,$$

$$\text{trace}(T_{max}) = T_{\max \text{ sum}}$$

where $T_{\max \text{ sum}}$ is a constant.

Evaluating the MIV given J , R , and T_{max} is fairly expensive computationally when compared with function evaluations for the stiffness problem. Therefore, we utilized a custom, greedy Markov-Chain Monte Carlo optimization algorithm which was fairly effective at finding a local maximum within 300 iterations. We denote this maximum by MIV^* .

It is worth noting that MIV is a function of J , R , and T_{max} , while the ESE is a function of J , R , and K_t . Therefore, changes in T_{max} will not affect the ESE and changes in K_t will not affect the MIV. However, the Jacobian matrix and the routing have effects on *both* of these characteristics. This study is focused mostly on the effects of *routing* on these two characteristics. It can also be noted that with a torque-driven manipulator, the analysis of force production and stiffness synthesis becomes much less interesting, as there are very few design parameters that can be altered compared with the tendon-driven manipulator. Furthermore, torque-driven manipulators are not able to utilize the advantages of tendon-driven manipulators as stated in the introduction.

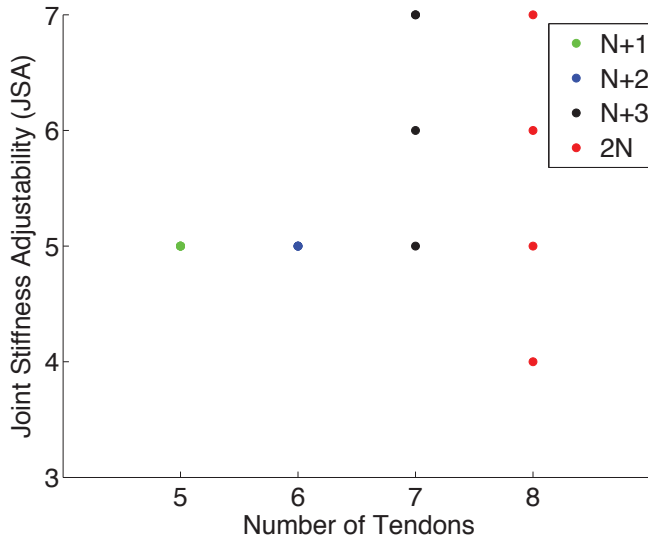


Figure 7.4: Joint stiffness adjustability versus number of tendons, plotted for all admissible routings. Mathematically, JSA is the rank of \tilde{R} , which is the number of free parameters of the joint stiffness matrix that can be independently chosen.

7.4 Results

7.4.1 Joint Stiffness Adjustability

We were able to determine the JSA of all 222,208 admissible tendon routings. The results are shown in Figure 7.4. We see that designs with 5 or 6 tendons have a JSA of 5, while designs with 7 or 8 tendons can have a JSA of up to 7 (but never 8!). However, some designs with 8 tendons can only have a JSA of 4, which corresponds to symmetric routings (a 2N design where the moment arms of one tendon are the opposite sign and equal magnitude of those from another tendon), as noted in (Kobayashi et al. 1998). A symmetric routing which controls all of the degrees of freedom of an N-DOF manipulator requires at least 2N tendons, so routings of a 4-DOF finger with 5, 6, or 7 tendons cannot be symmetric.

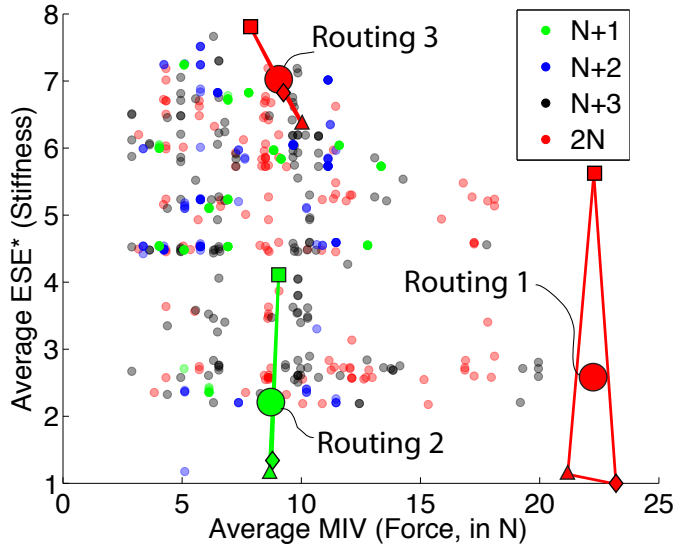


Figure 7.5: Optimized endpoint stiffness eccentricity (ESE*) vs. unoptimized maximal isotropic value (MIV), averaged over the 3 postures. Note: only 524 out of 1,200 data points shown (all other designs had higher ESE* than 8 and lower MIV than 16). Large circles mark the averages of posture 1 (small squares), posture 2 (small triangles), and posture 3 (small diamonds) for the routings shown in Figure 7.6.

7.4.2 Optimized Endpoint Stiffness Eccentricity vs. Maximal Isotropic Value

For the 300 randomly-selected routings from each category, we found the ESE* (optimized ESE) and the unoptimized MIV, shown in Figure 7.5. The MIV was calculated with all maximal tendon tensions being equal and the sum being constant at 1000N. We did not optimize the MIV for every design due to computational tractability considerations and because it is not crucial for the purposes of this study. (See below for some examples of optimized MIV).

We see that, in general, the best routings with 7 or 8 tendons have a substantially higher (unoptimized) MIV than the best routings with 5 or 6 tendons. However, routings with fewer tendons are not less able to produce low ESE values.

7.4.3 Optimizing MIV for 3 Specific Routings

To demonstrate that optimization of MIV is possible, we did optimize the MIV, in posture 2, for the three routings marked with large circles in Figure 7.5. Routing 1 is the one with the highest unoptimized MIV, and it has 8 tendons. Routing 2 was chosen as an N+1 design that had both low average ESE* and high MIV compared with other N+1 designs. Routing 3 was chosen as a reference point, having a mathematically even, symmetric moment arm matrix of a 2N design (the matrix values are only indicative of the sign of the moment arm and not the magnitude):

$$R_{\text{ROUTING } 3} = \begin{bmatrix} 1 & -1 & 1 & -1 & 1 & -1 & 1 & -1 \\ 0 & 0 & 1 & -1 & 1 & -1 & 1 & -1 \\ 0 & 0 & 0 & 0 & 1 & -1 & 1 & -1 \\ 0 & 0 & 0 & 0 & 0 & 0 & 1 & -1 \end{bmatrix}$$

The optimization was able to improve the MIV in posture 2 from 21.2N to 26.0N for Routing 1 (a 23% increase), from 8.68N to 15.6N for Routing 2 (an 80% increase), and from 10.0N to 18.0N for Routing 3 (an 80% increase). Figure 7.6 shows the routings, unoptimized feasible force sets, optimized feasible force sets, unoptimized endpoint stiffness ellipsoids (with all tendons having equal stiffnesses), and optimized endpoint stiffness ellipsoids. Two 3-D views are shown of the feasible force sets. The optimized tendon stiffness values shown are normalized so that the highest stiffness has a value of 1 (multiplying all the stiffnesses by a scalar does not affect the condition number).

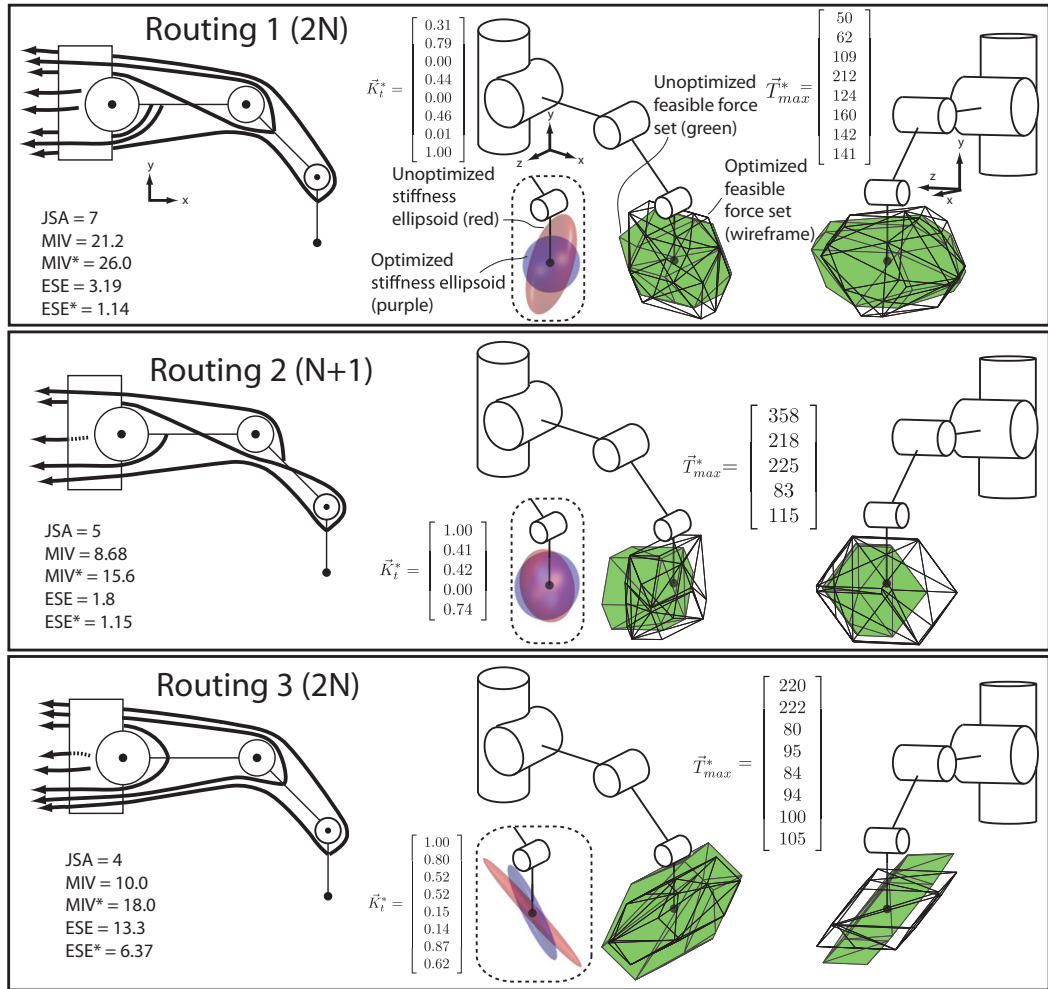


Figure 7.6: Illustration of 3 routings along with stiffness ellipsoids and feasible force sets. JSA: Joint stiffness adjustability. MIV: Maximal isotropic value before optimization, in N. MIV*: Maximal isotropic value after optimization, in N. ESE: Endpoint stiffness eccentricity before optimization. ESE*: Endpoint stiffness eccentricity after optimization. \vec{K}_t^* : tendon stiffnesses producing ESE*, normalized so that maximal stiffness is 1. \vec{T}_{max}^* : maximal tendon tensions producing MIV*, in N. Note: all results shown are for posture 2 only, and values correspond with the small triangles in Figure 7.5.

We see that routings 1 and 2 are able to produce very low ESE* values, while Routing 3 is only able to produce an ESE* of 6.37 (in posture 2). It can be noted that some of the optimized tendon stiffnesses are 0, which may only be realizable in practice with a direct drive DC motor actuator (in which case also the motor inertia would not necessarily allow for instantaneous extension of the tendon with zero resistance). However, we feel that this is not extremely important in our simulation results and general conclusions, since this analysis and optimization could easily be implemented with additional constraints (such as minimal and maximal values for tendon stiffnesses).

We can also observe in Routing 1 that the two tendons that only cross the first joint could be easily combined into one tendon in strength and stiffness, resulting in a routing with 7 tendons that has the exact same characteristics as the routing shown with 8 tendons.

7.5 Discussion

The main purpose of this study was to demonstrate the large effect of tendon routing, number, and properties on force-production and stiffness realization capabilities. We show that tendon routings with fewer than $2N$ tendons (which are necessarily asymmetric) can have high force-production capabilities as well as low eccentricity of endpoint stiffnesses.

Our optimization of the endpoint stiffness assumed that it is desirable to produce nearly-isotropic endpoint stiffness, as we assumed no knowledge about the task or potential obstacles to the fingertip. In some practical cases, it may be desirable to adjust the endpoint stiffness characteristics asymmetrically according to the task or situation (Wolf

& Hirzinger 2008) to be compliant in one direction and stiff in another. For example, if the task is to push a button, guide a rod, etc, then it may be beneficial to have high stiffness in the direction of force application but low stiffness in the directions perpendicular to the direction of force application. Any specific task requirements could easily be incorporated into an optimization routine.

For any practical application, the analyses used in this study would need to take into account the actuation system, and whether it incorporates non-linear or adjustable stiffnesses. The calculation of JSA and the optimization of ESE and MIV in this study assume that the tendon stiffnesses can be controlled independently of tendon tension and that the stiffnesses are linear.

Even if the actuation scheme used in a physical system does not allow for tendon stiffness control apart from tendon tension, the analyses used here could be used to guide the designation of spring constants for linear springs in series with actuators (i.e., some tendons could use stiff springs and others more compliant springs for a desired generic endpoint stiffness). Non-linear springs (Laurin-Kovitz et al. 1991) could be designed also with varying properties among tendons (e.g., with different elasticity constants and biases (Kobayashi et al. 1998)).

While the MIV was used as the fitness metric for the force-production capabilities, some hands or fingers may only need strong flexing force for use in grasping and the maximal extension force requirements may be low. In this case, the distribution of maximal tendon tensions could be adjusted or optimized according to grasping or other task requirements (Pollard & Gilbert 2002), possibly significantly reducing the total weight or volume of the actuation system when compared with only using identical actuators

for all tendons. Also, if non-linear stiffnesses are used in series with actuators, then the calculation of feasible force sets may need to be adjusted to account for the fact that pre-tension (possibly very high) will need to be applied to obtain a desired stiffness.

We only analyzed routings where the tendons routed around every joint that they passed (i.e., that the structure matrix is pseudo-triangular, as in (Lee & Tsai 1991)) and where all moment arms were equal in magnitude for a particular joint. We acknowledge that many of the routings that we analyzed may not be realizable in practice. Routings can be designed where tendons pass through the center of joints (Grebenstein et al. 2010), or where moment arms for different tendons on the same joint can have different magnitudes. Varying moment arms can add more potential flexibility to force-production and stiffness characteristics, while on the other hand, practical design considerations may preclude realization of some routings. However, the analyses could be run on a set of practical routings, spring stiffnesses, and maximal tendon tensions to guide in the design process.

While we have analyzed the passive control of stiffness and the bounds of force production in a finger, we have not considered directly the consequences of finger design to active control, which is of huge importance when constructing a useful system. In addition, a physical system subject to friction, estimation errors, actuator inconsistencies, and other factors may mandate certain design constraints that we have not analyzed.

Lastly, it is natural to compare our results to the number, routing and strength of the musculotendons of the human index finger. That index finger has 4 DOFs, and 7 tendons (6 tendons for the middle and ring fingers) (Valero-Cuevas et al. 1998, Valero-Cuevas, Anand, Saxena & Lipson 2007). Interestingly, that anatomy has fewer than $2N$

actuators and exhibits cross-over tendons such as those seen in Routings 1 and 2. In addition, muscles have different strengths and stiffnesses (muscles with longer tendons are naturally more compliant). Future work will apply this analysis to the anatomy of biological fingers.

In this study we have shown that there is a very wide range of force-production and stiffness capabilities of different tendon routings with varying numbers of tendons. We feel that the methods presented here could be used to guide in the design process for tendon-driven fingers, hands, or other manipulators, to maximize force production for various tasks, minimize the size and weight of the actuation system, and design tendon stiffness characteristics to realize various joint and endpoint stiffnesses. Furthermore, analysis of the human musculoskeletal system from the perspective of stiffness control and force-production simultaneously could elucidate the advantages and disadvantages of its anatomical features.

Acknowledgements

The authors gratefully acknowledge the help of M. Grebenstein in providing the kinematic parameters for the DLR index finger and the helpful discussions with J. Kutch, S. Schaal, M. Kurse, and P. Pastor.

Chapter 8

A Novel Computational Approach Helps Explain and Reconcile Conflicting Experimental Findings on the Neural Control of Arm Endpoint Stiffness

8.1 Abstract

Much debate has arisen from the experimental findings of limb impedance control during reaching movements, and particularly around the regulation of stiffness characteristics, and its relation to minimization of energy expenditure for a particular task. The two chief divergent experimental findings are i) that the CNS has very limited control over endpoint stiffness orientation and ii) that the CNS has almost complete control over endpoint stiffness ellipsoid orientation and eccentricity. In this study, we provide the results from novel theoretical analyses and computational experiments that offer explanations for both of these divergent findings, using only the passive stiffness characteristics of muscles, the

arm posture, and a standard 6-muscle planar arm model. There are three chief conclusions from this study. The first is that the mechanical ability to orient stiffness ellipsoids is heavily dependent on even small changes in posture, as well as moment arm ratios of the bi-articular muscles. The second is that neuromuscular synergies drastically reduce endpoint stiffness flexibility. The third is that in the complete absence of synergies, for any desired and realizable endpoint stiffness matrix, there exists a one-dimensional manifold in muscle activation space that can produce that stiffness (i.e., there exists stiffness redundancy). This provides a solution space which the CNS can then search to minimize energy consumption. In summary, this computational study helps to shed light on the differing conclusions of limb stiffness experiments, and its insights also can be used to design new experiments that can further elucidate the mechanisms of learning and plasticity present in the human motor system.

8.2 Introduction

Limb stiffness control by the central nervous system has been a subject of much study and debate over the past 3 decades. Numerous experiments and theoretical analyses have been conducted on the biomechanical and neuromuscular capabilities of the CNS to regulate endpoint stiffness of a limb (Burdet, Osu, Franklin, Milner & Kawato 2001, Burdet, Osu, Franklin, Yoshioka, Milner & Kawato 2000, Flash & Mussa-Ivaldi 1990, Franklin,

So, Kawato & Milner 2004, Franklin, Liaw, Milner, Osu, Burdet & Kawato 2007, Hogan 1984, Hogan 1985*a*, Hogan 1985*b*, Hu, Murray & Perreault 2011, Kadiallah, Liaw, Kawato, Franklin & Burdet n.d., McIntyre et al. 1996, Milner 2002, Mussa-Ivaldi, Hogan & Bizzi 1985, Perreault, Kirsch & Crago 2001, Perreault, Kirsch & Crago 2002, Stroeve 1999, Tee, Franklin, Kawato, Milner & Burdet n.d., Shin, Kim & Koike 2009, Osu & Gomi 1999, Gomi & Osu 1998, Darainy, Malfait, Gribble, Towhidkhah & Ostry 2004). These studies chiefly analyze the stiffness of the hand in reaching-like postures, as this is a simple case to analyze and experiments with this limb are standardized and fairly easy to perform.

In addition, there is extensive literature on the analysis and synthesis of stiffness in robotic manipulators (Ciblak & Lipkin 1994, Ciblak & Lipkin 1999, Huang & Schimmels 2000, Kobayashi et al. 1998, Hogan 1985*a*). The theoretical contributions and conclusions of these studies are unencumbered by extensive discussion of the mechanisms and limitations of motor control by the CNS, and hence can form a good foundation for analyzing the bounds of the biomechanical capabilities of the human musculoskeletal system. It can therefore aid in interpretation of human subjects experiments as well as stimulating creativity in novel experiments.

One set of experimental literature finds that the CNS can arbitrarily regulate the orientation and eccentricity of arm stiffness ellipsoids following training in order to perform a task more reliably and with less energetic expenditure than before training (Burdet et al. 2001, Franklin et al. 2004, Franklin et al. 2007, Kadiallah et al. n.d.). Another

set of experiments concludes that the CNS cannot arbitrarily regulate endpoint stiffness, and that it is only able to rotate the orientation of the stiffness ellipsoid around 30° (Gomi & Osu 1998, Darainy et al. 2004, Perreault et al. 2002). While these are very conflicting results, one large difference in the experimental conditions is that the former literature trains the arm and measures stiffness during reaching movements, while the latter literature measures stiffness without training in reaching movements.

Using the analyses developed in the robotics literature, we are able to resolve these divergent findings by computational experiments which offer explanations for both sets of results. Our novel formulation of the stiffness synthesis problem allows us to easily and efficiently analyze stiffness synthesis flexibility in the presence as well as absence of muscle synergies. We find that stiffness flexibility is very sensitive to small changes in arm posture and moment arm ratios, especially in certain portions of the workspace. Our experiments also emphasize the importance of bi-articular muscles in the human arm for stiffness control which has been highlighted extensively in the literature(Franklin et al. 2007, Flash & Mussa-Ivaldi 1990, Hogan 1985*a*, Hogan 1985*b*, Kobayashi et al. 1998). Moreover, our formulation reveals a one-dimensional manifold (which is a convex set) where a realizable stiffness can be attained in the absence of synergies. This can be called stiffness redundancy, and once the CNS solves the problem of tuning endpoint stiffness to its desired configuration, then it further faces the problem of energy minimization

within the constraints of the desired stiffness. This implies that conclusions about energy minimization due to changes in the stiffness ellipsoid should be used with caution.

8.3 Methods

8.3.1 Arm Model

We use a simplified planar arm model with 6 muscles similar to those that have been used in other theoretical and computational studies (Fagg, Sitkoff, Barto & Houk 1997, Flash & Mussa-Ivaldi 1990, Hogan 1985*b*, Milner 2002, Mussa-Ivaldi et al. 1985). It is shown in Figure 8.1a. We use workspace constraints identical to those used in (Hogan 1985*b*) to produce the workspace shown in Figure 8.1b. In the same figure, we illustrate that we use singular value decomposition (SVD) to transform the endpoint stiffness matrix (K_{end}) or the manipulator Jacobian (J) to an ellipse that represents the characteristics of either of these matrices (e.g., condition number, orientation, size, etc.).

8.3.2 Theoretical Formulation

We begin our formulation with the endpoint stiffness matrix, K_{end} , which relates the vector of differential endpoint displacements to differential endpoint forces:

$$\partial \vec{F} = K_{end} \partial \vec{x} \quad (8.1)$$

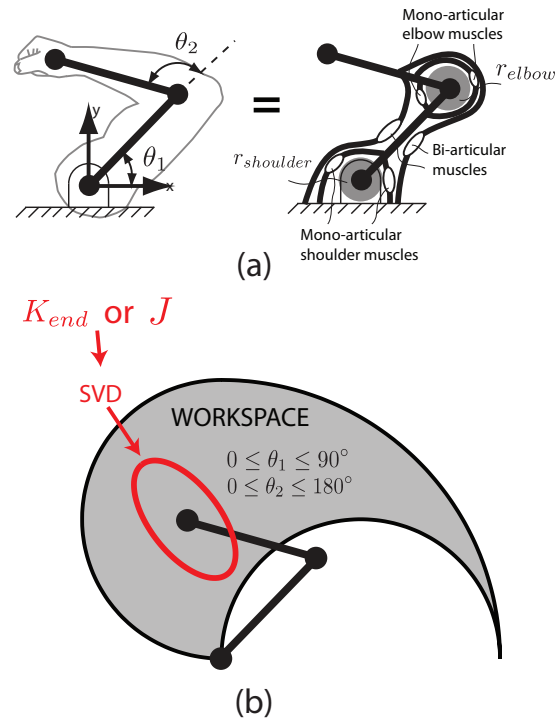


Figure 8.1: (a) Arm model. (b) Workspace of arm model. SVD used to transform endpoint stiffness matrix to a stiffness ellipse.

where $\partial\vec{F}$ is the endpoint force vector resulting from a displacement vector $\partial\vec{x}$. The joint stiffness matrix relates the vector of differential joint angle displacements to differential joint torques:

$$\partial\vec{\tau} = K_{joint}\partial\vec{\theta} \quad (8.2)$$

where $\partial\vec{\tau}$ is the joint torque vector resulting from a joint angle displacement vector $\partial\vec{\theta}$. The endpoint stiffness matrix is dependent on the joint stiffness matrix as well as the manipulator Jacobian J (which is posture dependent: a vector of joint angles $\vec{\theta}$ uniquely defines the posture):

$$\dot{\vec{x}} = J(\vec{\theta})\dot{\vec{\theta}} \quad (8.3)$$

where $\dot{\vec{x}}$ denotes the endpoint velocity vector and $\dot{\vec{\theta}}$ denotes the joint angle velocity vector.

The endpoint stiffness matrix, in the absence of an external tip force, is given by (Hogan 1985*b*):

$$K_{end} = J^{-T} K_{joint} J^{-1} \quad (8.4)$$

Furthermore, the joint stiffness matrix is given by (Hogan 1985*b*):

$$K_{joint} = R K_{tendon} R^T \quad (8.5)$$

where R is the moment arm matrix relating joint angle changes to tendon displacements, $\partial \vec{s}$:

$$\partial \vec{s} = R \partial \vec{\theta} \quad (8.6)$$

and K_{tendon} is the diagonal matrix of tendon stiffnesses, which is assumed to be a linearly related to muscle force (Cui, Perreault, Maas & Sandercock 2008):

$$K_{tendon} = \text{diag}(\vec{F}_{muscles}) \quad (8.7)$$

Combining Equations 8.4, 8.5, and 8.7, we get:

$$K_{end} = J^{-T} R(\text{diag}(\vec{F}_{muscles})) R^T J^{-1} \quad (8.8)$$

From the above equation, we can reformulate the endpoint stiffness matrix, the moment arm matrix, and the Jacobian in order to make the endpoint stiffness vector, \vec{K}_{end} a linear function of the muscle force vector $\vec{F}_{muscles}$. We show these reformulations in Figure 8.2. (•) denotes element-by-element multiplication, and R_i is the i^{th} row of R . The Jacobian

$$\begin{aligned}
K_{end} &= \begin{bmatrix} k_{11} & k_{12} \\ k_{21} & k_{22} \end{bmatrix} \rightarrow \vec{K}_{end} = \begin{bmatrix} k_{11} \\ k_{12} \\ k_{22} \end{bmatrix} \\
R &= \begin{bmatrix} \dots & R_1 & \dots \\ \dots & R_2 & \dots \\ \vdots & & \vdots \\ \dots & R_n & \dots \end{bmatrix} \rightarrow \tilde{R} = \begin{bmatrix} R_1 \bullet R_1 \\ R_1 \bullet R_2 \\ \vdots \\ R_1 \bullet R_n \\ R_2 \bullet R_2 \\ \vdots \\ R_2 \bullet R_n \\ \vdots \\ R_n \bullet R_n \end{bmatrix} \\
J^{-T} &= \begin{bmatrix} j_{11} & j_{12} \\ j_{21} & j_{22} \end{bmatrix} \rightarrow \tilde{J}^{-T} = \begin{bmatrix} j_{11}^2 & 2j_{11}j_{12} & j_{12}^2 \\ j_{11}j_{21} & j_{11}j_{22} + j_{12}j_{21} & j_{12}j_{22} \\ j_{21}^2 & 2j_{21}j_{22} & j_{22}^2 \end{bmatrix}
\end{aligned}$$

Figure 8.2: Endpoint stiffness variables reformulated. (\bullet) denotes element-by-element multiplication, and R_i is the i^{th} row of R .

reformulation is specific to the 2-link planar arm model, but similar expressions can be formulated for Jacobians of higher dimensions.

The endpoint stiffness and the moment arm matrix have been previously reformulated in this way (Kobayashi et al. 1998), but to the best of our knowledge, no study has ever reformulated the Jacobian in this way to allow for the following simple set of linear equations, which is equivalent to Equation 8.8:

$$\tilde{K}_{end} = \tilde{J}^{-T} \tilde{R} \vec{F}_{muscles} \quad (8.9)$$

8.3.3 Checking for Realizable Endpoint Stiffness Matrices

Given a desired endpoint stiffness condition number (the ratio of the length of the major axis of the ellipse to the length of the minor axis) and orientation (angle from the x-axis to the major axis of the ellipse), we can determine if the arm is able to realize this stiffness matrix given the constraints that the muscle forces are non-negative, the net joint torque vector is zero, and the endpoint stiffness vector corresponds to that which is desired. We can express this as follows:

if $\exists \vec{F}_{muscles}$ s.t.

$$\tilde{K}_{end,desired} = \tilde{J}^{-T} \tilde{R} \vec{F}_{muscles} \quad (8.10)$$

$$R\vec{F}_{muscles} = 0 \quad (8.11)$$

$$\vec{F}_{muscles} \geq 0 \quad (8.12)$$

Then if $\exists \vec{F}_{muscles}$ s.t. Equations 8.10, 8.11, and 8.12, $\tilde{K}_{end,desired}$ is realizable.

We would like to estimate the angular range of achievable endpoint stiffness ellipse orientations given the arm posture and a desired condition number. To this end, we fix the condition number and the posture, and then determine a set of desired endpoint

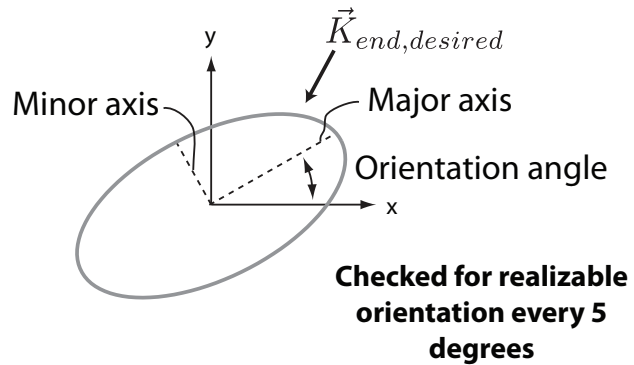


Figure 8.3: The endpoint stiffness ellipse as defined by the desired endpoint stiffness vector, corresponding to an orientation angle and a set condition number.

stiffness vectors \vec{K}_{end} , where each corresponds to a different ellipse orientation. We do this every 5° around the full range of orientations and then check the fraction of these orientations that are realizable. This is shown in Figure 8.3.

In our computational experiments, we formulated the realizability problem above as a constrained quadratic programming problem, with the optimization criteria being minimizing the sum of squares of the muscle forces. If the optimization found a solution, then the orientation (for that specific condition number and posture) is realizable.

An example of the fraction of realizable orientations for all postures in the workspace is shown in Figure 8.4.

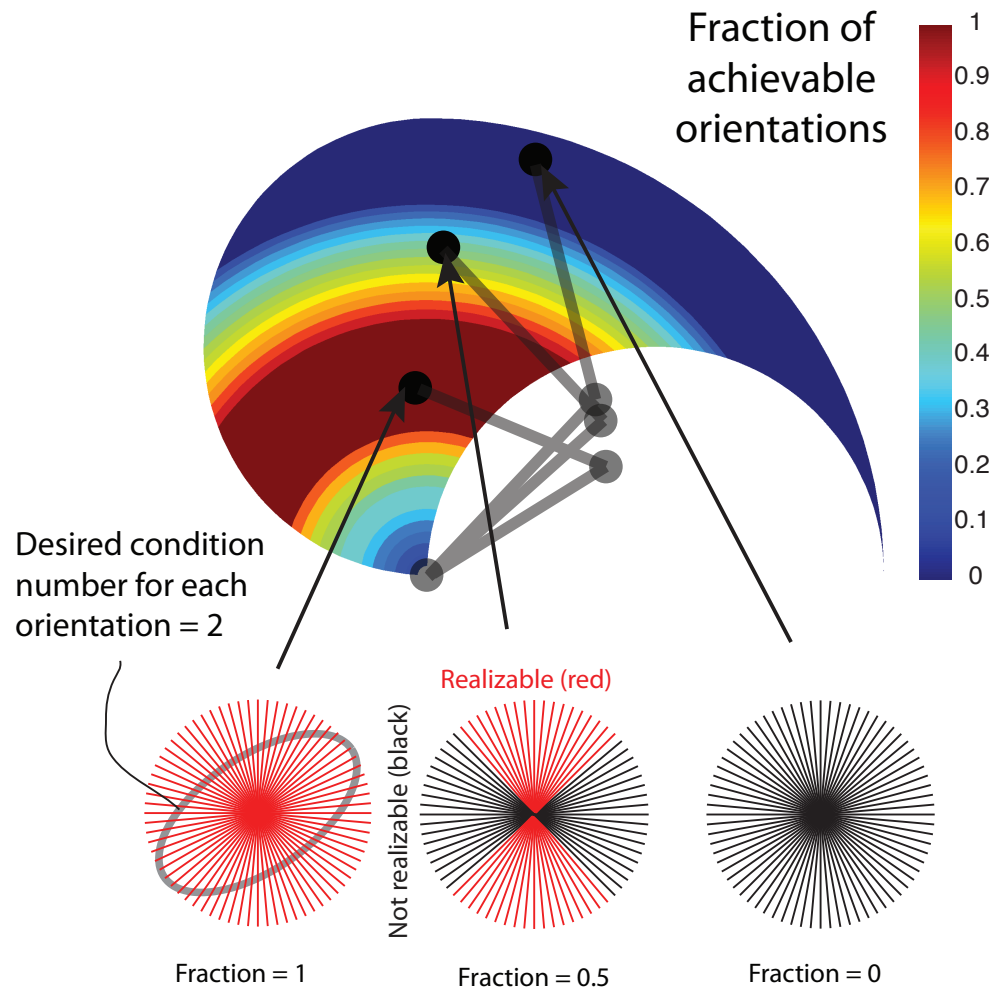


Figure 8.4: Example of realizable orientations in various postures for a condition number of 2. Red lines indicate that the orientation of the major axis in that position is realizable, and black lines indicate that the orientation is not realizable.

8.3.4 Varying Moment Arms and Synergies

We did this realizability experiment with all muscles having equal moment arms and also with varying ratios of elbow to shoulder moment arms. In addition, we also performed the experiment with synergies as reported from an EMG study (Osu & Gomi 1999). This synergy basically couples the bi-articular muscles with the mono-articular elbow muscles, and quantitatively it was found that the elbow stiffness from co-contraction of the bi-articular muscles was approximately one half of the elbow stiffness from the mono-articular elbow muscles. The mono-articular shoulder muscles were not found to have synergies with the bi-articular muscles.

In the presence of these synergies, then only one parameter can be varied to change the orientation and condition number of the endpoint stiffness ellipse: the ratio of elbow muscle co-contraction (which includes the synergistic bi-articular muscles' co-contraction) to shoulder muscle co-contraction. Increasing both co-contractions simultaneously only increases the size of the ellipse but not the condition number or orientation. As we will see in the results, none of the desired endpoint stiffness vectors can be achieved because there are two parameters that must be satisfied: the condition number and orientation. In the presence of synergies, as just described, there is only one free parameter that can be varied and therefore changing orientation independently of condition number is impossible.

Due to this inflexibility, we use another method to analyze the effect synergies have on realizable endpoint orientations, *without considering the specific condition number*: we vary the ratio of shoulder stiffness to elbow stiffness over a range of 2 orders of magnitude (1/10 to 10) and see how much the orientation of the ellipse is able to change.

8.3.5 Exploring Energy Expenditure Within the Stiffness Redundancy Solution Space

The constraints in the realizability tests have 5 equality constraints (Equations 8.10 and 8.11). Since there are 6 muscles, if there is any solution which satisfies the non-negative constraint (Equation 8.12), in general there will be a one-dimensional manifold (or nullspace) of solutions for the desired endpoint stiffness vector in the 6-dimensional muscle force space. Vertex enumeration algorithms can be used to determine the vertices of this one-dimensional manifold (which is a convex set). However, we are most interested in the maximal and minimal energy expenditures within this space. Therefore, we can use opposite quadratic programming optimization criteria to determine both of these energy expenditures. For the minimal energy expenditure, as already described, our optimization criteria is to minimize the sum of squares of the muscle forces. For maximal energy expenditure, our optimization criteria is to maximize the sum of squares of the muscle forces. From these numbers we can then determine the maximal amount of energy reduction that is possible. For example, if the maximal energy expenditure is 10

(normalized) and the minimal energy expenditure is 7, then there is a maximum of 30% reduction in energy possible.

Our rationale for quantifying these ratios is that for an observed stiffness ellipsoid in human subjects experiments, we want to know if we can infer that the central nervous system is minimizing energy expenditure. If there is a large possible range of energies expended for the exact same endpoint stiffness ellipse, then additional experimental means such as EMG must be used to make precise and accurate conclusions about energy minimization.

8.4 Results

8.4.1 Realizable Fraction of Endpoint Stiffness Ellipses

Figure 8.5 shows the results of various condition numbers, synergies, and moment arm ratios on the fraction of realizable orientations.

Our computational results for condition number 1, in the equal moment arms, no synergies case, is identical to the theoretical result determined by (Hogan 1985*b*). We can make several observations from Figure 8.5. First, posture has a huge effect on the range of realizable orientations. Second, the ratio of shoulder to elbow moment arms also has a large effect on realizable orientations. Third, as discussed before, synergies prevent any orientation from being obtained given a set condition number because that requires

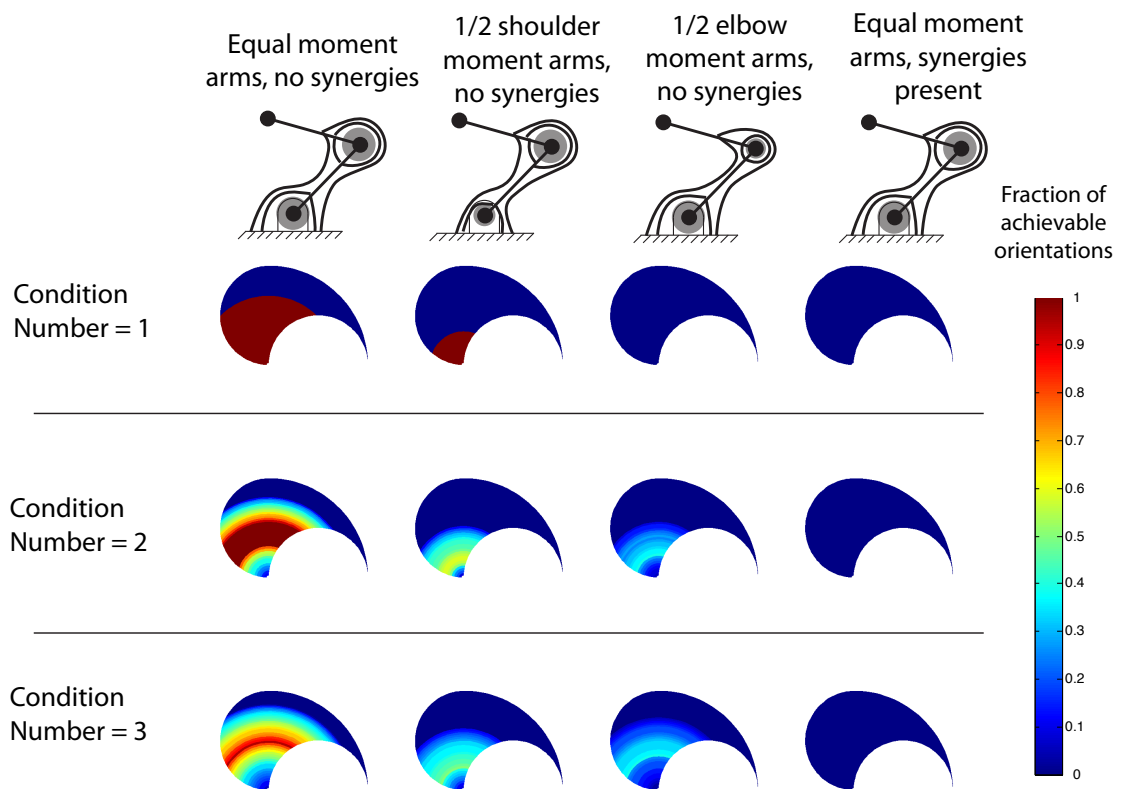


Figure 8.5: Fraction of realizable orientations given various modeled conditions.

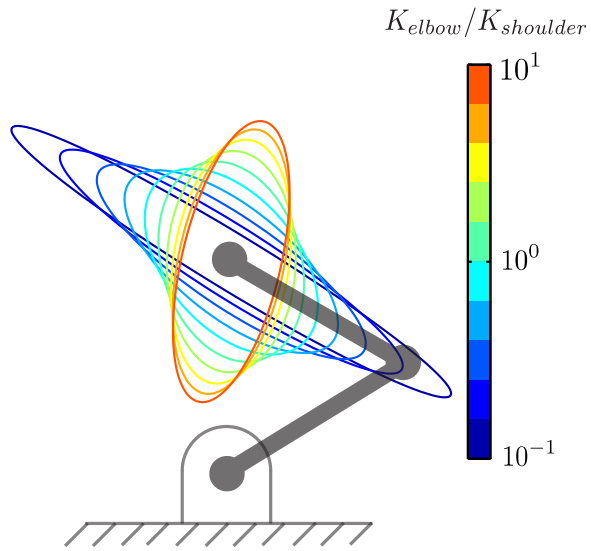


Figure 8.6: Range of orientations in the presence of synergies.

2 free parameters, while in the synergies case, there is only one free parameter. Fourth, in general, a higher condition number results in less orientation range realizability.

8.4.2 Realizable Orientations in the Presence of Synergies

Figure 8.6 shows the orientations achieved by varying the ratio of shoulder to elbow stiffness from 1/10 to 10, with the arm endpoint being in normalized x-y position (0,1): each link of the arm has length of 1. The volumes of the ellipses are normalized to be equal to each other, allowing observation of the orientation and condition number of the ellipse.

The range of orientations is approximately 70° , which represents a realizable fraction of orientations of about 0.39. This is a much more limited range than the first column of plots shown in Figure 8.5. In this posture, for all 3 condition numbers, the fraction of realizable orientations is 1 (all orientations are achievable) in the absence of synergies. In addition, we see that as the orientation of the ellipse in Figure 8.6 changes, the condition number of the ellipse changes. The range of physically-realizable ratios of elbow to shoulder co-contraction are likely much less extreme than two orders of magnitude, which would result in an even smaller range of possible ellipse orientations.

8.4.3 Energy Expenditure Ranges

The maximal ratios between maximal and minimal energy expenditure given a condition number and posture for *any orientation* produced the results shown in Figure 8.7. The maximum possible energy reduction at a given posture is shown. That is, for a fraction of 0.5, the maximal energy expended for a certain orientation was 2 times that of the minimal energy expended. It can be seen that the maximum possible energy reduction for any posture for these condition numbers is around 0.5 (in some very specific postures). In much of the workspace, very little energy reduction is possible.

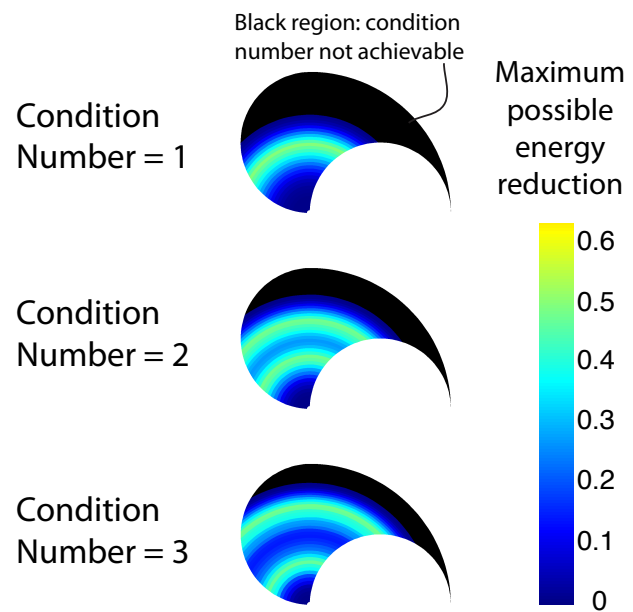


Figure 8.7: Maximal possible energy reduction for any orientation given the condition number and posture.

8.5 Discussion

We have explored the effects of posture, synergies, and moment arm ratios on the achievable endpoint stiffness ellipses for the human arm as well as energy minimization possibilities. Our novel formulation allows us to do this with ease and efficiency. We see that the range of achievable orientations is very sensitive to posture, and that synergies drastically limit the ability to orient the ellipse as well as control the condition number (since it cannot be controlled independently of orientation). In addition, significant energy minimization is possible once certain achievable endpoint ellipses have been realized by a co-contraction pattern in the solution space.

We would like to point out an important difference in our formulation compared with other modeling studies for arm stiffness (Franklin et al. 2007, Hogan 1985*b*, Hogan 1985*a*, McIntyre et al. 1996, Flash & Mussa-Ivaldi 1990, Perreault et al. 2002). The general form of the joint stiffness matrix in these studies is (for all equal moment arms):

$$K_{joint} = \begin{bmatrix} K_s + K_b & K_b \\ K_b & K_e + K_b \end{bmatrix} \quad (8.13)$$

where K_s is the shoulder stiffness provided by co-contraction of the mono-articular shoulder muscles, K_b is the bi-articular joint stiffness provided by co-contraction of bi-articular muscles, and K_e is the elbow stiffness provided by co-contraction of mono-articular elbow

muscles. This implies 3 equality constraints, one for each pair of muscles. This is one more constraint than the condition of zero endpoint force (i.e., $R\vec{F}_{muscles} = 0$, which is two equalities). If these 3 equality constraints are in place, then in addition to the 3 provided by $\tilde{K}_{end,desired} = \tilde{J}^{-T}\tilde{R}\vec{F}_{muscles}$, we have a total of 6 equality constraints. If a solution exists given these constraints, it is unique (in general), since there are 6 muscles. Therefore, no energy minimization is possible if these 3 “synergies” are present.

This study only looks at the mechanical capabilities of the arm model given the passive stiffness properties of muscles, which were assumed to be linear and proportional to muscle force. This model does not take into account active reflex pathways (or feedback pathways), which clearly can be used to minimize energy further depending on the frequency content of a perturbation or motor noise during a task. It has been suggested (Hu et al. 2011) that some studies involving endpoint stiffness analysis may incorporate active reflex contributions (Burdet et al. 2001, Franklin et al. 2007, Darainy et al. 2004). If only passive stiffness properties are used and there is no net force at the endpoint, then the endpoint stiffness matrix is symmetric. It has been noted that any non-symmetric component of endpoint stiffness “can only be due to heteronymous inter-muscular feedback” (Hogan 1985*b*). However, our study is still able to reconcile conflicting findings even if only passive stiffness is considered.

Our results suggest ways in which future arm stiffness experiments may be conducted in order to analyze stiffness synthesis strategies used by the CNS such as synergies,

energy minimization, posture adjustment, and active reflex pathways. Reaching experiments could test stiffness ellipsoids in various postures during the reaching movement, since stiffness ellipsoid orientation flexibility is very sensitive to small changes in posture. Findings that conflict with the results of this study could be studied in more detail as this would suggest significant feedback pathways that were developed as a result of motor learning and neural plasticity.

Acknowledgements

The authors gratefully acknowledge the useful comments from Jason Kutch.

Chapter 9

Optimization of Tendon Topology for Robotic Fingers: Prediction and Implementation

9.1 Abstract

Tendon-driven mechanisms in general, and tendon-driven fingers in particular, are an important class of bio-inspired mechatronic systems. However, their mechanical complexity and high-dimensional design space has not been fully harnessed to optimize their performance, control, and construction. In this study we describe a novel, systematic approach to analyze and optimize the routing of tendons for force-production capabilities of a reconfigurable 3D tendon-driven finger. Our results show that these capabilities could be increased by up to 277% by rerouting tendons, and up to 82% by changing specific pulley sizes for specific routings. Experimental results for 6 implemented tendon routings correlated very highly with theoretical predictions with an R^2 value of 0.987,

and the average effect of unmodeled friction decreased performance an average of 12%.

We not only show that, as expected, functional performance can be highly sensitive to tendon routing and pulley size, but also that informed design of fingers with fewer tendons can exceed the performance of some fingers with more tendons. This now enables the systematic simplification and/or optimization of the design and construction of novel robotic fingers. Lastly, this design and analysis approach can be used to model complex anatomical systems such as the human hand to understand it in detail.

9.2 Introduction

Bio-inspired robotic hands employ multiple robotic fingers for dexterous grasping and manipulation tasks (Jacobsen et al. 1986, Salisbury & Craig 1982, Shadow Robot Company n.d., Grebenstein et al. n.d., Ambrose et al. 2000, Jau 1995, Massa et al. 2002, Lin & Huang 1996, Kawasaki et al. 2002, Namiki et al. 2003, Yamano & Maeno 2005, Gaiser et al. 2008). Bio-inspiration can refer to their tendon-driven nature, but also the asymmetry of the routings, the variation in moment arm sizes, and the non-uniform distribution of maximal tendon tensions. Robotic finger kinematics may be anthropomorphic or they may be less complex to simplify the construction and control of the fingers. Moreover, two fundamental classes of actuation are typically used: i) those that use remote actuation (e.g., motors outside the fingers which actuate tendons, cables, or gears) and ii) those

that use internal actuation (e.g., motors inside the fingers). Tendon-driven limbs and fingers are ubiquitous in vertebrates, and such bio-inspired tendon-driven actuation has proven engineering design advantages such as light weight, low inertia, small size, backdrivability, and design flexibility (Pons et al. 1999). However, the mechanical complexity of tendon-driven system (e.g., the large number of design parameters) has precluded the development of modeling, design, and analysis tools to optimize their performance, control, and construction. In this paper, we analyze, optimize, and test alternative implementations of a 3D tendon-driven robotic finger. We validate this approach with physical hardware implementations from the functional perspective of maximizing the set of feasible endpoint static forces.

Many considerations go into the design of robotic fingers and hands, such as force and velocity production, control, ease of construction, design simplicity, and cost. Adequate force-production capabilities are a necessary element of the multidimensional design puzzle: according to Firmani, “The knowledge of maximum twist and wrench capabilities is an important tool for achieving the optimum design of manipulators” (Firmani et al. 2008). In fact, if a finger cannot produce sufficient endpoint force while meeting other critical design requirements such as size and number of motors (for example in space, hazardous or surgical applications), then the mechatronic system is useless regardless of the attributes of the controller or ease of manufacturing. Therefore, as a demonstration of our

novel modeling, analysis and optimization approach we concentrates on the kinetostatic (endpoint force-production) capabilities for robotic fingers.

Several studies have analyzed the kinetostatic performance of tendon-driven and torque-driven manipulators (Bouchard et al. n.d., Chiacchio et al. 1997, Firmani et al. 2008, Finotello et al. 1998, Gouttefarde & Krut 2010, Zibil et al. 2007, Tsai 1995, Lee & Tsai 1991, Lee 1991) (determining the kinetostatic capabilities given design parameters), and several others have addressed their optimization or synthesis (specifying the design parameters given desired capabilities) (Fu & Pollard 2006, Chen et al. 1999, Ou & Tsai 1993, Ou & Tsai 1996, Sheu et al. 2009, Angeles 2004, Aref et al. 2009, Chablat & Angeles 2002, Khan & Angeles 2006). These studies are based on mathematical theory. The fabrication of robotic fingers has been widely accomplished for robotic hands (Jacobsen et al. 1986, Salisbury & Craig 1982, Shadow Robot Company n.d., Grebenstein et al. n.d., Ambrose et al. 2000, Jau 1995, Massa et al. 2002, Lin & Huang 1996, Kawasaki et al. 2002, Namiki et al. 2003, Yamano & Maeno 2005, Gaiser et al. 2008). Experimental testing of kinetostatic performance can be found in the biomechanics literature (Kuxhaus et al. 2005, Valero-Cuevas et al. 1998), but these do not implement a system whose parameters can be altered. We combine these three areas of *theory, fabrication, and testing* to optimize and validate hardware implementations of alternative robotic finger designs.

9.3 Finger Construction

We had several design requirements when designing a reconfigurable robotic finger as a test bed for analysis, optimization, and testing. They were

1. Ability to arbitrarily change tendon routing (i.e., the joints each tendon crosses, and whether they produce positive or negative torque at each joint).
2. Ability to vary pulley sizes (i.e., moment arms of the tendons)
3. Low friction
4. Sufficient and well arranged degrees-of-freedom (DOFs) to allow three-dimensional endpoint motion and force production
5. Robust, durable, rigid

We designed the finger in SolidWorks 2010 (Dassault Systèmes), as shown in Figure 9.1. The actual reconfigurable finger is also shown. It was constructed with one abduction DOF and two flexion-extension DOFs. The primary materials were aluminum (for the links and terminating pulleys), turcite (for the spacers and rotating pulleys), and ball bearings with extended inner rings (mounted on all pulleys and link axes). All of the pulleys were custom-machined and two sizes were constructed for reconfigurability: a radius of 8.0mm for the large pulleys and 4.4mm for the small pulley, as shown in

Figure 9.2. There were multiple pulleys that had to be added between the axes to ensure reconfigurability of the tendon routing (i.e., that each tendon could rout on either side of every joint and no bowstringing of the tendons would occur).

The selection of link lengths and pulley sizes was otherwise fairly arbitrary, and since our study did not involve optimization of incremental changes in these parameters (except the 2 pulley sizes), we simply constructed it to have reasonable size that could be fabricated and tested.

9.4 Methods

After construction of the finger with the desired capabilities, we were then able to analyze and optimize tendon routing and pulley sizes based on the actual kinematics and reconfiguration options of the finger.

9.4.1 Force polytope analysis

Quantification of the force-production capabilities of a robotic finger (or manipulator) can be accomplished by determination of the feasible force set (or force polytope) of the finger. This convex set encloses all feasible forces that the fingertip can exert given kinematic parameters, tendon routing and pulley sizes, and maximal tendon tensions. A quality metric that can be assigned to this set is known as the maximal isotropic value

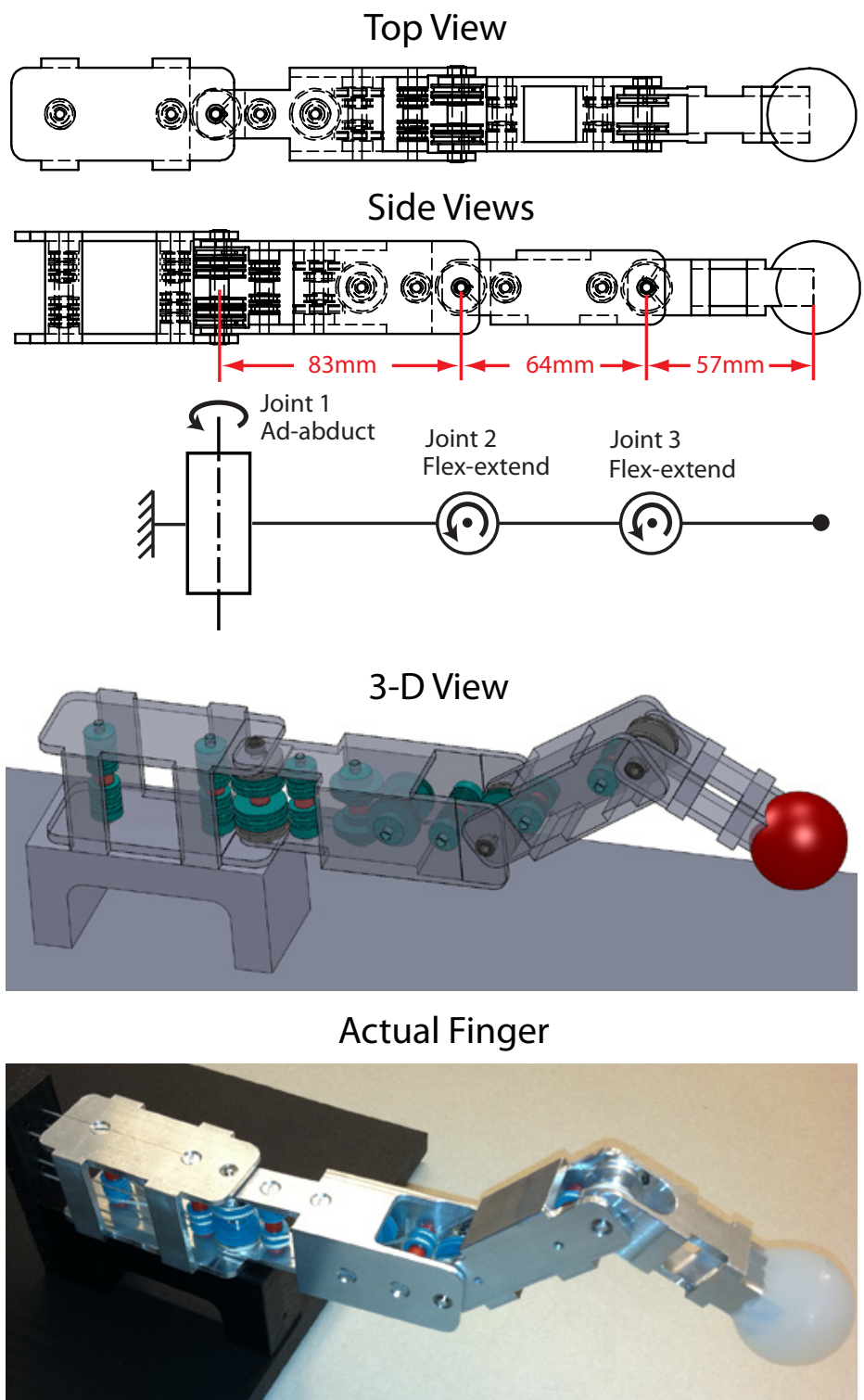


Figure 9.1: 2-D and 3-D views of finger model in SolidWorks, and the actual finger.

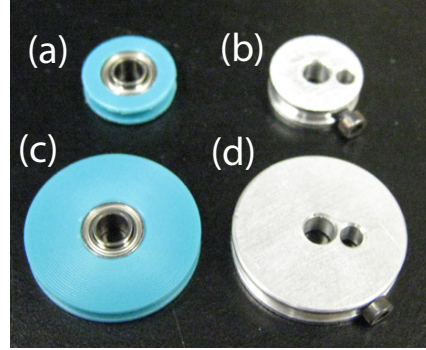


Figure 9.2: Pulleys used in finger design. (a) Turcite rotating small pulley. (b) Aluminum terminating small pulley. (c) Turcite rotating large pulley. (d) Aluminum terminating large pulley.

(MIV) (Finotello et al. 1998). Since we are not assuming any specific task that this finger must perform, then we chose to use this metric. We could have used any other metric instead of the MIV. Further comments can be found in the discussion section. The MIV is the radius of the largest ball, centered at the origin, that the feasible force set can contain, as illustrated in Figure 9.3 for a 2-D feasible force set. A finger can exert at least that many units of force in any direction.

We can use an activation vector, \vec{a} , to represent the degree to which a tendon is activated. Each element of \vec{a} ranges between 0 (no activation, zero force) and 1 (full activation, maximal force). Further discussion may be found in (Valero-Cuevas 2005). If we define F_0 as a diagonal matrix of maximal tendon tensions, R as the moment arm matrix (or structure matrix) relating tendon tensions to joint torques, and J as the posture-dependent Jacobian relating joint velocities to fingertip velocities, then we can

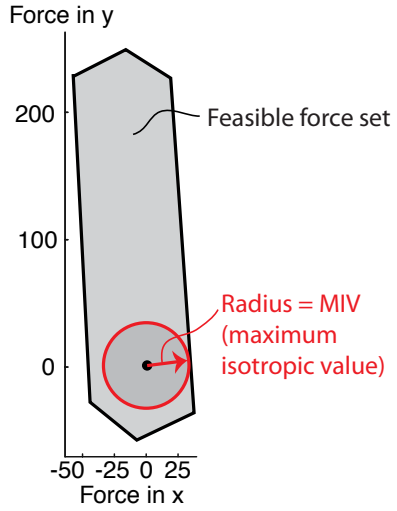


Figure 9.3: Illustration of calculation of MIV (maximum isotropic value) from feasible force set.

get the fingertip force vector \vec{f} from tendon activations (Valero-Cuevas et al. 1998) if the Jacobian is square and invertible:

$$\vec{f} = J^{-T} R F_0 \vec{a} = A \vec{a} \quad (9.1)$$

For a given fixed finger posture, the J^{-T} , R , and F_0 matrices can be grouped into a linear mapping from activations into fingertip force, which we call an action matrix A (Valero-Cuevas et al. 1998, Valero-Cuevas 2005). Each column of A represents the force vector each tendon produces at the fingertip in that posture if fully activated. The collection of all such forces (i.e., all columns of matrix A) forms a set of output force

basis vectors. Linearity of this mapping holds true for static forces because the Jacobian and moment arms remain constant. The Minkowski sum of these basis vectors forms the feasible force set of the fingertip, and can be computed by taking the convex hull of the points generated by mapping each vertex of the activation hypercube (i.e., each vertex of the unit hypercube in the positive orthant) to fingertip wrench space via the action matrix A (Valero-Cuevas et al. 1998).

There are two ways to describe a convex hull: i) a set of vertices and ii) a set of linear inequalities. Vertex enumeration methodologies can calculate one description given the other. The Qhull software package uses the Quickhull algorithm (Barber et al. 1996) and is used to perform the MIV calculations in this study. Other vertex enumeration algorithms that can perform these calculations easily include CDD (Fukuda & Prodon 1996) and LRS (Avis 2000).

The description involving a set of linear inequalities (similar to a linear programming inequality constraint formulation) takes the form

$$Ax \leq b \quad (9.2)$$

where A is a matrix of constants defining the inequalities, x is a vector of variables of length d , where d is the dimensionality of the convex hull, and b is a vector of constants. If we denote A_i as the i^{th} row of A , then the linear inequality $A_i x \leq b_i$ defines a halfspace,

which also defines a facet of the convex hull. The perpendicular (i.e., shortest) Euclidean distance (or offset) of this facet from the origin, in general, will be given by

$$\frac{b_i}{\|A_i\|_2} \quad (9.3)$$

The Qhull output, however, automatically sets each $\|A_i\|_2$ equal to 1, so the i^{th} offset from the origin is simply the signed constant b_i . Calculation of the MIV in this study involves simply finding the minimum of b corresponding to the feasible force set.

For our finger, the Jacobian is a 3×3 matrix which is square and invertible in our experimental postures, R is a $3 \times \ell$ matrix (ℓ is the number of tendons, which is 4, 5, or 6), and F_0 is an $\ell \times \ell$ diagonal matrix of maximal tendon tensions.

9.4.2 Evaluating tendon routings

The construction of the finger allowed for various moment arm matrices to be implemented which had 4, 5, or 6 tendons. These designs are known as N+1, N+2, and 2N designs, where N is the degrees of freedom of the finger. We enumerated all possible moment arm matrices beginning with the “base” matrices shown in Figure 9.4. The N+2a and N+2b designs differ only in that the second tendon terminates at the first joint in the N+2a designs and at the second joint in the N+2b designs. We replaced each ‘#’ with either a 1 or -1 (in accordance with the sign of the moment exerted on a joint when the

corresponding tendon is under tension; see Figure 9.1 for definition of joint axes) in a full combinatoric search and then checked the controllability (i.e., that all of the joints could be actuated independently in torque and motion) conditions as described in (Lee & Tsai 1991). We then calculated the MIV for these routings using the large pulleys in the main posture: 0° at joint 1, -45° at joint 2, and -45° at joint 3, as shown in Figure 9.5. To make comparisons feasible across finger designs with different number of tendons, we used a uniform maximal tendon tension distribution, with the sum being constrained¹ to 60N (i.e., for designs with 4, 5, and 6 tendons, the maximal tensions were 15N, 12N, and 10N, respectively). We found that many of the admissible routings produced the exact same MIVs and feasible force set volumes, likely corresponding with structurally isomorphic routings (Lee & Tsai 1991). The number of routings that produced unique MIVs was a very small subset of the admissible routings, as can be seen from the numbers in Figure 9.4. In cases of optimization of a more complex finger or manipulator where the number of unique MIVs may be orders of magnitude higher, methods for selection of a subset for further optimization such as in (Taguchi, Konishi & American Supplier 1987) may be used.

¹The sum of maximal tendon tensions being equal is an important constraint due to the size, weight, and motor torque (and therefore tendon tension) limitations inherent in dexterous hands. For example, the torque capacity of motors is roughly proportional to motor weight, and minimization of weight was an important consideration in the design of the DLR Hand II (Butterfa et al. 2001). In addition, the maximal force production capabilities of McKibben-style muscles are roughly proportional to cross-sectional area (Pollard & Gilbert 2002). Since the actuators typically will be located in the forearm, then the total cross-sectional area will be limited to the forearm cross-sectional area. In this study, for simplicity and without affecting the generalizability of our approach or results, we do not consider alternative constraints on the actuation system (e.g., electrical current capacity, tendon velocities, etc).

<p>N+1 design: 24 admissible, 3 unique</p> $R = \begin{bmatrix} \# & \# & \# & \# \\ 0 & \# & \# & \# \\ 0 & 0 & \# & \# \end{bmatrix}$	<p>N+2a design: 88 admissible, 6 unique</p> $R = \begin{bmatrix} \# & \# & \# & \# & \# \\ 0 & 0 & \# & \# & \# \\ 0 & 0 & 0 & \# & \# \end{bmatrix}$
<p>N+2b design: 296 admissible, 11 unique</p> $R = \begin{bmatrix} \# & \# & \# & \# & \# & \# \\ 0 & \# & \# & \# & \# & \# \\ 0 & 0 & 0 & \# & \# & \# \end{bmatrix}$	<p>2N design: 872 admissible, 20 unique</p> $R = \begin{bmatrix} \# & \# & \# & \# & \# & \# \\ 0 & 0 & \# & \# & \# & \# \\ 0 & 0 & 0 & 0 & \# & \# \end{bmatrix}$

Figure 9.4: Base moment arm matrices used when finding admissible and unique tendon routings.

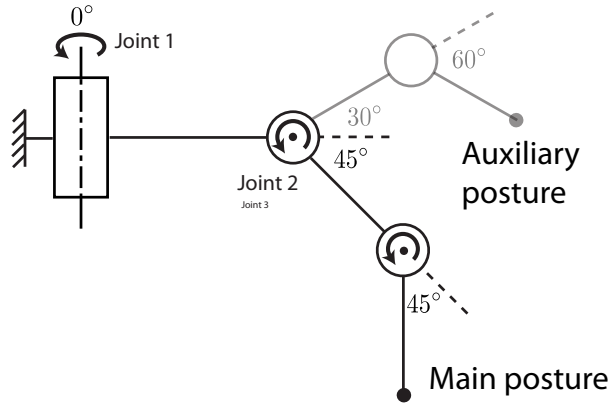


Figure 9.5: Finger posture used in computations and experimental testing.

The total number of routings producing distinct feasible force sets² was 40. For each of those routings, we calculated the MIV for all combinations of large and small pulleys. For example, the N+1 design has 9 moment arm values. Therefore, there are 2^9 combinations of large and small pulleys for that case. Taking the combination with the highest MIV for each routing gave 40 moment-arm-optimized routings. Therefore, we had 40 unoptimized routings and 40 optimized routings. Out of these 80, we chose 6 different routings to test experimentally in a fashion that permitted testing of a large range of MIVs, and included the design with the highest predicted MIV. Otherwise the selection was arbitrary.

9.4.3 Experimental testing of tendon routings

For each of the tendon routings tested, we first arranged the pulleys and strings (0.4mm braided polyester twine) to match the desired configuration. We then mounted the finger onto a base that was part of a motor array system as shown in Figure 9.6. The DC motors were coupled to capstans on which the string wound. Each string was then routed around pulleys that were attached to load cells (Interface SML 25, Scottsdale, AZ) which provided force measurements for the closed-loop controller implemented in Realtime LabView. The endpoint of the finger was fixed to a custom made gimbal which constrained translational

²Due to the nature of our full combinatoric search, moment arm matrices that produced mirrored feasible force sets about a plane passing through the origin (which would have the same MIV) were discarded and also those moment arm matrices that were produced by a rearrangement of the columns. For example, in Figure 9.4, interchanging columns 5 and 6 does not change the feasible force set, it only reverses the “numbering” of the tendons. But in the full combinatoric search, both of these numberings would be different matrices producing identical feasible force sets.

motion but not rotational motion (we did not want the fingertip to be over-constrained).

The gimbal was attached to a 6-axis load cell (JR3, Woodland, CA). The sampling rate and control loop frequency were both 100Hz.

A small pretension of 1N was applied to each string to remove slack and prevent it from falling off of the pulleys. Then each vertex of the activation hypercube (as described in the previous section) was applied to the strings (in addition to the pretension) in ramp-up, hold, and ramp-down phases to find the feasible force set (Kutch & Valero-Cuevas 2011).

As in prior work, (Kutch & Valero-Cuevas 2011), vertices of this experimental feasible force set were determined from the hold phases and then used to find the MIV using Qhull as described earlier. The experimental MIV could then be compared with the theoretical MIV (from computational results).

To compare the shapes of the experimental and theoretical feasible force sets, we first normalized the volume of the experimental feasible force set to make it equal to the volume of the theoretical feasible force set. We then calculated the mean Euclidean distance of each vertex from the theoretical feasible force set from the corresponding vertex in the experimental feasible force set. We did this because there was always friction loss in the experiment³. In addition, we calculated the average angle between the

³Take an extreme case in which friction loss was 50% exactly for every tendon. The theoretical feasible force set is a unit cube. While the shape of the experimental feasible force set would be also an exact cube, it would be 50% contracted in every direction and therefore the corresponding vertices would be far from each other. If we normalized the volume, the corresponding vertices would be in the same location, and the mean distance (in shape similarity) would be zero.

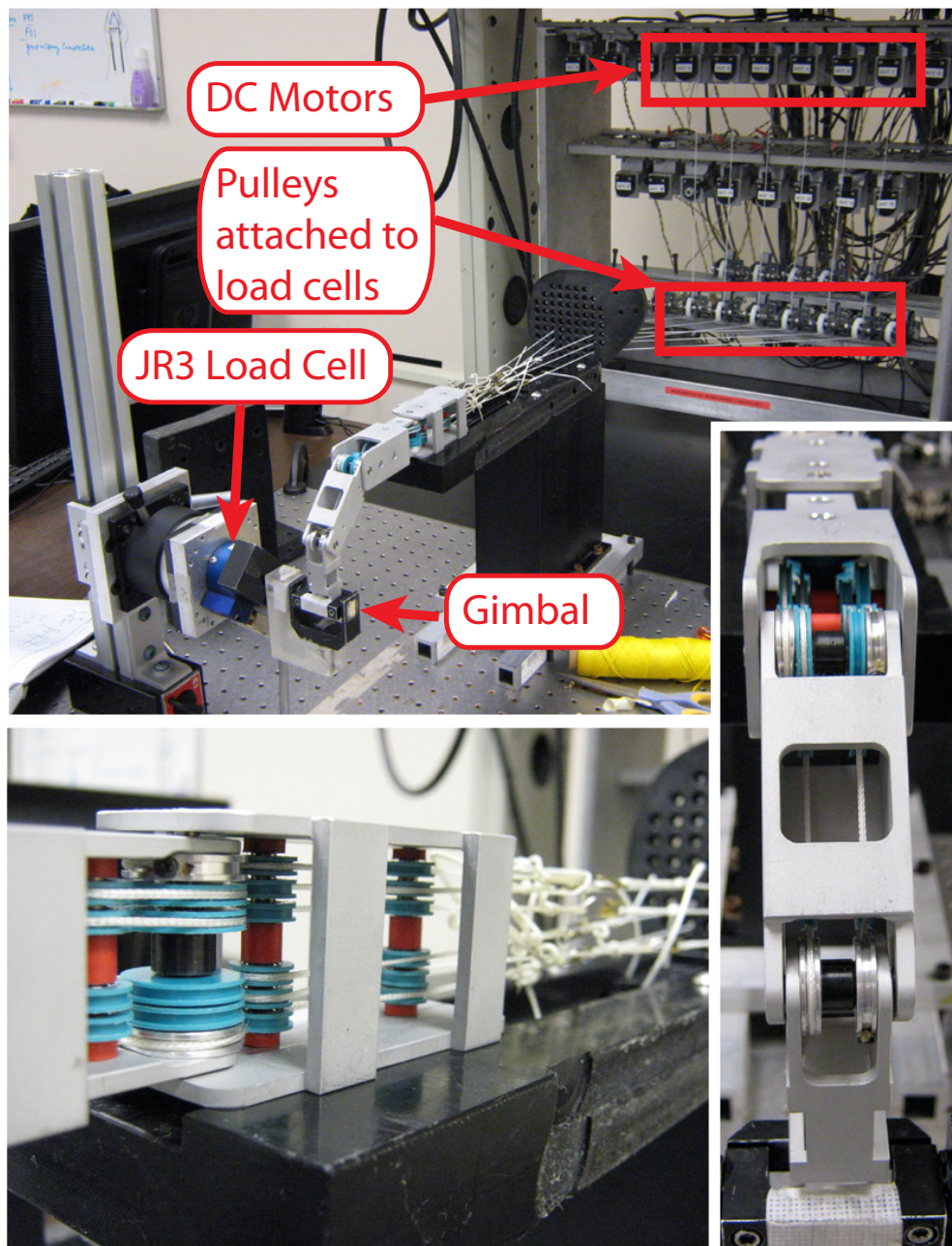


Figure 9.6: Experimental system for feasible force set testing.

two vectors (starting and the origin and ending at the corresponding vertex) formed from corresponding vertices.

We tested the finger in the main posture (for which we optimized MIV) and an auxiliary posture (to validate the predictions more fully). These postures are shown in Figure 9.5. For each design and posture, we did three repetitions of tests. Since there were 6 designs, 2 postures, and 3 repetitions, we conducted a total of 36 tests.

9.5 Results

9.5.1 Calculating maximum isotropic values

The 40 unique unoptimized and 40 unique optimized routings produced the MIVs shown in Figures 9.7a and b. Optimization of the pulley sizes increased the average MIV from 0.60N to 0.78N, a 30% increase as shown in Figure 9.7a, and the maximum increase for a routing by this optimization was 82%. It is interesting to note that this force-production capability increase is achieved by simply decreasing specific pulley sizes in an informed manner. We can see from Figure 9.7b that designs with 4 tendons could not produce MIVs higher than the best designs with 5 or 6 tendons. However, the best design with 4 tendons did have a higher MIV than many alternative routings that had more tendons. In addition, the maximal increase from only rerouting tendons (no pulley size optimization)

was 277% (i.e., the increase from the worst admissible routing to the best admissible routing for a given number of tendons).

9.5.2 Theoretical predictions vs. experimental results

The experimental results and the routings tested are shown in Figure 9.8. The data points shown in Figure 9.8b are averages of the three test repetitions in both the main posture and the auxiliary posture for each of the designs. The average standard deviation from the three test repetitions was very low at 0.0090N, showing that the results for each design/posture combination were extremely repeatable. We see a consistent linear relationship between theoretical and experimental MIVs with an R^2 value of 0.987. This result shows that the theoretical calculations are very good at predicting actual performance. The slope of the line is 0.879, which we interpret to represent an average loss of performance of about 12% from theoretical predictions, likely due mainly to friction in the system. We show experimental and theoretical feasible force sets for one test of designs 1 and 6 in the main posture in Figure 9.8d, and we can see visually that the shape of the theoretical feasible force sets was extremely similar to those of the experimental feasible force sets, although the experimental ones were contracted to an extent.

We can see several interesting features in Figure 9.8. First of all, in Figure 9.8a, we see that routings 1 and 5 are identical except that 2 of the signs in the moment arm matrix are reversed (i.e., 2 of the tendons are switched from one side of the ad-abduction

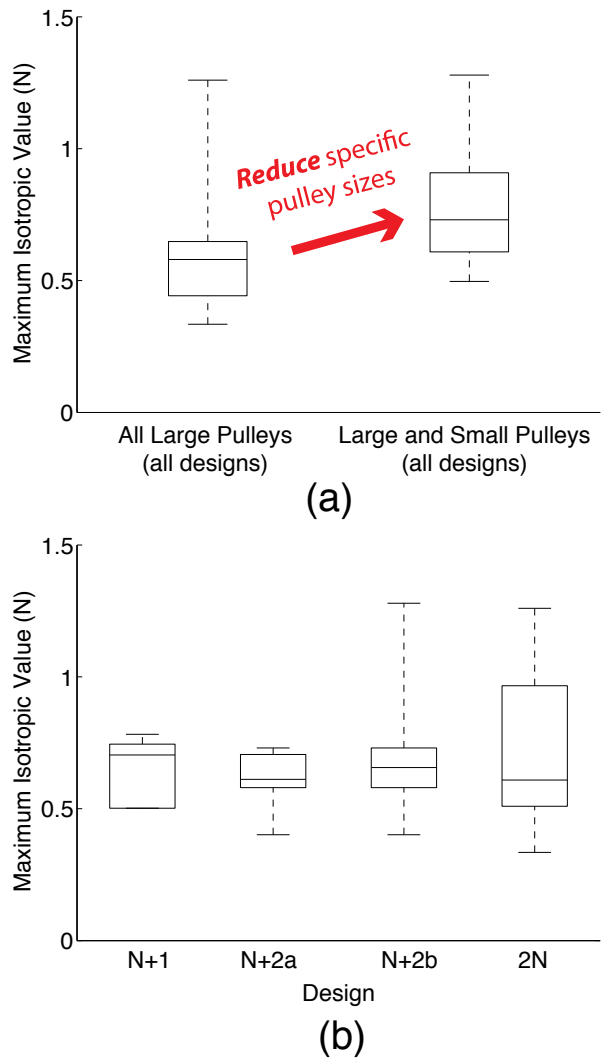


Figure 9.7: Maximum isotropic values for various routings. (a) Boxplot of MIV for all designs before and after pulley-size optimization. (b) Boxplot of MIV vs. design (includes optimized and unoptimized pulley sizes).

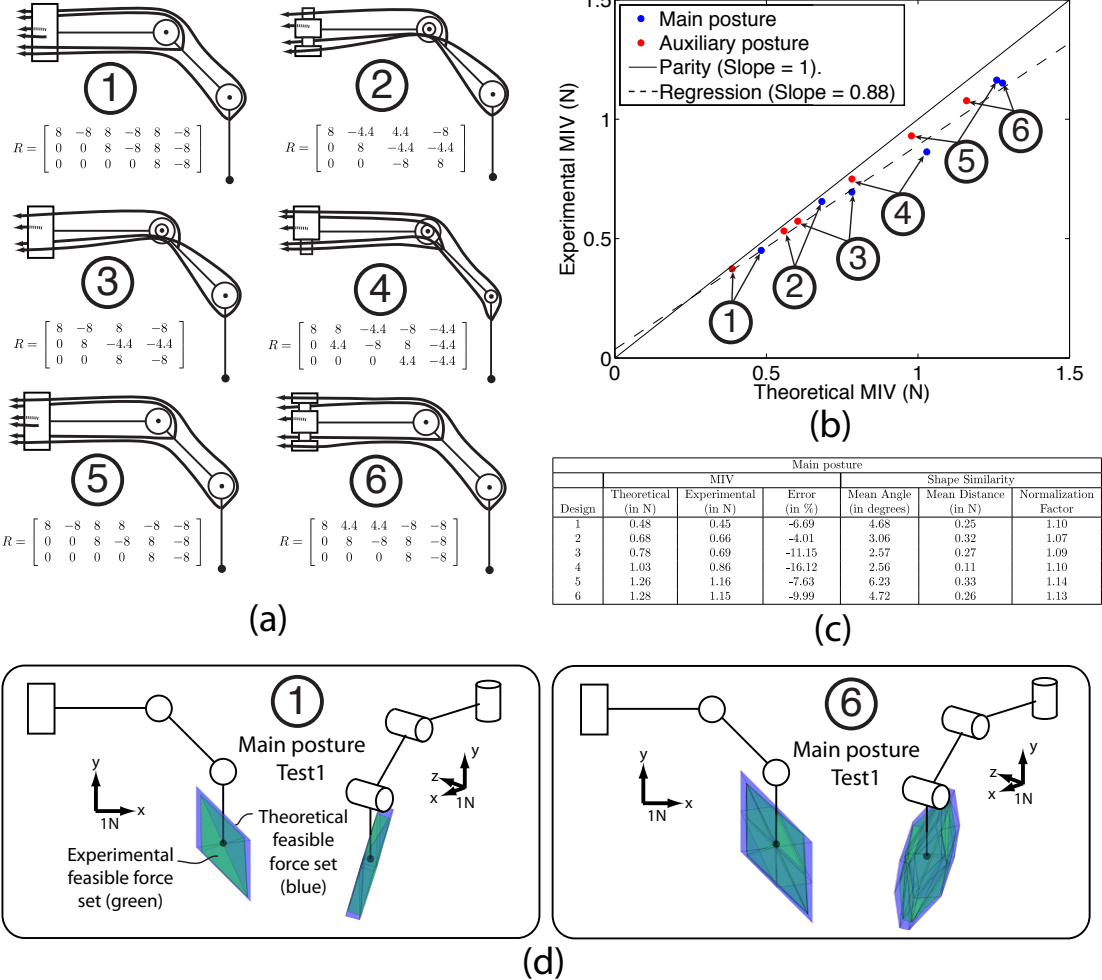


Figure 9.8: Results from experimental testing of various routings. (a) The 6 different routings tested. Shown to scale. R matrix values are in mm. (b) Experimental vs. theoretical MIV. Parity line is where experimental MIV would be exactly equal to theoretical MIV (intercept of 0, slope of 1). Regression has an R^2 value of 0.987. (c) Table of averages from 3 tests for each design in main posture. (d) 3-D visualization of experimental and theoretical feasible force sets for designs 1 and 6.

joint to the other). However, we can see in Figure 9.8b and the table in Figure 9.8c that the MIV of routing 5 is more than twice that of routing 1 both theoretically and experimentally. Figure 9.9 emphasizes this large change in MIV for a small, intelligent (but perhaps counterintuitive before performing the analyses) change in tendon routing. Secondly, the MIVs of routings 5 and 6 are very similar, but routing 6 has one less tendon. Thirdly, routings 2 and 3 have two fewer tendons than routing 1 but still outperform it in terms of MIV. Figure 9.8d demonstrates visually that the experimental feasible force sets corresponded very closely with the theoretical feasible force sets in shape, and that the size was similar but contracted by a small amount due to friction. While the side views of both of these feasible force sets look similar, the isometric views show clearly that the feasible force set of routing 1 is quite thin along one direction (which results in a low MIV) and the feasible force set of routing 6 is much more expanded in all directions (so the MIV is much higher).

In Figure 9.8b, we see that the data points lie underneath but fairly close to the parity line (if the theoretical and experimental MIVs were identical, the data points would lie exactly on the parity line). As would be expected, none of them are above the parity line. In the table in Figure 9.8c, we see that the error in the prediction of MIV ranged roughly between 4% and 16% which is the percentage MIV below the parity line where the data points are located. As far as shape goes, we see that the average difference in angles between corresponding vertices of the feasible force sets was between 2.56° and 6.5° . A

small amount of angular error would be expected due to error in the positioning and alignment of the JR3 axes relative to the finger axes, so this contributes to the average difference in angles. The mean distance of corresponding vertices is less than 0.35N. The normalization factors were less than 1.15, and it is the factor by which the experimental feasible force set had to be expanded in every direction to have the same volume as the theoretical feasible force set. It roughly corresponds with the MIV error.

9.6 Discussion

In this work, we have investigated the effect of various tendon routings on the set of feasible forces that can be exerted by a robotic finger both computationally and in a physical system. We see that routing has a very dramatic effect on the shape and size of the feasible force set. We also see that computational predictions are quite accurate and that they can be useful when making informed design decisions. Therefore the main conclusions of this study are twofold:

1. Different routings in robotic fingers can result in extremely different force-production capabilities.
2. Theoretical feasible force set analyses predict experimental force-production performance quite well and therefore they are a useful design tool.

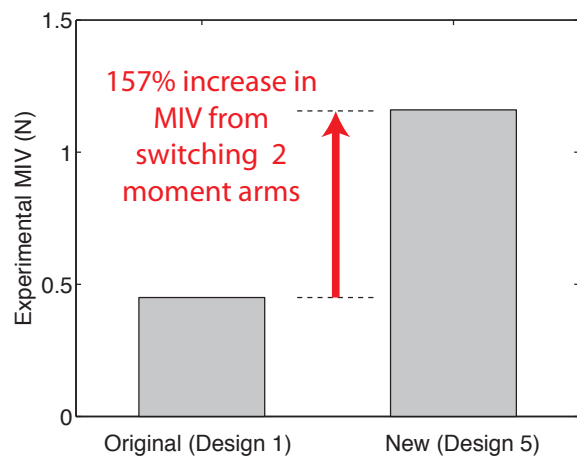
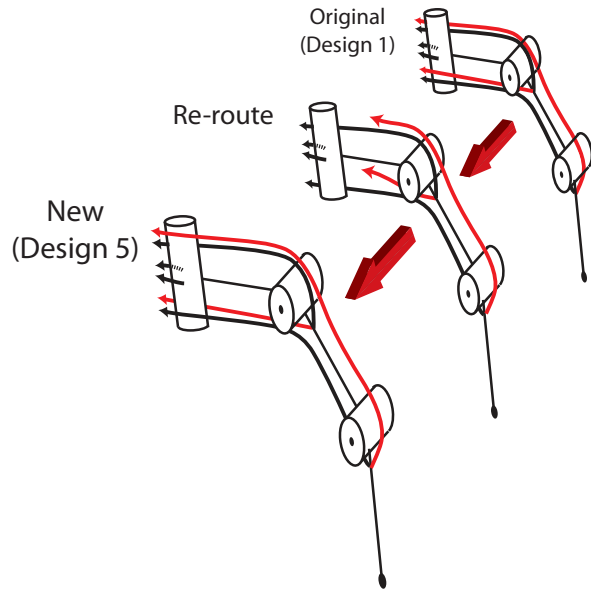


Figure 9.9: Illustration of a simple (but intelligent) tendon re-routing that drastically increases MIV.

One application of this work is to design tendon-driven fingers and manipulators for a given task that are optimized in terms of minimal size, weight, complexity, and cost. Since tendon-driven systems are linear for fixed postures, if we double all the moment arms (or the maximal tensions of all tendons), we double the size of feasible force set in every direction. Our results showed that the MIV for routing 6 was more than 100% greater than that of routing 1. Therefore, one could either reduce all of the maximal tendon tensions or all of the moment arms in routing 6 by 50% and still have a greater MIV than routing 1. In a robotic hand system, if the maximal tendon tensions were cut in half (by implementing smaller motors), then the weight of the actuators could be roughly halved and cost would be reduced. This would be very desirable, in general. If tendons are driving a minimally-invasive surgical instrument, then the moment arms could be halved and therefore the diameter of the instrument would be halved (which actually would reduce the cross-sectional area by 75%!). The instrument would then be much smaller and could be much better suited for certain surgical procedures.

We have used MIV as the fitness metric for our analyses since no prior assumption of task specification was made. We acknowledge that in general, the MIV would typically be more practically used for a tendon-driven, multi-purpose manipulator rather than a robotic finger. These analyses and optimizations that we described apply equally to tendon-driven manipulators and fingers regardless of size. Since we were only testing one finger in this paper, we decided to use the MIV. Current work has accomplished design

optimization and validation for grasp quality of multiple fingers of identical design to the one in this paper.

If a necessary task or set of tasks is known (e.g., to have high flexion force for strong grasps) then the analyses could assign a fitness metric to a routing based on that task specification. The optimization could then be based on that metric. For example, if it is desired to have a very strong flexion force with low extension force requirements, then linear programming can easily be used to determine the maximal force possible in the flexing direction(s) after the feasible force set has been calculated (e.g., using the generic procedure outlined in (Fu & Pollard 2006)). We have previously described that the feasible force sets of the human fingers are asymmetrically biased towards endpoint forces in the flexion direction than in the extension which is anatomically reasonable for grasping tasks (Inouye et al. 2011*b*, Valero-Cuevas et al. 1998, Valero-Cuevas et al. 2000, Valero-Cuevas & Hentz 2002). If strong grasp and minimal size/weight/cost is desired for a set of fingers, then analyses like those used in (Inouye, Kutch & Valero-Cuevas 2011*a*) can be used to design an optimized tendon-driven robotic hand.

We have investigated force-production capabilities in this paper, but there are many other considerations that go into the design of a robotic hand. Other significant considerations include the robustness and effectiveness of control algorithms, passive stiffness

characteristics, sensitivity to friction and positioning errors, and maximal endpoint velocities. We acknowledge that force-production capabilities are only one piece of the design puzzle for optimized robotic fingers.

For reasons of practicality, we only analyzed and constructed routings where the tendons routed around every joint that they passed (i.e., that the structure matrix is pseudo-triangular, as in (Lee & Tsai 1991)) and where there were only two sizes of pulleys that could be chosen. Routings can, however, be designed where tendons pass through the center of joints (Gebensteiner et al. 2010), or where moment arms can have many feasible magnitudes. This opens up the design space even more, and exhaustive searches like the ones we performed in this study may be more laborious, or even not be feasible given the exponential growth of design options. In addition, tendon-driven fingers or manipulators with more than 3 degrees of freedom will tend to suffer from the curse of dimensionality in the design space, and a designer may have to use various optimization algorithms (Inouye et al. 2012) in a search for a “good enough” design which could then be selected for physical construction. Alternatively, a designer could come up with a handful of feasible, physically-realizable routings and then search in the vicinity of that region of the parameter space to determine feasible improvements with affordable computational cost (Valero-Cuevas et al. 2009).

The optimization process we used in this study only addressed this realization of a robotic finger. If a general robotic finger or manipulator has more joints or tendons, the

dimensionality of the design space increases dramatically and finding a globally optimum solution for a specific fitness metric (of which any task-specific metric may be used, not only the general MIV metric) may be computationally infeasible due to the curse of dimensionality. Other custom or typical optimization algorithms could be used to find solutions with a high fitness. Furthermore, in the case when the optimization may involve link lengths and D-H parameters in addition to tendon routing, number of tendons, and pulley sizes, then finding a locally optimal solution or just a good-enough solution could still be very useful. The main purpose of this study was to investigate the correlation of predictions with experiments, as opposed to identifying a general optimization method for tendon-driven robotic fingers and manipulators.

Tendon friction was a significant factor in our experiment, (as it is for any tendon driven system), especially for the tendons at the last joint that had to wrap around as many as 12 pulleys. The main source of friction seemed to be the pulleys, as general observation of the data indicated that tendons attached to the ad-abduction joint (which wrapped around 4 pulleys) suffered from very little friction loss (less than a few %) while the tendons that attached to the last joint (which wrapped around 12 pulleys and routed through the fairly complicated tendon redirection between the first and second joints) suffered from as much as 20% friction loss.

Future work will extend this experimental validation approach to routings of multiple fingers for optimized grasp quality. In addition, this work is easily applicable to refine the

design of generic tendon-driven manipulators. Furthermore, investigation of the control and structure of biological tendon-driven systems is now made possible using a similar framework.

9.7 Conclusions

We conclude from this validation that these computational methods are effective at predicting the performance of drastically different tendon-driven robotic finger (or manipulator) designs, and are therefore a useful design tool. Various benefits of fully utilizing this design tool include

1. Minimization of weight: if a superior design has a force-production performance twice that of an inferior design, the superior design's actuators only need to be half the strength of the inferior design's to match the inferior design's performance, which in general corresponds to a large reduction in weight of the actuators.
2. Minimization of size: if a superior design has a force-production performance twice that of an inferior design, the superior design's moment arms only need to be half the size of the inferior design's to match the inferior design's performance, which could be used to half the overall thickness of the finger (or manipulator, or minimally-invasive surgical device).

3. Minimization of number of tendons (and therefore actuators): If a design with less tendons (such as an $N+1$ design) can be synthesized with the same force-production performance as that of one with more tendons (such as a $2N$ design), then the actuator system can be simplified and less space to rout the tendons inside the finger (or manipulator, or minimally-invasive surgical device) is needed.

Acknowledgements

The authors gratefully acknowledge the help of Manish Kurse in providing the data acquisition routine for the experimental procedure, and Dr. Veronica Santos for construction of the gimbal used in the experiments.

Chapter 10

Computational Optimization and Experimental Evaluation of Grasp Quality for Tendon-Driven Hands Under Constraints

10.1 Abstract

The chief tasks of robotic and prosthetic hands are grasping and manipulating objects, and size and weight constraints are very influential in their design. In this study we use computational modeling to both predict and optimize the grasp quality of a reconfigurable, tendon-driven hand. Our computational results show that grasp quality, measured by the radius of the largest ball in wrench space, could be improved up to 259% by simply making some pulleys smaller and redistributing the maximal tensions of the tendons. We experimentally evaluated several optimized and unoptimized designs, which had either 4, 5, or 6 tendons, and found that the theoretical calculations are effective at predicting

grasp quality, with an average friction loss in this system of around 30%. We conclude that this optimization can be a very useful design tool, and that using biologically-inspired asymmetry and parameter variability can be used to maximize performance.

10.2 Introduction

Robotic and prosthetic hands have been designed for many years, and their essential tasks are grasping and manipulating objects (Jacobsen et al. 1986, Salisbury & Craig 1982, Shadow Robot Company n.d., Grebenstein et al. n.d., Ambrose et al. 2000, Jau 1995, Massa et al. 2002, Lin & Huang 1996, Kawasaki et al. 2002, Namiki et al. 2003, Yamano & Maeno 2005, Gaiser et al. 2008). Many robotic and prosthetic hands also are designed with approximately the same shape and/or size as the human hand in order to be able to perform tasks in place of a human. Weight and size constraints are two of the paramount design constraints for these manipulators. Actuators for the fingers, typically located proximal to the hand, are generally either larger or heavier if they are able to produce more tension. This is also the case in the human hand: larger muscles are both heavier and stronger. In addition, the pulley sizes in the fingers cannot be made too big, otherwise the finger itself will become too large. In this paper, we utilize two reconfigurable fingers to test computational predictions of grasp quality for a given tendon routing whose pulley

sizes are constrained and the sum of maximal tendon tensions is constrained (due to weight and size constraints on the actuation system).

In addition to maximizing performance for a set of given constraints, the optimization techniques presented here can also be used to minimize size or weight given performance requirements. This is a useful tool when designing certain tendon-driven systems, such as minimally-invasive surgical devices (minimization of size and number of actuators desired) and prosthetic hands (minimization of weight desired). The consequences of over-designing the capabilities of these systems are increased weight, cost, size, and power consumption. Other capabilities important in the design of these systems are position control, force control, velocity production, and design simplicity.

A large body of literature exists which addresses grasp quality of objects by robotic hands and manipulators. Some studies have looked at grasp quality in order to determine the optimal finger placement on an object by a robotic hand (Miller & Allen 1999, Miller & Allen 2004, Surez Feijo et al. 2006, Borst, Fischer & Hirzinger 2003). However, they do not take into account the mechanical capabilities of the fingers and therefore are only useful in optimizing grasp placement and hand kinematics, not in optimizing the design parameters. Mechanical design parameters were taken into account for tendon-driven hands in (Fu & Pollard 2006), but they did not optimize over the parameters. Optimization of parameters given requirements on force production for a single finger was examined in (Pollard & Gilbert 2002), but they did not implement any of the optimized

designs in hardware, and they did not optimize for grasp quality. The hardware implementation of robotic hands has been widely accomplished (Jacobsen et al. 1986, Salisbury & Craig 1982, Shadow Robot Company n.d., Grebenstein et al. n.d., Ambrose et al. 2000, Jau 1995, Massa et al. 2002, Lin & Huang 1996, Kawasaki et al. 2002, Namiki et al. 2003, Yamano & Maeno 2005, Gaiser et al. 2008), but their choice of design parameters has not been guided by a systematic optimization or analyses of grasp quality.

Our study uses a previously-developed computational framework (Inouye et al. 2012) to evaluate and optimize the grasp quality of a reconfigurable tendon-driven hand (taking into account all design parameters and constraints). The mechanical design of the reconfigurable fingers is identical to that of a finger used in another study for single finger force-production analysis and optimization (Inouye, Kutch & Valero-Cuevas n.d.). We show that under constraints, optimization of design parameters can improve grasp performance by more than 200%, and our predictions of grasp quality are corroborated by experimental results.

10.3 Methods

10.3.1 Hand Construction

The robotic hand we optimized and tested consisted of two reconfigurable fingers, which were designed for a previous study (Inouye et al. n.d.). 2-D views of the finger design

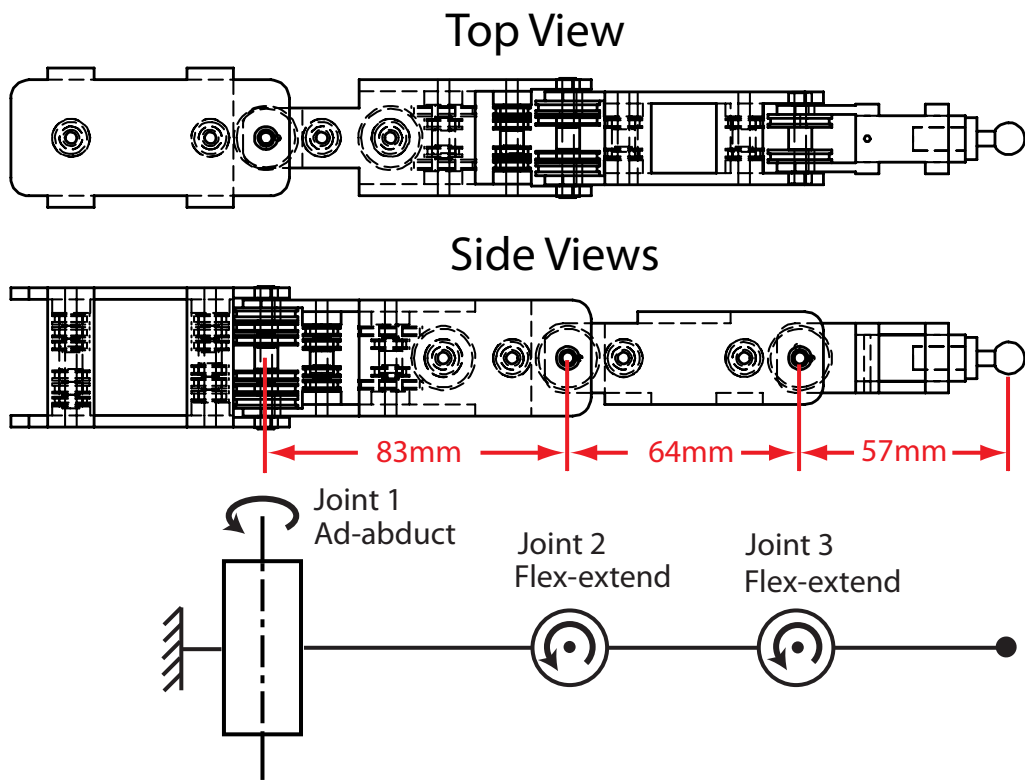


Figure 10.1: Top and side views of finger design and kinematics.

are shown in Figure 10.1. The fingers were able to accept arbitrary tendon routings that were analyzed and optimized computationally. In addition, the pulley size was variable, consisting of two options: a large pulley, with radius 8mm, and a small pulley, with radius 4.4mm. Each of the custom pulleys was fitted with ball bearings to minimize friction.

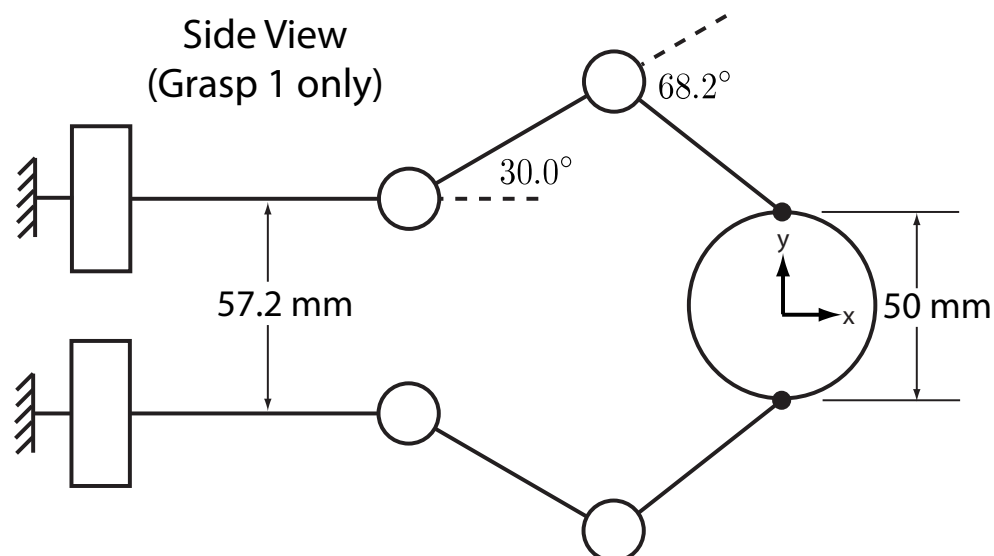
10.3.2 Grasp Quality Analysis

Our calculation of grasp quality was based on the wrench-direction-independent metric known as the radius of largest ball, originally proposed by (Ferrari & Canny 1992). The metric, in effect, is equal to the maximal magnitude of a wrench that can be applied to the object in all directions in wrench space without it losing force closure (i.e., causing the grasp to fail). A wrench vector whose magnitude is less than the grasp quality can be applied to the object *in any direction in wrench space* without losing force closure. The process for efficiently calculating the grasp quality and optimizing the parameters of a tendon-driven hand was originally developed in (Inouye et al. 2012).

Briefly, the grasp quality analysis first involves selecting the initial grasp parameters: the finger geometry, object size and shape, grasping points, and number of fingers. These are shown for this experiment in Figure 10.2. We analyzed grasp quality for two different finger placements, also in Figure 10.2. Next, the fingertip force-production capabilities for each finger are determined by calculating the feasible force set, which is a function of finger posture and geometry, tendon routing and pulley sizes, and maximal tensions of the tendons (Valero-Cuevas 2005). The finger Jacobian, J , relating joint angle velocities to endpoint velocities, is determined from the geometry (i.e., D-H parameters) of the finger and the finger posture. The tendon routing and pulley sizes determine the moment arm matrix R . The maximal tensions of the tendons define the diagonal F_0 matrix. After the

feasible force sets are calculated, they are intersected with friction cones whose orientation is dependent on fingertip contact angle in order to produce a feasible object force set. We used a coefficient of friction of 0.5 for this study. This set represents the forces that can be applied to the object by the fingertip. The feasible object force set is calculated for each finger, using the finger placements determined initially. These sets are used to determine all the forces and torques that can be resisted in wrench space (i.e., the grasp wrench set), from which the grasp quality metric is then calculated using the Quickhull algorithm (Barber et al. 1996) implemented in the software program Qhull.

The construction of the finger allowed for various moment arm matrices (which define the tendon routing and pulley sizes of the finger) to be implemented which had 4, 5, or 6 tendons. These designs are known as $N+1$, $N+2$, and $2N$ designs, where N is the degrees of freedom of the finger. We enumerated all possible moment arm matrices beginning with the “base” matrices shown in Figure 10.3. We replaced each ‘#’ with either a 1 or -1 (in accordance with the sign of the moment exerted on a joint when the corresponding tendon is under tension; see Figure 10.1 for definition of joint axes) in a full combinatoric search and then checked the controllability conditions as described in (Lee & Tsai 1991). This resulted in a total of 252 realizable, unique routings (with all large moment arms). The construction of the finger only allowed for routings where the tendons routed around every joint that they passed (i.e., that the moment arm matrix is pseudo-triangular, as in (Lee & Tsai 1991)).



Isometric View **Front View**

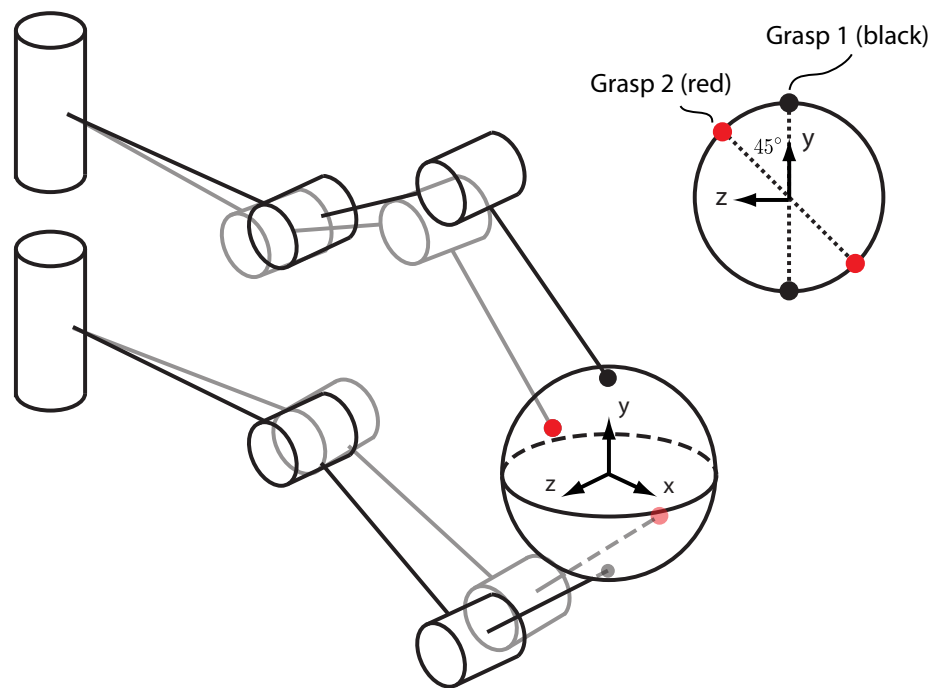


Figure 10.2: Finger placements for each grasp.

$$\begin{array}{c}
 \text{N+1 design} \\
 R = \left[\begin{array}{ccccc} \# & \# & \# & \# \\ 0 & \# & \# & \# \\ 0 & 0 & \# & \# \end{array} \right] \quad \text{N+2 design} \\
 R = \left[\begin{array}{ccccc} \# & \# & \# & \# & \# \\ 0 & \# & \# & \# & \# \\ 0 & 0 & 0 & \# & \# \end{array} \right] \\
 \\
 \text{2N design} \\
 R = \left[\begin{array}{cccccc} \# & \# & \# & \# & \# & \# \\ 0 & 0 & \# & \# & \# & \# \\ 0 & 0 & 0 & 0 & \# & \# \end{array} \right]
 \end{array}$$

Figure 10.3: Base moment arm matrices used when finding realizable, unique tendon routings.

We then calculated the grasp quality for these routings using the large pulleys and an even distribution of maximal tendon tension. The sum of maximal tendon tensions was limited to 60N for each finger ¹(i.e., for designs with 4, 5, and 6 tendons, the maximal tensions were 15N, 12N, and 10N, respectively).

10.3.3 Optimization of Grasp Quality

The fitness metric we used for optimization was the sum of the grasp qualities for grasp 1 and grasp 2 (they were both weighted equally).

¹The sum of maximal tendon tensions being equal is an important constraint due to the size, weight, and motor torque (and therefore tendon tension) limitations inherent in dexterous hands. For example, the torque capacity of motors is roughly proportional to motor weight, and minimization of weight was an important consideration in the design of the DLR Hand II (Butterfa et al. 2001). In addition, the maximal force production capabilities of McKibben-style muscles are roughly proportional to cross-sectional area (Pollard & Gilbert 2002). Since the actuators typically will be located in the forearm, then the total cross-sectional area will be limited to the forearm cross-sectional area. In this study, we do not consider alternative constraints on the actuation system (e.g., electrical current capacity, tendon velocities, etc).

10.3.3.1 Optimizing Pulley Sizes

We calculated the fitness for all combinations of large and small pulleys for the best routing from each of the base moment arm matrices shown in Figure 10.3. We also optimized the moment arms for the following naive 2N design (where 1 and -1 denote the large moment arm sizes), for a total of 4 pulley-size-optimized routings:

$$R_{\text{NAIVE } 2N} = \begin{bmatrix} 1 & -1 & 1 & -1 & 1 & -1 \\ 0 & 0 & 1 & -1 & 1 & -1 \\ 0 & 0 & 0 & 0 & 1 & -1 \end{bmatrix}$$

A combinatoric search for the 2N designs involved 12 moment arms, so $2^{12} = 4096$ fitness evaluations were performed. Similarly, the N+2 design had 2048 evaluations and the N+1 design had 512 evaluations.

10.3.3.2 Optimizing Tendon Tension Distribution

The last step in our optimization process involved performing a greedy Markov-Chain Monte Carlo algorithm on the maximal tendon tension distribution. Starting with all the tendons having equal maximal tendon tensions, we perturbed the distribution of the maximal tendon tensions using a multivariate normal distribution with standard deviation of 1% of the maximal tendon tension sum. This perturbation was effectively like one inside an n -dimensional hypercube in the positive orthant with side length equal

to maximal tendon tension sum, where n is the number of tendons for each finger. After perturbation inside the hypercube, we projected the point onto the hyperplane given by the following equation:

$$\sum_{i=1}^n F_{i,max} = \text{MaxTendonTensionSum} \quad (10.1)$$

where $F_{i,max}$ is the maximal tension of tendon i and one of the diagonal entries in the F_0 matrix. This would give us a new distribution of maximal tendon tensions, and we would then evaluate the fitness. If it was higher, we would take that point as the starting point for the next perturbation. The maximal tendon tensions were constrained so that they did not go negative or above the total maximum, and a reflection technique at those boundaries was used similar to that in (Santos et al. 2009). The overall process is shown graphically for a simplified 2-tendon example in Figure 10.4.

A detailed explanation of the effects of different structure matrices and distributions of maximal tendon tensions on the kinetostatic (i.e., force-production) capabilities of manipulators and biological hands can be found in (Valero-Cuevas 2005, Inouye et al. 2012, Lee & Tsai 1991, Finotello et al. 1998, Ou & Tsai 1993, Ou & Tsai 1996, Tsai 1995).

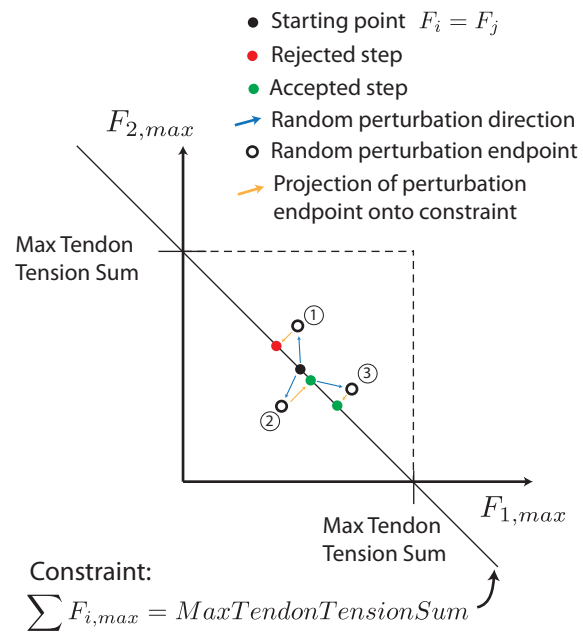


Figure 10.4: Illustration of Markov-Chain Monte Carlo algorithm for distribution of maximal tendon tensions.

10.3.4 Experimental testing of tendon routings

We tested each of the pulley-size-optimized layouts for each of the 4 routings (the best from each of the base matrices, and then the naive 2N). We tested them with optimized tendon tension distributions and unoptimized tendon tension distributions. This gave 8 finger design configurations, and we tested each of these 8 designs in both grasp configurations. This gave 16 tests. In addition, we tested the naive 2N design in both postures with unoptimized pulley sizes and unoptimized tendon tension distribution. So we obtained a total of 18 data points.

For each of the designs tested, we first arranged the pulleys and strings (0.4mm braided polyester twine) to match the desired configuration. We then mounted the fingers onto a base that was part of a motor array system as shown in Figure 10.5. The DC motors were coupled to shafts which string wound around. The string was then routed around pulleys that were attached to Interface SML 25 load cells which provided force measurements for the closed-loop controller implemented in LabView. The ends of the fingers had a ball which fit into a socket on the object that we designed to attach to the 6-axis JR3 load cell and also provide the correct finger placements. This ball-and-socket joint constrained translational motion but not rotational motion (we did not want the fingertip to be over-constrained). One object was printed for each grasp configuration. Both are shown in Figure 10.5. The sampling rate and control loop frequency were both 100Hz.

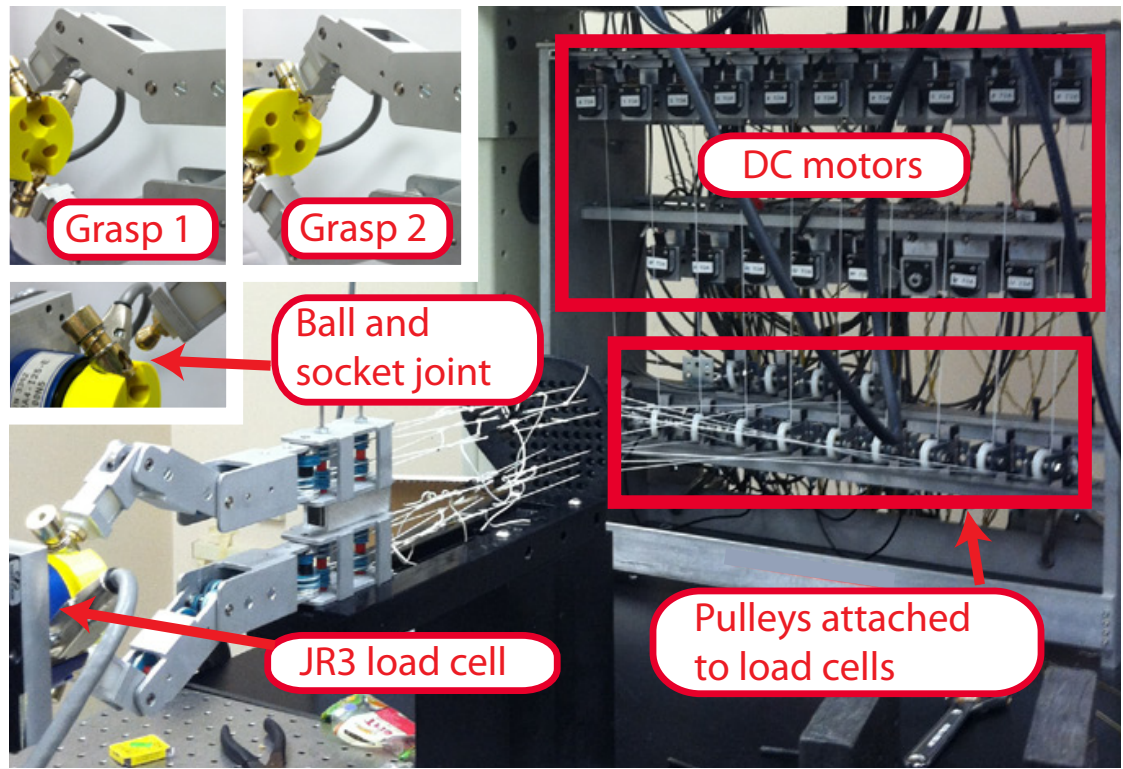


Figure 10.5: Experimental system for grasp testing.

A small pretension of 1N was applied to each string to remove slack and prevent the string from falling off of the pulleys. Then the Minkowski sum ² of each vertex of both feasible object force sets (described in the previous section) was applied to the strings (in addition to the pretension) in ramp-up, hold, and ramp-down phases to find the grasp wrench set. The vertices of this experimental grasp wrench set were determined from the hold phases and then used to find the grasp quality. The experimental grasp quality could then be compared with the theoretical grasp quality (from computational results).

10.4 Results

10.4.1 Computational grasp quality predictions

The 252 unoptimized routings produced the grasp qualities shown in Figure 10.6. The optimization paths for the best N+1, N+2, and 2N designs, plus the naive 2N design, are also shown. Each optimization step produced a higher fitness, and iso-fitness dashed lines are shown.

We see that the naive 2N design improved the most from the optimization steps. This would be expected since the other designs that were optimized already had the highest fitness from their base matrix. In fact, the naive 2N design improved its fitness by 259%.

²The Minkowski sum in this context refers to the combination of each vertex of one feasible object force set with every vertex of the other feasible object force set

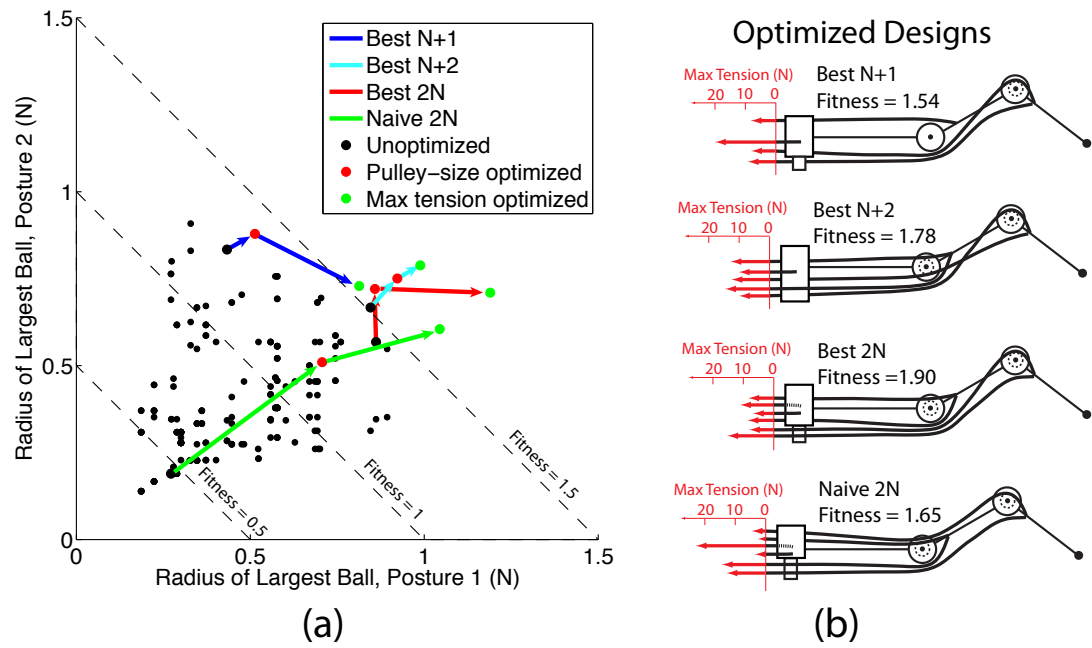


Figure 10.6: (a) Computational results of grasp quality for hand designs. Optimization paths shown. (b) Pulley-size and max tension optimized designs.

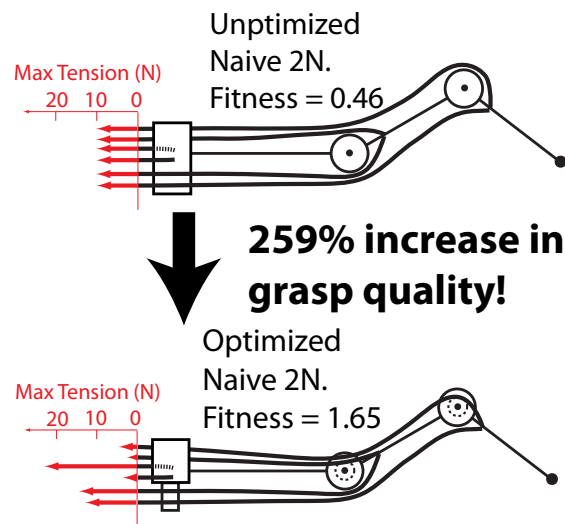


Figure 10.7: Computational predictions of fitness for unoptimized and optimized naive 2N design.

We see the optimization for the naive 2N design made 6 out of the 12 moment arms smaller and redistributed the maximal tensions severely, as seen in Figure 10.7.

Furthermore, we can see that the optimized N+1 design had a fitness that was higher than *any* of the unoptimized N+2 and 2N designs, even though it had fewer tendons. Fewer tendons, in general, would be desirable due to simplification of the actuation system and less complexity in design and manufacturing.

10.4.2 Theoretical predictions vs. experimental results

The experimental results are shown in Figure 10.8. We see that the data points lie underneath the parity line (if the theoretical and experimental grasp qualities were identical,

the data points would lie exactly on the parity line). As would be expected, none of them are above the parity line. We ran a regression on the data points and we felt it was reasonable to constrain the intercept to zero. The slope of the line was 0.70, which indicated around a 30% loss in quality, on average, due to friction and other experimental error. The coefficient of determination is not well defined for regressions whose constants are constrained to zero, but visually the fit is fairly good, and the main point is that in general, a prediction of higher (or at least much higher) grasp quality resulted in an experimental result of higher grasp quality. We show the 3-D force portions of the grasp wrench set in Figure 10.8 for two of the designs and we can see that the theoretical and experimental 3-D force portions of the grasp wrench sets are very similar in size and shape, with the experimental sets being contracted, mainly due to friction. We see that the optimized best 2N design has a 223% greater experimental grasp quality than the unoptimized naive 2N design in grasp 1.

10.5 Discussion

In this work, we have investigated the effect of tendon routings, pulley sizes, and distribution of maximal tendon tensions on the grasp quality of a tendon-driven robotic hand under design constraints. We see that altering all of these design parameters has a very

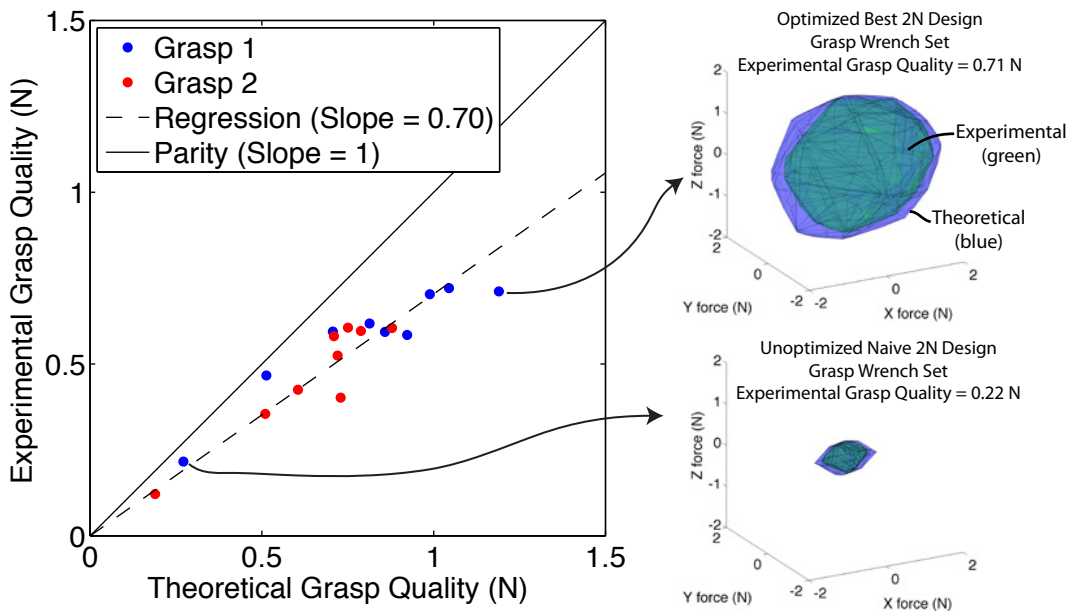


Figure 10.8: Results from experimental testing of various routings. Experimental vs. theoretical grasp quality for both grasps. Parity line is where experimental grasp quality would be exactly equal to theoretical grasp quality (intercept of 0, slope of 1). Regression line constant term forced to zero. 3-D force portions of grasp wrench set for two different tests shown on right (torque constrained to zero).

dramatic effect on grasp quality while still satisfying the constraints. We also see that computational predictions can be useful when making design decisions.

We have used radius of largest ball as the grasp quality metric for our analyses since no prior assumption of wrench direction specification was made. If a necessary wrench or set of wrenches is known (Borst, Fischer & Hirzinger n.d.) (e.g., to pick up a heavy object, pull on a cord, or turn a knob) then the analyses could assign a fitness metric to a routing based on that task specification, using a procedure similar to that used in (Fu & Pollard 2006). The optimization could then be based on that metric. In addition, any other grasp quality metric based on kinetostatic performance (such as the volume of the grasp wrench set (Miller & Allen 1999)) could be used to optimize a tendon-driven hand under constraints.

As in a previous study which utilized a single finger of the same design (Inouye et al. n.d.), we only analyzed and constructed routings where the tendons routed around every joint that they passed (i.e., that the structure matrix is pseudo-triangular, as in (Lee & Tsai 1991)) and where there were only two sizes of pulleys that could be chosen. Routings can be designed where tendons pass through the center of joints (Gebenstein et al. 2010), or where moment arms can have many feasible magnitudes. This opens up the design space even more, and exhaustive searches like the ones we performed in this study may not be feasible. In addition, tendon-driven fingers or manipulators with more than 3 degrees of freedom will tend to suffer from the curse of dimensionality in the design

space, and a designer may have to use various optimization algorithms (Inouye et al. 2012) in a search for a very good design which could then be designed for physical construction. Alternatively, a designer could come up with a handful of feasible, physically-realizable routings and then run these analyses to determine the best one.

Friction was a significant factor in our experiment, especially for the tendons at the last joint that had to wrap around as many as 12 pulleys. This high number of pulleys was necessary to ensure total reconfigurability. Fingers for a commercial robotic hand under constraints (such as a dexterous prosthetic hand) could use these computational methods to design routings where very few pulleys are necessary, and hence the friction could be reduced.

Moreover, the 30% reduction in grasp quality compared with predictions due to frictional loss and other experimental error can partly be explained by the fact that the grasp quality metric used was the “worst case scenario” (i.e., the magnitude of weakest wrench). This would result in the grasp quality being lowered by one or more of many sources of friction loss, small controller errors, or positioning errors of the load cell or fingers, and be similar to a “max error” operator. The experimental volume of the grasp wrench set, which can be viewed as an approximation of the average wrench that can be produced by the fingers, is much more consistent with predictions, as shown in Figure 10.9. This could be viewed as an “average error” operator. We have plotted the volume to the one-fifth power to linearly scale the volume for inspection.

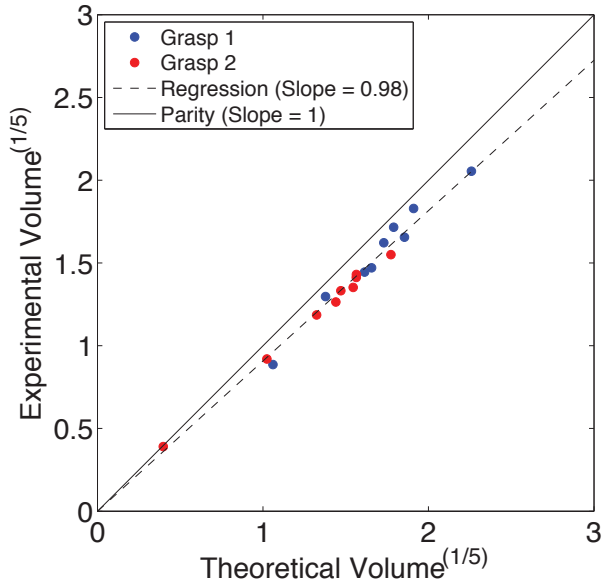


Figure 10.9: Experimental vs. predicted volumes of grasp wrench sets.

We have investigated grasp quality in this paper, but there are many other considerations that go into the design of a robotic hand. Other significant considerations are the effectiveness of control algorithms, passive stiffness characteristics, sensitivity to friction and positioning errors, and maximal finger velocities. We acknowledge that grasp quality is only one piece of the design puzzle for optimized robotic hands.

This work is also easily extended to the case of underactuated hands. These hands are simpler to design and control, and current users of prosthetic hands can only transfer a few reliable signals to the hand. This limited control bandwidth currently restricts the applicability of these results to prosthetic hands at the current stage of neural interface

development. However, as the number of reliable neural or cortical signals from amputees increases, the market for dexterous prosthetic hands will increase dramatically.

This study also gives us insight into the anatomy of the human hand. The human hand's tendon routing is very asymmetric, the distribution of maximal tendon tensions is extremely skewed, and the magnitudes of the moment arms vary widely. In the index finger, the smallest muscle is only 10% of the strength of the largest muscle, the magnitude of the smallest moment arm is approximately 10% of that of the largest moment arm, and it utilizes one less tendon than a 2N design (Valero-Cuevas et al. 2000). In fact, our optimized results show that *none* of the optimized designs had much symmetry. We feel that the biological inspiration from these parameter variances can be used in the design of tendon-driven robotic systems to maximize performance.

Acknowledgements

The authors gratefully acknowledge the help of Dr. Jason Kutch and Manish Kurse in providing the data acquisition routine for the experimental procedure, and also for their helpful comments.

Chapter 11

Conclusions and Future Work

The central contribution of the work in this dissertation is providing and testing advanced computational methods for the systematic design and optimization of bio-inspired tendon-driven systems. Some of the systems that can be analyzed and optimized with the computational methods developed here include minimally-invasive surgical devices, robotic and prosthetic hands, lightweight robotic arms, miniature robots, rescue robots, and service robots. As the market for advanced, dexterous robotic and prosthetic devices grow, optimization of cost, weight, and size will be important considerations in a competitive commercial market.

In addition, in-depth analysis of the neuromuscular systems of the human body can be performed using these methods to offer insight and inspiration for robotic mechanisms, medical devices, and physical therapy. A thorough understanding of biomechanics and the

effects of various neuromuscular and cognitive disorders on normal function is necessary to develop and implement new and effective treatment modalities.

Bibliography

- Alici, G. & Shirinzadeh, B. (2005), ‘Enhanced stiffness modeling, identification and characterization for robot manipulators’, *Robotics, IEEE Transactions on* **21**(4), 554–564.
- Ambrose, R. O., Aldridge, H., Askew, R. S., Burridge, R. R., Bluethmann, W., Diftler, M., Lovchik, C., Magruder, D. & Rehnmark, F. (2000), ‘Robonaut: Nasa’s space humanoid’, *IEEE Intelligent Systems and Their Applications* **15**(4), 57–63.
- Angeles, J. (2004), ‘On the optimum dimensioning of robotic manipulators’.
- Aref, M. M., Taghirad, H. D. & Barissi, S. (2009), ‘Optimal design of dexterous cable driven parallel manipulators’.
- Avis, D. (2000), A revised implementation of the reverse search vertex enumeration algorithm, Vol. 29, pp. 177–198. In: Polytopes - Combinatorics and Computation, G. Kalai & G. Ziegler eds., Birkhauser-Verlag, DMV Seminar Band 29.
- Barber, C. B., Dobkin, D. P. & Huhdanpaa, H. (1996), ‘The quickhull algorithm for convex hulls’, *ACM Transactions on Mathematical Software (TOMS)* **22**(4), 469–483.
- Birglen, L. & Gosselin, C. M. (2004), ‘Kinetostatic analysis of underactuated fingers’, *Robotics and Automation, IEEE Transactions on* **20**(2), 211–221.
- Borst, C., Fischer, M. & Hirzinger, G. (2003), Grasping the dice by dicing the grasp, Vol. 4. 2003 IEEE/RSJ International Conference on Intelligent Robots and Systems, 2003.(IROS 2003). Proceedings.
- Borst, C., Fischer, M. & Hirzinger, G. (n.d.), Grasp planning: How to choose a suitable task wrench space, pp. 319–325. 2004 IEEE International Conference on Robotics and Automation, 2004. Proceedings. ICRA’04.

- Bouchard, S., Gosselin, C. M. & Moore, B. (n.d.), On the ability of a cable-driven robot to generate a prescribed set of wrenches, Citeseer. Proc. of the ASME International Design Engineering Technical Conferences, Mechanics and Robotics Conference.
- Burdet, E., Osu, R., Franklin, D. W., Milner, T. E. & Kawato, M. (2001), ‘The central nervous system stabilizes unstable dynamics by learning optimal impedance’, *Nature* **414**(6862), 446–449.
- Burdet, E., Osu, R., Franklin, D. W., Yoshioka, T., Milner, T. E. & Kawato, M. (2000), ‘A method for measuring endpoint stiffness during multi-joint arm movements’, *Journal of Biomechanics* **33**(12), 1705–1709.
- Burdick, J. W. (2002), On the inverse kinematics of redundant manipulators: Characterization of the self-motion manifolds, IEEE, pp. 264–270. Robotics and Automation, 1989. Proceedings., 1989 IEEE International Conference on.
- Butterfa, J., Grebenstein, M., Liu, H. & Hirzinger, G. (2001), Dlr-hand ii: Next generation of a dextrous robot hand, Vol. 1, IEEE, pp. 109–114 vol. 1. Robotics and Automation, 2001. Proceedings 2001 ICRA. IEEE International Conference on.
- Chablat, D. & Angeles, J. (2002), ‘On the kinetostatic optimization of revolute-coupled planar manipulators’, *Mechanism and machine theory* **37**(4), 351–374.
- Chang, S. L., Lee, J. J. & Yen, H. C. (2005), ‘Kinematic and compliance analysis for tendon-driven robotic mechanisms with flexible tendons’, *Mechanism and machine theory* **40**(6), 728–739.
- Chen, D. Z., Su, J. C. & Yao, K. L. (1999), ‘A decomposition approach for the kinematic synthesis of tendon-driven manipulators’, *Journal of Robotic Systems* **16**(8), 433–443.
- Chen, S. F. & Kao, I. (2000), ‘Conservative congruence transformation for joint and cartesian stiffness matrices of robotic hands and fingers’, *The International Journal of Robotics Research* **19**(9), 835–847.
- Chen, X., Womersley, R. S. & Ye, J. (2011), ‘Minimizing the condition number of a gram matrix’, *SIAM J. Optim* **21**, 127148.
- Chiachio, P., Bouffard-Vercelli, Y. & Pierrot, F. (1997), ‘Force polytope and force ellipsoid for redundant manipulators’, *Journal of Robotic Systems* **14**(8), 613–620.
- Ciblak, N. & Lipkin, H. (1994), Asymmetric cartesian stiffness for the modeling of compliant robotic systems, Vol. 72, pp. 197–204. Proc. ASME 23rd Biennial Mech. Conf., Des. Eng. Div.

- Ciblak, N. & Lipkin, H. (1999), Synthesis of cartesian stiffness for robotic applications, Vol. 3, IEEE, pp. 2147–2152 vol. 3. Robotics and Automation, 1999. Proceedings. 1999 IEEE International Conference on.
- Ciocarlie, M., Miller, A. & Allen, P. (2005), Grasp analysis using deformable fingers, pp. 4122–4128. 2005 IEEE/RSJ International Conference on Intelligent Robots and Systems, 2005.(IROS 2005).
- Cui, L., Perreault, E. J., Maas, H. & Sandercock, T. G. (2008), ‘Modeling short-range stiffness of feline lower hindlimb muscles’, *Journal of Biomechanics* **41**(9), 1945–1952.
- Dai, J. S. & Kerr, D. R. (1996), ‘Analysis of force distribution in grasps using augmentation’, *ARCHIVE: Proceedings of the Institution of Mechanical Engineers, Part C: Journal of Mechanical Engineering Science 1989-1996 (vols 203-210)* **210**(13), 15–22.
- Dai, J. S. & Kerr, D. R. (2000), ‘A six-component contact force measurement device based on the stewart platform’, *Proceedings of the Institution of Mechanical Engineers, Part C: Journal of Mechanical Engineering Science* **214**(5), 687.
- Dai, J. S. & Kerr, D. R. (2002), ‘A computation environment for restraint analysis and synthesis in robotic grasping’, *International Journal of Engineering Simulation* **3**(2), 16–25.
- Darainy, M., Malfait, N., Gribble, P. L., Towhidkhah, F. & Ostry, D. J. (2004), ‘Learning to control arm stiffness under static conditions’, *Journal of Neurophysiology* **92**(6), 3344.
- Denavit, J. (1955), ‘A kinematic notation for lower-pair mechanisms based on matrices’, *Trans. of the ASME. Journal of Applied Mechanics* **22**, 215–221.
- Deshpande, A. D., Balasubramanian, R., Lin, R., Dallon, B. & Matsuoka, Y. (2008), Understanding variable moment arms for the index finger mcp joints through the act hand, IEEE, pp. 776–782. Biomedical Robotics and Biomechatronics, 2008. BioRob 2008. 2nd IEEE RAS & EMBS International Conference on.
- Elsner, L., He, C. & Mehrmann, V. (1995), ‘Minimization of the norm, the norm of the inverse and the condition number of a matrix by completion’, *Numerical linear algebra with applications* **2**(2), 155–171.
- Fagg, A. H., Sitkoff, N., Barto, A. G. & Houk, J. C. (1997), Cerebellar learning for control of a two-link arm in muscle space, Vol. 3, IEEE, pp. 2638–2644 vol. 3. Robotics and Automation, 1997. Proceedings., 1997 IEEE International Conference on.

- Ferrari, C. & Canny, J. (1992), Planning optimal grasps, IEEE, pp. 2290–2295. Robotics and Automation, 1992. Proceedings., 1992 IEEE International Conference on.
- Finotello, R., Grasso, T., Rossi, G. & Terribile, A. (1998), Computation of kinetostatic performances of robot manipulators with polytopes, Vol. 4, IEEE, pp. 3241–3246. Robotics and Automation, 1998. Proceedings. 1998 IEEE International Conference on.
- Firmani, F., Zibil, A., Nokleby, S. B. & Podhorodeski, R. P. (2008), ‘Wrench capabilities of planar parallel manipulators. part i: Wrench polytopes and performance indices’, *Robotica* **26**(06), 791–802.
- Flash, T. & Mussa-Ivaldi, F. (1990), ‘Human arm stiffness characteristics during the maintenance of posture’, *Experimental brain research* **82**(2), 315–326.
- Franklin, D. W., Liaw, G., Milner, T. E., Osu, R., Burdet, E. & Kawato, M. (2007), ‘Endpoint stiffness of the arm is directionally tuned to instability in the environment’, *The Journal of Neuroscience* **27**(29), 7705–7716.
- Franklin, D. W., So, U., Kawato, M. & Milner, T. E. (2004), ‘Impedance control balances stability with metabolically costly muscle activation’, *Journal of Neurophysiology* **92**(5), 3097.
- Fu, J. L. & Pollard, N. S. (2006), On the importance of asymmetries in grasp quality metrics for tendon driven hands, pp. 1068–1075. 2006 IEEE/RSJ International Conference on Intelligent Robots and Systems.
- Fukuda, K. & Prodon, A. (1996), ‘Double description method revisited’, *Combinatorics and Computer Science* pp. 91–111.
- Gaiser, I., Schulz, S., Kargov, A., Klosek, H., Bierbaum, A., Pylatiuk, C., Oberle, R., Werner, T., Asfour, T. & Breithauer, G. (2008), A new anthropomorphic robotic hand, IEEE, pp. 418–422. Humanoid Robots, 2008. Humanoids 2008. 8th IEEE-RAS International Conference on.
- Garland, M. (2004), ‘Qslim software package’.
- Garland, M. & Heckbert, P. S. (1997), Surface simplification using quadric error metrics, ACM Press/Addison-Wesley Publishing Co., p. 216. Proceedings of the 24th annual conference on Computer graphics and interactive techniques.
- Ghafoor, A., Dai, J. S. & Duffy, J. (2004), ‘Stiffness modeling of the soft-finger contact in robotic grasping’, *Journal of mechanical design* **126**, 646.

- Gomi, H. & Osu, R. (1998), ‘Task-dependent viscoelasticity of human multijoint arm and its spatial characteristics for interaction with environments’, *The Journal of Neuroscience* **18**(21), 8965–8978.
- Gouttefarde, M. & Krut, S. (2010), ‘Characterization of parallel manipulator available wrench set facets’, *Advances in Robot Kinematics: Motion in Man and Machine* pp. 475–482.
- Gebensteiner, M., Albu-Schaffer, A., Bahls, T., Chalon, M., Eiberger, O., Friedl, W., Gruber, R., Hagn, U., Haslinger, R. & Hppner, H. (n.d.), ‘The dlr hand arm system’, *Submitted to ICRA* **11**.
- Gebensteiner, M., Chalon, M., Hirzinger, G. & Siegwart, R. (2010), Antagonistically driven finger design for the anthropomorphic dlr hand arm system. Proc. IEEE-RAS International Conference on Humanoid Robots (HUMANOIDS).
- Gebensteiner, M. & van der Smagt, P. (2008), ‘Antagonism for a highly anthropomorphic handarm system’, *Advanced Robotics* **22**(1), 39–55.
- Hashimoto, M. & Imamura, Y. (1994), Design and characteristics of a parallel link compliant wrist, IEEE, pp. 2457–2462 vol. 3. Robotics and Automation, 1994. Proceedings., 1994 IEEE International Conference on.
- Hogan, N. (1984), ‘Adaptive control of mechanical impedance by coactivation of antagonist muscles’, *Automatic Control, IEEE Transactions on* **29**(8), 681–690.
- Hogan, N. (1985a), ‘Impedance control—an approach to manipulation. i-theory. ii-implementation. iii-applications’, *ASME Transactions Journal of Dynamic Systems and Measurement Control B* **107**, 1–24.
- Hogan, N. (1985b), ‘The mechanics of multi-joint posture and movement control’, *Biological cybernetics* **52**(5), 315–331.
- Hogan, N. (1990), ‘Mechanical impedance of single-and multi-articular systems’, *Multiple muscle systems biomechanics and movement organization* (9), 1–23.
- Howe, R. D., Kao, I. & Cutkosky, M. R. (1988), The sliding of robot fingers under combined torsion and shear loading, pp. 103–105. Proc. IEEE Int. Conf. on Robotics and Automation.
- Hu, X., Murray, W. & Perreault, E. (2011), ‘Muscle short-range stiffness can be used to estimate the endpoint stiffness of the human arm.’, *Journal of Neurophysiology* **105**(4), 1633–1641.

- Huang, S. & Schimmels, J. M. (2000), ‘The bounds and realization of spatial compliances achieved with simple serial elastic mechanisms’, *Robotics and Automation, IEEE Transactions on* **16**(1), 99–103.
- Inouye, J. M., Kutch, J. J. & Valero-Cuevas, F. (2011a), ‘A novel methodology to compare grasp quality: application to two dominant tendon-driven designs’, *Proceedings of the 35nd Annual Meeting of the American Society of Biomechanics, Long Beach, CA, 2011.* .
- Inouye, J. M., Kutch, J. J. & Valero-Cuevas, F. (2011b), ‘Quantitative prediction of grasp impairment following peripheral neuropathies of the hand’, *Proceedings of the 35nd Annual Meeting of the American Society of Biomechanics, Long Beach, CA, 2011.* .
- Inouye, J. M., Kutch, J. J. & Valero-Cuevas, F. J. (2012), ‘A novel synthesis of computational approaches enables optimization of grasp quality of tendon-driven hands’, *Accepted February 2012 to IEEE Transactions on Robotics* .
- Inouye, J. M., Kutch, J. J. & Valero-Cuevas, F. J. (n.d.), ‘Optimization of tendon topology for robotic fingers: Prediction and implementation’, *In review.* .
- Jacobsen, S., Iversen, E., Knutti, D., Johnson, R. & Biggers, K. (1986), Design of the utah/mit dextrous hand, pp. 1520–1532. 1986 IEEE International Conference on Robotics and Automation. Proceedings.
- Jau, B. M. (1995), Dexterous telemanipulation with four fingered hand system, Vol. 1, IEEE, pp. 338–343 vol. 1. Robotics and Automation, 1995. Proceedings., 1995 IEEE International Conference on.
- Kadiallah, A., Liaw, G., Kawato, M., Franklin, D. W. & Burdet, E. (n.d.), ‘Impedance control is selectively tuned to multiple directions of movement’, *Journal of Neurophysiology* .
- Katz, J. N. & Simmons, B. P. (2002), ‘Carpal tunnel syndrome’, *New England Journal of Medicine* **346**(23), 1807.
- Kawasaki, H., Komatsu, T. & Uchiyama, K. (2002), ‘Dexterous anthropomorphic robot hand with distributed tactile sensor: Gifu hand ii’, *Mechatronics, IEEE/ASME Transactions on* **7**(3), 296–303.
- Keenan, K. G., Santos, V. J., Venkadesan, M. & Valero-Cuevas, F. J. (2009), ‘Maximal voluntary fingertip force production is not limited by movement speed in combined motion and force tasks’, *The Journal of Neuroscience* **29**(27), 8784.

- Khan, W. A. & Angeles, J. (2006), ‘The kinetostatic optimization of robotic manipulators: the inverse and the direct problems’, *Journal of mechanical design* **128**, 168.
- Kinoshita, H., Backstrom, L., Flanagan, J. R. & Johansson, R. S. (1997), ‘Tangential torque effects on the control of grip forces when holding objects with a precision grip’, *Journal of Neurophysiology* **78**(3), 1619.
- Kirkpatrick, D., Mishra, B. & Yap, C. K. (1992), ‘Quantitative steinitz’s theorems with applications to multifingered grasping’, *Discrete and Computational Geometry* **7**(1), 295–318.
- Kobayashi, H., Hyodo, K. & Ogane, D. (1998), ‘On tendon-driven robotic mechanisms with redundant tendons’, *The International Journal of Robotics Research* **17**(5), 561.
- Kuo, A. D. & Zajac, F. E. (1993), ‘A biomechanical analysis of muscle strength as a limiting factor in standing posture’, *Journal of Biomechanics* **26**, 137–150.
- Kutch, J. J. & Valero-Cuevas, F. J. (2011), ‘Muscle redundancy does not imply robustness to muscle dysfunction’, *Journal of Biomechanics* **44**(7), 1264–1270.
- Kuxhaus, L., Roach, S. S. & Valero-Cuevas, F. J. (2005), ‘Quantifying deficits in the 3d force capabilities of a digit caused by selective paralysis: application to the thumb with simulated low ulnar nerve palsy’, *Journal of Biomechanics* **38**(4), 725–736.
- Laurin-Kovitz, K. F., Colgate, J. E. & Carnes, S. D. R. (1991), Design of components for programmable passive impedance, IEEE, pp. 1476–1481 vol. 2. Robotics and Automation, 1991. Proceedings., 1991 IEEE International Conference on.
- Lee, J. J. (1991), ‘Tendon-driven manipulators: Analysis, synthesis, and control’.
- Lee, J. J. & Tsai, L. W. (1991), ‘The structural synthesis of tendon-driven manipulators having a pseudotriangular structure matrix’, *The International Journal of Robotics Research* **10**(3), 255.
- Leijnse, J., Quesada, P. M. & Spoor, C. W. (2010), ‘Kinematic evaluation of the finger’s interphalangeal joints coupling mechanism–variability, flexion-extension differences, triggers, locking swan-neck deformities, anthropometric correlations’, *Journal of Biomechanics* **43**(12), 2381–2393.
- Li, Z. & Sastry, S. S. (1988), ‘Task-oriented optimal grasping by multifingered robot hands’, *Robotics and Automation, IEEE Journal of* **4**(1), 32–44.

- Lin, L. R. & Huang, H. P. (1996), Mechanism design of a new multifingered robot hand, Vol. 2, IEEE, pp. 1471–1476 vol. 2. Robotics and Automation, 1996. Proceedings., 1996 IEEE International Conference on.
- Lin, Q., Burdick, J. W. & Rimon, E. (2000), ‘A stiffness-based quality measure for compliant grasps and fixtures’, *Robotics and Automation, IEEE Transactions on* **16**(6), 675–688.
- Lu, Z. & Pong, T. K. (2010), ‘Minimizing condition number via convex programming’.
- Markcnsc scoff, X. & Yapadimitriou, C. H. (1987), ‘Optimum grip of a polygon’.
- Massa, B., Roccella, S., Carrozza, M. C. & Dario, P. (2002), Design and development of an underactuated prosthetic hand, Vol. 4, IEEE, pp. 3374–3379 vol. 4. Robotics and Automation, 2002. Proceedings. ICRA’02. IEEE International Conference on.
- McIntyre, J., Mussa-Ivaldi, F. A. & Bizzi, E. (1989), Modeling of multi-joint motor systems, IEEE, pp. 242–243 vol. 1. Engineering in Medicine and Biology Society, 1989. Images of the Twenty-First Century., Proceedings of the Annual International Conference of the IEEE Engineering in.
- McIntyre, J., Mussa-Ivaldi, F. A. & Bizzi, E. (1996), ‘The control of stable postures in the multijoint arm’, *Experimental brain research* **110**(2), 248–264.
- Miller, A. T. & Allen, P. K. (1999), Examples of 3d grasp quality computations, Vol. 2. 1999 IEEE International Conference on Robotics and Automation, 1999. Proceedings.
- Miller, A. T. & Allen, P. K. (2004), ‘Graspit! a versatile simulator for robotic grasping’, *IEEE Robotics & Automation Magazine* **11**(4), 110–122.
- Milner, T. E. (2002), ‘Contribution of geometry and joint stiffness to mechanical stability of the human arm’, *Experimental brain research* **143**(4), 515–519.
- Mishra, B. (1995), ‘Grasp metrics: Optimality and complexity’.
- Murray, R. M., Li, Z. & Sastry, S. S. (1994), *A mathematical introduction to robotic manipulation*, CRC.
- Mussa-Ivaldi, F. A., Hogan, N. & Bizzi, E. (1985), ‘Neural, mechanical, and geometric factors subserving arm posture in humans’, *The Journal of Neuroscience* **5**(10), 2732–2743.

- Namiki, A., Imai, Y., Ishikawa, M. & Kaneko, M. (2003), Development of a high-speed multifingered hand system and its application to catching, Vol. 3, IEEE, pp. 2666–2671 vol. 3. Intelligent Robots and Systems, 2003.(IROS 2003). Proceedings. 2003 IEEE/RSJ International Conference on.
- Osu, R. & Gomi, H. (1999), ‘Multijoint muscle regulation mechanisms examined by measured human arm stiffness and emg signals’, *Journal of Neurophysiology* **81**(4), 1458.
- Ott, C. (2008), *Cartesian impedance control of redundant and flexible-joint robots*, Vol. 49, Springer Verlag.
- Ou, Y. J. & Tsai, L. W. (1993), ‘Kinematic synthesis of tendon-driven manipulators with isotropic transmission characteristics’, *Journal of mechanical design* **115**, 884.
- Ou, Y. J. & Tsai, L. W. (1996), ‘Isotropic design of tendon-driven manipulators’, *Journal of mechanical design* **118**(3), 360–366.
- Pashkevich, A., Klimchik, A. & Chablat, D. (2011), ‘Enhanced stiffness modeling of manipulators with passive joints’, *Mechanism and machine theory* .
- Paul, C., Valero-Cuevas, F. J. & Lipson, H. (2006), ‘Design and control of tensegrity robots for locomotion’, *Robotics, IEEE Transactions on* **22**(5), 944–957.
- Pearlman, J. L., Roach, S. S. & Valero-Cuevas, F. J. (2004), ‘The fundamental thumb-tip force vectors produced by the muscles of the thumb’, *Journal of Orthopaedic Research* **22**(2), 306–312.
- Perreault, E. J., Kirsch, R. F. & Crago, P. E. (2001), ‘Effects of voluntary force generation on the elastic components of endpoint stiffness’, *Experimental brain research. Experimentelle Hirnforschung. Experimentation cerebrale* **141**(3), 312.
- Perreault, E. J., Kirsch, R. F. & Crago, P. E. (2002), ‘Voluntary control of static endpoint stiffness during force regulation tasks’, *Journal of Neurophysiology* **87**(6), 2808.
- Pollard, N. S. & Gilbert, R. C. (2002), ‘Tendon arrangement and muscle force requirements for humanlike force capabilities in a robotic finger’, *environment* **17**, 14.
- Pons, J. L., Ceres, R. & Pfeiffer, F. (1999), ‘Multifingered dexterous robotics hand design and control: a review’, *Robotica* **17**(6), 674.
- Pratt, G. A. & Williamson, M. M. (1995), Series elastic actuators, Published by the IEEE Computer Society, p. 399. iros.

- Rieffel, J., Valero-Cuevas, F. & Lipson, H. (2009), ‘Automated discovery and optimization of large irregular tensegrity structures’, *Computers & Structures* **87**(5-6), 368–379.
- Riordan, D. C. (1969), ‘Tendon transfers for median, ulnar or radial nerve palsy’, *Hand* **1**(1), 42–46.
- Salisbury, J. K. (1982), ‘Kinematic and force analysis of articulated hands’.
- Salisbury, J. K. & Craig, J. J. (1982), ‘Articulated hands: Force control and kinematic issues’, *The International Journal of Robotics Research* **1**(1), 4.
- Santos, V. J., Bustamante, C. D. & Valero-Cuevas, F. J. (2009), ‘Improving the fitness of high-dimensional biomechanical models via data-driven stochastic exploration’, *Biomedical Engineering, IEEE Transactions on* **56**(3), 552–564.
- Santos, V. J. & Valero-Cuevas, F. J. (2006), ‘Reported anatomical variability naturally leads to multimodal distributions of denavit-hartenberg parameters for the human thumb’, *Biomedical Engineering, IEEE Transactions on* **53**(2), 155–163.
- Shadow Robot Company (n.d.).
URL: <http://www.shadowrobot.com>
- Sheu, J. B., Huang, J. J. & Lee, J. J. (2009), ‘Kinematic synthesis of tendon-driven robotic manipulators using singular value decomposition’, *Robotica* **28**(01), 1–10.
- Shin, D., Kim, J. & Koike, Y. (2009), ‘A myokinetic arm model for estimating joint torque and stiffness from emg signals during maintained posture’, *Journal of Neurophysiology* **101**(1), 387–401.
- Starr, G. P. (1988), Cartesian stiffness control of the jpl/stanford/salisbury hand, IEEE, pp. 636–637 vol. 1. Robotics and Automation, 1988. Proceedings., 1988 IEEE International Conference on.
- Strang, G. (2003), *Introduction to linear algebra*, Wellesley Cambridge Pr.
- Stroeve, S. (1999), ‘Impedance characteristics of a neuromusculoskeletal model of the human arm i. posture control’, *Biological cybernetics* **81**(5), 475–494.
- Sugano, S., Tsuto, S. & Kato, I. (1992), Force control of the robot finger joint equipped with mechanical compliance adjuster, Vol. 3, IEEE, pp. 2005–2013. Intelligent Robots and Systems, 1992., Proceedings of the 1992 IEEE/RSJ International Conference on.
- Surez Feijo, R., Cornell, J. & Roa Garzn, M. (2006), ‘Grasp quality measures’.

- Taguchi, G., Konishi, S. & American Supplier, I. (1987), *Orthogonal arrays and linear graphs: tools for quality engineering*, American Supplier Institute Allen Park, MI.
- Tee, K. P., Franklin, D. W., Kawato, M., Milner, T. E. & Burdet, E. (n.d.), ‘Concurrent adaptation of force and impedance in the redundant muscle system’, *Biological cybernetics* **102**(1), 31–44.
- Tsai, L. W. (1995), ‘Design of tendon-driven manipulators’, *Journal of mechanical design* **117**, 80.
- Tsai, L. W. (1999), *Robot analysis: the mechanics of serial and parallel manipulators*, Wiley-Interscience.
- Tsai, L. W. & Lee, J. J. (1988), ‘Kinematic analysis of tendon-driven robotic mechanisms using graph theory’.
- Valero-Cuevas, F. J. (2005), ‘A mathematical approach to the mechanical capabilities of limbs and fingers’, *Progress in Motor Control* pp. 619–633.
- Valero-Cuevas, F. J., Anand, V. V., Saxena, A. & Lipson, H. (2007), ‘Beyond parameter estimation: Extending biomechanical modeling by the explicit exploration of model topology’, *Biomedical Engineering, IEEE Transactions on* **54**(11), 1951–1964.
- Valero-Cuevas, F. J. & Hentz, V. R. (2002), ‘Releasing the a3 pulley and leaving flexor superficialis intact increases pinch force following the zancolli lasso procedures to prevent claw deformity in the intrinsic palsied finger’, *Journal of Orthopaedic Research* **20**(5), 902–909.
- Valero-Cuevas, F. J., Hoffmann, H., Kurse, M. U., Kutch, J. J. & Theodorou, E. A. (2009), ‘Computational models for neuromuscular function’, *IEEE Reviews in Biomedical Engineering (2) October* p. 110135.
- Valero-Cuevas, F. J., Johanson, M. E. & Towles, J. D. (2003), ‘Towards a realistic biomechanical model of the thumb: the choice of kinematic description may be more critical than the solution method or the variability/uncertainty of musculoskeletal parameters’, *Journal of Biomechanics* **36**(7), 1019–1030.
- Valero-Cuevas, F. J. & Small, C. F. (1997), ‘Load dependence in carpal kinematics during wrist flexion in vivo’, *Clinical Biomechanics* **12**(3), 154–159.
- Valero-Cuevas, F. J., Towles, J. D. & Hentz, V. R. (2000), ‘Quantification of fingertip force reduction in the forefinger following simulated paralysis of extensor and intrinsic muscles’, *Journal of Biomechanics* **33**(12), 1601–1609.

- Valero-Cuevas, F. J., Zajac, F. E. & Burgar, C. G. (1998), ‘Large index-fingertip forces are produced by subject-independent patterns of muscle excitation’, *Journal of Biomechanics* **31**(8), 693–704.
- Wimbock, T., Ott, C., Albu-Schaffer, A., Kugi, A. & Hirzinger, G. (2008), Impedance control for variable stiffness mechanisms with nonlinear joint coupling, IEEE, pp. 3796–3803. Intelligent Robots and Systems, 2008. IROS 2008. IEEE/RSJ International Conference on.
- Wolf, S. & Hirzinger, G. (2008), A new variable stiffness design: Matching requirements of the next robot generation, IEEE, pp. 1741–1746. Robotics and Automation, 2008. ICRA 2008. IEEE International Conference on.
- Yamano, I. & Maeno, T. (2005), Five-fingered robot hand using ultrasonic motors and elastic elements, IEEE, pp. 2673–2678. Robotics and Automation, 2005. ICRA 2005. Proceedings of the 2005 IEEE International Conference on.
- Yoshikawa, T. (1990), *Foundations of robotics: analysis and control*, The MIT Press.
- Yoshikawa, T. (2002), Translational and rotational manipulability of robotic manipulators, IEEE, pp. 1170–1175. Industrial Electronics, Control and Instrumentation, 1991. Proceedings. IECON’91., 1991 International Conference on.
- Zajac, F. E. (1989), ‘Muscle and tendon: properties, models, scaling, and application to biomechanics and motor control’, *Critical reviews in biomedical engineering* **17**(4), 359.
- Zhu, X. & Wang, J. (2003), ‘Synthesis of force-closure grasps on 3-d objects based on the q distance’, *Robotics and Automation, IEEE Transactions on* **19**(4), 669–679.
- Zibil, A., Firmani, F., Nokleby, S. B. & Podhorodeski, R. P. (2007), ‘An explicit method for determining the force-moment capabilities of redundantly actuated planar parallel manipulators’, *Journal of mechanical design* **129**, 1046.